University of Colorado, Boulder
CU Scholar

Aerospace Engineering Sciences Graduate Theses & Dissertations

Aerospace Engineering Sciences

Spring 1-1-2015

An XFEM Approach to Modeling Material Interface Uncertainty

Christapher Lang
University of Colorado Boulder, christapherlang@gmail.com

Follow this and additional works at: https://scholar.colorado.edu/asen_gradetds

Part of the Structures and Materials Commons

An XFEM Approach to Modeling Material Interface Uncertainty

by

Christapher Lang

B.S. Mechanical Engineering, Oklahoma State University, 2000

M.S. Mechanical Engineering, George Washington University, 2002

A thesis submitted to the

Faculty of the Graduate School of the

University of Colorado in partial fulfillment

of the requirements for the degree of

Doctor of Philosophy

Department of Aerospace Engineering

2015

This thesis entitled:
An XFEM Approach to Modeling Material Interface Uncertainty
written by Christapher Lang
has been approved for the Department of Aerospace Engineering

_____

Dr. Kurt Maute

_____

Dr. Alireza Doostan

Date _____

The final copy of this thesis has been examined by the signatories, and we find that both the
content and the form meet acceptable presentation standards of scholarly work in the above
mentioned discipline.

Lang, Christapher (Ph.D. Aerospace Engineering)

An XFEM Approach to Modeling Material Interface Uncertainty

Thesis directed by Prof. Dr. Kurt Maute and Prof. Dr. Alireza Doostan

Abstract

The focus of this research is uncertainty modeling for problems with random geometry. This dissertation develops a computational framework, based on the eXtended Finite Element Method (XFEM) and a Polynomial Chaos Expansion (PCE), for modeling heterogeneous materials with uncertain material interfaces. The uncertain geometry is characterized based on a finite set of random parameters, which requires a collection of measurement data or images. The XFEM is particularly useful for problems with changing interface geometries, as remeshing is avoided since a conforming mesh is not required. The XFEM is extended to the probability domain by a PCE based on the random parameters defining the uncertain geometry, and a random level set function implicitly defines the uncertain geometry. An intrusive PCE is implemented, which integrates the expansion within the deterministic model. Problems with continuous and discontinuous solutions at the material interface are solved, which utilize different enrichment functions. An accurate integration approach is introduced for the stochastic domain for both types of solutions. For problems with continuous solutions at the interface, a strategy for choosing a proper C^0-continuous enrichment function is presented. A PCE is best suited to approximating a smooth behavior of the degrees of freedom, and this research shows that a proper C^0-continuous enrichment function leads to a smooth behavior of the degrees of freedom when the spatial mesh is converged. To address solving problems with discontinuous solutions at the interface, an implementation of the Heaviside enriched XFEM is presented which provides a robust approach for handling complex interface configurations. A preconditioning scheme was developed to avoid ill-conditioning due to small intersected element volumes. The Heaviside enriched XFEM extended to the probability domain leads to a smooth behavior of the degrees of freedom regardless of the spatial mesh size.

The C^0-continuous enrichment requires simultaneous spatial and stochastic refinement to reduce the approximation error, while the Heaviside enrichment function leads to a solution that converges at low stochastic approximation orders for each spatial mesh size. Numerical examples include heat diffusion and linear elasticity for problems containing a single inclusion with random geometry.

Acknowledgements

Contents

Chapter

Appendix

Chapter 1

Introduction

It is critical to account for input uncertainty when modeling systems for engineering design, as realistic conditions are not known precisely. All input data contain some amount of uncertainty, which can be classified as epistemic and aleatory. Epistemic uncertainty is the variability due to limited data and knowledge, and it is considered reducible by obtaining additional data. Aleatory uncertainty is the natural randomness which cannot be reduced. There are two key challenges in uncertainty analysis to account for the input variability. First, the input data must be characterized to represent the uncertainty, which may include collecting sample data and engineering judgment. The second challenge is the propagation of the uncertain inputs to outputs through the governing stochastic partial differential equations (PDEs) of the system. The governing PDEs are stochastic due to a random operator or right-hand side for uncertain loads, material properties, and boundary conditions, which have been extensively studied [14, 2, 22, 9]. However, geometric uncertainty presents additional challenges due to the uncertain domain definition, which is the focus of this research.

The Finite element (FE) method is a widespread numerical approach for solving PDEs. For systems governed by stochastic PDEs, the FE method may be coupled with a sampling approach such as Monte Carlo (MC) simulation or stochastic collocation [1, 21, 34]. These sampling approaches require solutions for multiple sample points generated from the uncertain input data. A more efficient approach is the spectral stochastic FE method (SSFEM) [4, 12, 14, 35]. In SSFEM, a polynomial chaos expansion (PCE) [35, 5, 6, 13, 32, 7] approximates the degrees of freedom, and

a Galerkin projection is used to solve for the coefficients of the expansion. The SSFEM is best suited for problems in which the degrees of freedom vary smoothly with respect to the random parameters. For uncertainty in geometry, a sampling approach requires the generation of a new mesh which conforms to the geometry for each sample. The eXtended Finite Element Method (XFEM) [23, 11, 15] offers the advantage of not requiring a conforming mesh for problems with uncertain geometry. However, the degrees of freedom may not depend smoothly on the random parameters. This research addresses the smooth dependency and develops a computational framework, based on the XFEM and a PCE, for modeling heterogeneous materials with uncertain inclusion geometry.

The work here is focused on predicting the behavior of composite materials with uncertain inclusion geometry. The heat diffusion and elasticity response is studied for materials in which the inclusion geometry is uncertain, which may be due to processing techniques, manufacturing tolerances, and measurement errors. Understanding the behavior of these types of material systems is critical, since the effective properties depend on the shape and size of the inclusions. The uncertain inclusion geometry is characterized by a set of random parameters, and the statistics of the response, such as the mean, variance, and probability distribution, are determined.

The first challenge of characterizing the uncertain geometry is accomplished by collecting experimental data. For geometric uncertainty, measurement data or a set of images is collected for numerous outcomes of the interface geometry. Various approaches exist for representing the uncertain geometry, such as selecting specific geometric features as functions of random inputs. For this work, the level set method [28] is used to represent the inclusion geometry. The level set method is typically combined with the XFEM [11, 30, 31, 33] to implicitly define the inclusion geometry according to a level set function. For uncertain geometry, a random level set function is constructed based on a set of finite random variables using the collected experimental data. For example, an approach for creating a random level set function using shape recovery and a collection of images such as micrographs is proposed in [29]. The characterization of the random geometry mathematically describes the uncertain input for solving the governing partial differential equation of the system.

The second challenge of propagating the uncertain inputs is the primary focus of this research, and a characterization of the random inclusion geometry is assumed. For dealing with geometric uncertainty, the XFEM is a natural choice for utilization in the computational approach. The XFEM is a deterministic approach for modeling problems with non-smooth solutions, which arise from geometric features such as holes, cracks, and inclusions. The XFEM combined with the level set method [3, 10, 16, 30, 8] is particularly well-suited for modeling problems with changing material interfaces, which arises for transient, optimization, and uncertainty analyses. A mesh which conforms to the geometric feature is not required, therefore remeshing is avoided and a fixed spatial mesh is utilized. However, a drawback of the XFEM is that an ill-conditioned system of equations occurs when the ratio of volumes on either side of the interface in an element is small [11, 27]. The ill-conditioning is an issue which must be addressed for a robust approach to solving problems with moving or changing interface geometry. A technique is desired which avoids ill-conditioning for any small element intersection without loss of solution accuracy.

A Monte Carlo (MC) simulation using the XFEM is a straightforward approach for solving problems with uncertain geometry. A robust implementation of the XFEM is necessary such that numerous interface configurations can be accurately modeled by the same spatial mesh without loss of accuracy due to complex geometry or ill-conditioning. A robust XFEM implementation is presented for modeling inclusion problems, and a preconditioning scheme is developed to avoid any ill-conditioning. The XFEM is used to solve multiple interface configurations to study the system dependency on the random parameters and compare with the PCE approximation. While a MC simulation can be used to solve simple problems, it is infeasible for complex problems as it requires numerous deterministic solutions.

The eXtended Stochastic Finite Element Method (X-SFEM) is a recently proposed approach for modeling geometric uncertainty [26]. The spatial domain is augmented by a probability domain by combining the XFEM with a PCE to approximate the solution as a function of the spatial coordinates and random parameters. The PCE approximates the variation of the degrees of freedom in the probability domain, and the choice of enrichment function affects the smoothness of the

degrees of freedom over part or the entire domain. The X-SFEM has been studied for problems with random domains [25] as well as problems with random inclusion geometry with C^0-continuous solutions at the material interface [24]. The application of PCE may lead to exponential convergent rates if the degrees of freedom vary smoothly with respect to the random parameters. However, the PCE may converge slowly or fail to converge if the behavior of the degrees of freedom is non-smooth in the stochastic domain. For the case of random material inclusions, an enrichment function tailored to the X-SFEM for problems with C^0-continuous solutions was presented in [24] which results in a smooth behavior of the degrees of freedom in the stochastic domain.

This research follows the work on X-SFEM for solving problems with random material inclusions. The combination of the XFEM and PCE provides the basis of the computational framework for solving problems with uncertain geometry. The computational expense required to solve stochastic partial differential equations utilizing PCE methods greatly increases with respect to the number of random parameters. In this research, an intrusive PCE approach is used as opposed to a non-intrusive sampling approach, which provides computational efficiency by manipulating the elemental matrices to incorporate the stochastic approximation. Various enrichment functions for problems with continuous and discontinuous solutions at the material interface are explored in this work. Utilizing a C^0-continuous and Heaviside enrichment function require different approaches for solving problems with uncertain inclusion geometry.

The novel contributions of this research are summarized. The challenges associated with the X-SFEM using a C^0-continuous enrichment was studied, which is specific to solving problems with C^0-continuous solutions at the material interface. An implementation of the XFEM with a Heaviside enrichment was developed and extended to the X-SFEM, which is applicable to solving problems with discontinuous and C^0-continuous solutions at the interface. A constraint is enforced to maintain continuity of the solution at the interface for the latter. The contributions are classified into three groups: X-SFEM with C^0-continuous enrichment, XFEM with Heaviside enrichment, and X-SFEM with Heaviside enrichment.

1. **X-SFEM with a C^0-continuous enrichment function**

1.1. Successful enrichment function

The XFEM is extended to the stochastic domain using a PCE for modeling problems with a random inclusion using a C^0-continuous enrichment [24]. A spectral PCE approximates the variation of the degrees of freedom in the probability domain. A spectral PCE is best suited for approximating a smooth variation over the entire domain, and the choice of the enrichment function determines the behavior of the degrees of freedom. Therefore careful consideration is needed for the choice of enrichment function in order to maintain accuracy and efficiency. The basic elements of a successful enrichment function are identified [17], which lead to a smooth variation over the entire domain. Note that the smooth variation for a C^0-continuous enrichment depends on a converged spatial mesh.

1.2. Partitioning of the probability domain

As in the XFEM, where a partition of the spatial domain is required for integration of an intersected element, a partition of the probability domain is required for accurate integration in the X-SFEM for the C^0-continuous approach [17]. The element integration over the stochastic domain is piecewise smooth depending on whether the element is intersected, and the intersection of the element is determined by the nodal level set function. A partition of the probability domain is constructed which aligns with the zero level set function for the nodes of the element. The zero level set at the nodes of the element correspond to where the element becomes intersected according to the random parameters. The piecewise smooth behavior of the element quantities align with the zero nodel level set values in the stochastic domain.

1.3. Efficiency and accuracy

The implementation of various C^0-continuous enrichment functions in the X-SFEM are studied [17], and the effectiveness of using a spectral PCE is presented. Two stochastic approximation approaches, a spectral PCE and a linear FE, are compared for efficiency and accuracy. A linear FE approximation is better suited to approximate a non-smooth or piecewise smooth variation,

however a higher number of unknowns are needed as compared to a spectral PCE. A spectral PCE with a proper C^0-continuous enrichment function is more efficient and as accurate as a linear FE approximation.

2. Heaviside enriched XFEM

2.1. Generalized Heaviside enriched XFEM

When solving problems with moving or changing inclusion geometry, the implementation of the XFEM needs to be robust and accurate for any potential interface configuration. In order to improve accuracy for complex interface configurations, the Heaviside enriched XFEM implementation [15] is extended to multiple enrichment levels in order to accurately model neighboring intersected elements and element intersected more than once. The method is applied to problems with varying inclusion geometry [18]. A robust XFEM implementation is required when solving problems with changing interface geometries. The numerical method needs to be accurate for any interface configuration, and the generalized Heaviside enrichment strategy enables more complex interface geometries to be accurately modeled.

2.2. Preconditioning scheme

In addition to requiring accurate solutions for any potential interface configuration, a robust implementation of the XFEM is needed. One drawback to the XFEM is that an ill-conditioned system of equations may result when an intersected element has a small ratio of volumes on either side of the interface. The ill-conditioning can introduce solution error, particularly for iterative linear solvers and nonlinear problems. In order to eliminate any ill-conditioning, a preconditioning scheme is introduced for the Heaviside enriched XFEM. The preconditioning scheme, which consists of a geometric preconditioner and constraining degrees of freedom to zero for small intersections, maintains a well-conditioned system with a low condition number without loss of solution accuracy [18]. The preconditioning scheme adds to the robustness of the XFEM implementation by accurately solving the problem regardless of the intersection

configuration.

3. Heaviside enriched X-SFEM

3.1. Extension of the Heaviside enriched XFEM to the stochastic domain

The generalized Heaviside enriched XFEM is extended to the stochastic domain in order to model problems with uncertain inclusion geometry [19]. The Heaviside enrichment is implemented to solve problems with discontinuous solutions at the material interface. In contrast to using a C^0-continuous enrichment function, the Heaviside enrichment function leads to a smooth variation of the degrees of freedom regardless of the spatial mesh size. However, the degrees of freedom are nonzero (active) on a subdomain of the probability domain. Therefore instead of a spectral PCE, the support of the polynomial basis functions is adjusted according to the active subdomain while maintaining orthogonality. The examples show convergence at low orders of the PCE. Additionally, the Heaviside enriched approach is applied to problems with C^0-continuous solutions by enforcing continuity at the interface using the stabilized Lagrange and Nitsche methods. A higher convergence rate is achieved compared to using proper C^0-continuous enrichment.

3.2. Partitioning of the probability domain

As in the X-SFEM with a C^0-continuous enrichment function, a partition of the probability domain is necessary for accurate integration for the Heaviside enriched X-SFEM. The partition is needed to align with the piecewise smoothness behavior of the element quantities with respect to the random parameters. Due to the proposed support adjustment of the polynomial basis, a partition is constructed which aligns with the support of the polynomial basis in addition to the zero nodal level set functions.

Chapter 2

Summary of Publications

A brief overview of each of the journal papers resulting from this dissertation are presented. Publication 1 and Publication 2 have been peer reviewed and published by the journal. Publication 3 has been submitted for publication in Computational Mechanics. The journal papers are included in the Appendix.

2.1 Publication 1: Extended stochastic FEM for diffusion problems with uncertain material interfaces

The eXtended Stochastic Finite Element Method (X-SFEM) proposed by Nouy et. el. was studied for diffusion problems with a single material inclusion. The uncertain geometry of the inclusion was modeled by 1 and 2 random parameters. Two important challenges in the X-SFEM are addressed in this paper. First, choosing an enrichment function is critical for accurately capturing the C^0-continuous solution in the spatial and probability domains. Various enrichment functions are compared, and the basic elements of a successful enrichment are identified. For a successful C^0-continuous enrichment in the X-SFEM, the support of the enrichment function should include all possibly intersected elements as well as the neighboring elements of the intersected elements (blending elements). Also, the spatial support of the enrichment function should be global instead of a local variation for a given realization. The second challenge addressed was accurate integration over the stochastic domain, which is achieved by correctly partitioning the domain. An accurate partitioning method for the stochastic domain is presented which aligns with where the interface

intersects a node. In addition to addressing these important challenges, the efficiency and accuracy of a spectral PCE and a linear FE are studied and compared. The spectral PCE showed the best performance in terms of accuracy and convergence properties for a properly chosen enrichment function.

2.2 Publication 2: A simple and efficient preconditioning scheme for Heaviside enriched XFEM

A robust formulation of the eXtended Finite Element Method (XFEM) is necessary when solving problems with moving or changing interface geometries on fixed spatial meshes. An accurate formulation is needed regardless of the specific interface geometry in relation to the spatial mesh. Using the generalized formulation of the Heaviside enriched XFEM [20], neighboring intersected elements and multiply intersected elements can be accurately modeled, and there are no issues with blending elements. This paper presents a preconditioning scheme for the Heaviside enriched XFEM which avoids the ill-conditioning which results when the ratio of volumes on either side of the interface in an element is small. The geometric preconditioner is computed from the nodal basis functions and the interface configuration. Therefore it is well suited to nonlinear problems with fixed and moving interfaces since it is constructed prior to building the system of equations. The geometric preconditioner combined with constraining degrees of freedom to zero for extremely small intersections leads to an almost constant condition number regardless of the interface configuration without loss of solution accuracy. Numerical examples are presented for discontinuous and C^0-continuous problems which compare the condition number and solution accuracy with and without the proposed preconditioning scheme.

2.3 Publication 3: Heaviside enriched extended stochastic FEM for problems with uncertain material interfaces

The Heaviside enriched XFEM is extended to the stochastic domain following the approach of the X-SFEM to model problems with a discontinuous solution at the interface of an uncertain

material inclusion. The Heaviside enrichment leads to a discontinuous solution in the spatial and stochastic domains. In particular, the degrees of freedom are non-zero (active) for only a part of the stochastic domain. In order to apply a PCE for approximation of the degrees of freedom in the stochastic domain, the proposed approach adjusts the support of the stochastic approximation according to the subdomain over which the degree of freedom is active. This support adjustment increases accuracy and leads to a well-conditioned system of equations. Numerical examples are presented for problems with discontinuous and C^0-continuous solutions to examine accuracy and the convergence rate. The C^0-continuous problems, which require enforcement of an interface constraint, are included in order to compare with the approach in Publication 1. The degrees of freedom are smooth when using a Heaviside enrichment regardless of the mesh size, and a higher convergence rate is achieved with the Heaviside enrichment approach for the C^0-continuous problems when compared to the C^0-continuous enrichment.

Chapter 3

Conclusions

3.1   Concluding Remarks

This dissertation focused on the development of a computational framework to solve problems with geometric uncertainty. The specific problems studied in this work were heat diffusion and linear elasticity of heterogeneous materials with uncertain inclusion geometry. The method was developed for problems in 2D space with consideration given to the extension to 3D. The XFEM was utilized to avoid remeshing due to the variation in geometry. Methods for solving the deterministic problem with the XFEM using continuous and discontinuous solutions at the material interface were both developed using different enrichment functions. The degrees of freedom were studied as a function of the random parameters in order to understand the behavior and influence of the choice of enrichment function, as well as the solution accuracy. A properly chosen C^0-continuous enrichment requires a converged spatial mesh for a smooth dependency of the degrees of freedom on the random inputs. A robust implementation of the XFEM is needed for solving problems with varying inclusion geometry, in which solution accuracy and efficiency is maintained regardless of the interface configuration. The issues which affect accuracy include small element intersections, neighboring intersected elements, and elements intersected more than once, which may not be avoided with a fixed spatial mesh. The generalized Heaviside enrichment with the preconditioning scheme, which can be applied to problems with continuous and discontinuous solutions at the material interface, addresses each of these issues for a deterministic analysis.

The computational method developed for this dissertation combines the XFEM and a poly-

nomial chaos expansion in order to solve the governing partial differential equation defined on a random domain. The uncertain geometry is characterized based on a finite set of random parameters. The discretization of the problem augments the spatial domain with a probability domain to solve for the degrees of freedom as functions of the random parameters. Various enrichment functions were explored for problems with continuous and discontinuous solutions at the material interface. While the specific application was heat diffusion and linear elasticity problems with a single random inclusion, the method developed is applicable to a wide range of problems and for multiple inclusions.

3.2   Future Work

Based on the continuation of this research and additional work performed during this research, some potential directions for future work include:

- *Extension to problems in 3D space* The work in this research focused on solving problems in 2 spatial dimensions, and the extension to 3D would be a step forward for solving problems with uncertain geometry. The element intersection configurations become more complex in 3 spatial dimensions, which must be understood for partitioning the domain for accurate integration as well as developing a robust implementation to handle the changing geometry of the interface.

- *Strategy for extension to higher stochastic dimensions* The theory for the extension of this research to more than two random parameters has been discussed. The opportunity exists to implement the proposed framework in higher probability dimensions to understand limitations and apply perhaps more efficient numerical techniques. The partitioning of the stochastic domain needs to be addressed for greater than 2 random parameters. The current research uses a constrained Delaunay triangulation to partition the 2D stochastic domain for numerical integration, which allows an aligned partition. However, constrained Delaunay triangulation does not exist in higher dimensions. Therefore a partitioning tech-

nique for integration in the stochastic domain is needed. Additionally, the computational cost exponentially increases as the number of random parameters is increased. Therefore efficient techniques for higher dimensions would greatly improve the current approach.

- *Preconditioning scheme for Heaviside enriched X-SFEM* The preconditioning scheme developed for the XFEM was not used in the Heaviside enriched X-SFEM. However, ill-conditioning also results due to small volumes in the stochastic domain with 2 random parameters. In this research, it was necessary to constrain to zero the coefficients for the degrees of freedom with very small stochastic supports. We studied various preconditioning approaches to address the ill-conditioning, which included a global preconditioner for the X-SFEM system of equations as well as an XFEM preconditioner applied to each realization at a stochastic integration point. However, a robust implementation which avoids any ill-conditioning was not completed. A preconditioning approach may help avoid ill-conditioned systems in the X-SFEM and reduce the error associated with the current approach of constraining coefficients.

- *Intrusive versus non-intrusive methods* The computational method developed in this work focused on an intrusive PCE, which requires access to the source code when working with existing deterministic models. A non-intrusive PCE or stochastic collocation method could utilize existing deterministic codes to solve the stochastic problem. Also, a comparison of the efficiency and accuracy between an intrusive and non-intrusive approach for geometric uncertainty would benefit the research community.

- *Application to transient analysis* The extension of the proposed framework to the class of problems with a dynamically evolving interface warrants investigation. The uncertainty may be due to the initial inclusion geometry as well as how the geometry evolves. An example of this problem type is a melting or solidification analysis. As part of this research for considering this class of problems, a transient XFEM analysis was applied for solving a melting bar and inclusion problem. The diffusion, Hamilton-Jacobi, and Helmholtz

equations were solved simultaneously to capture the evolving interface and temperature distribution. The diffusion equation determines the temperature field, the Stefan condition determines the interface velocity, the Helmholtz equation determines the velocity field, and the Hamilton-Jacobi equation determines the evolved level-set field. The application of the X-SFEM to solve transient problems with geometric uncertainty is another step forward for this research.

Bibliography

[1] I. Babuška, F. Nobile, and R. Tempone. A stochastic collocation method for elliptic partial differential equations with random input data. SIAM J. Numer. Anal., 43:1005–1034, 2007.

[2] I. Babuška, R. Tempone, and G. Zouraris. Solving elliptic boundary value problems with uncertain coefficients by the finite element method: the stochastic formulation. Comput. Methods Appl. Mech. Eng., 194:1251–1294, 2005.

[3] T. Belytschko, N. Moës, S. Usui, and C. Parimi. Arbitrary discontinuities in finite elements. Int. J. Numer. Meth. Engng., 50:993–1013, 2001.

[4] M. Deb, I. Babuška, and T. Oden. Solution of stochastic partial differential equations using galerkin finite element techniques. Comput. Methods Appl. Mech. Engrg., 190:6359–6372, 2001.

[5] B. Debusschere, H. Najm, P. Pébay, O. Knio, R. Ghanem, and O. Le Maître. A simple and efficient preconditioning scheme for heaviside enriched XFEM. Comput. Mech., 54:1357–1374, 2014.

[6] C. Desceliers, R. Ghanem, and C. Soize. Maximum likelihood estimation of stochastic chaos representations from experimental data. Int. J. Numer. Meth. Engng., 66:978–1001, 2006.

[7] M. Eldred, C. Webster, and P. Constantine. Evaluation of non-intrusive approaches for wiener-askey generalized polynomial chaos. AIAA, 2008-1892.

[8] M. Farsad, F. Vernerey, and H. Park. An extended finite element/level set method to study surface effects on the mechanical behavior and properties of nanomaterials. Int. J. Numer. Meth. Engng., 84:1466–1489, 2010.

[9] P. Frauenfelder, C. Schwab, and R. Todor. Finite elements for elliptic problems with stochastic coefficients. Comput. Methods Appl. Mech. Eng., 194:205–228, 2005.

[10] T. P. Fries. A corrected X-FEM approximation without problems in blending elements. Int. J. Numer. Methods Eng., 75:503–532, 2008.

[11] T. P. Fries and T. Belytschko. The extended/generalized finite element method: an overview of the method and its applications. Int. J. Numer. Methods Eng, 84:253–304, 2010.

[12] R. Ghanem. Ingredients for a general purpose stochastic finite elements implementation. Comput. Methods Appl. Mech. Engrg., 168:19–34, 1999.

[13] R. Ghanem and A. Doostan. On the construction and analysis of stochastic models: Characterization and propagation of the errors associated with limited data. J. Comput. Phys., 217:63–81, 2006.

[14] R. Ghanem and P. Spanos. Stochastic Finite Elements: A Spectral Approach. Springer, 1991.

[15] A. Hansbo and P. Hansbo. A finite element method for the simulation of strong and weak discontinuities in solid mechanics. Comput. Methods Appl. Mech. Eng., 193:3523–3540, 2004.

[16] H. Ji, D. Chopp, and J. Dolbow. A hybrid extended finite/level set method for modeling phase transformations. Int. J. Numer. Meth. Engng., 54:1209–1233, 2002.

[17] C. Lang, A. Doostan, and K. Maute. Extended stochastic FEM for diffusion problems with uncertain material interfaces. Comput. Mech., 51:1031–1049, 2013.

[18] C. Lang, D. Makhija, A. Doostan, and K. Maute. A simple and efficient preconditioning scheme for heaviside enriched XFEM. Comput. Mech., 54:1357–1374, 2014.

[19] C. Lang, A. Sharma, A. Doostan, and K. Maute. Heaviside enriched extended stochastic FEM for problems with uncertain material interfaces. Comput. Mech., 2015. to appear.

[20] D. Makhija and K. Maute. Numerical instabilities in level set topology optimization with the extended finite element method. Struct. Multidiscip. Optim., 49:185–197, 2014.

[21] L. Mathelin and M. Hussaini. A stochastic collocation algorithm for uncertainty analysis. Technical Report CR-2003-212153, NASA, 2003.

[22] H. Matthies and A. Keese. Galerkin methods for linear and nonlinear elliptic stochastic partial differential equations. Comput. Methods Appl. Mech. Engrg., 194:1295–1331, 2005.

[23] N. Moës, J. Dolbow, and T. Belytschko. A finite element method for crack growth without remeshing. Int. J. Numer. Methods Eng., 46:131–150, 1999.

[24] A. Nouy and A. Clément. Extended stochastic finite element method for the numerical simulation of heterogeneous materials with random material interfaces. Int. J. Numer. Meth. Engng., 83:1312–1344, 2010.

[25] A. Nouy, A. Clément, F. Schoefs, and N. Moës. An extended stochastic finite element method for solving stochastic partial differential equations on random domains. Comput. Methods Appl. Mech. Engrg., 197:4663–4682, 2008.

[26] A. Nouy, F. Schoefs, and N. Moës. X-sfem, a computational technique based on x-fem to deal with random shapes. Eur. J. Comput. Mech., 16:277–293, 2007.

[27] A. Reusken. Analysis of an extended pressure finite element space for two-phase incompressible flows. Comput. Vis. Sci., 11:293–305, 2008.

[28] J. Sethian. Level Set Methods and Fast Marching Methods: Evolving Interfaces in Computational Geometry, Fluid Mechanics, Computer Vision, and Materials Science. Cambridge University Press, 1999.

[29] G. Stefanou, A. Nouy, and A. Clément. Identification of random shapes from images through polynomial chaos expansion of random level set functions. Int. J. Numer. Meth. Engng., 79:127–155, 2009.

[30] N. Sukumar, D. Chopp, N. Moës, and T. Belytschko. Modeling holes and inclusions by level sets in the extended finite element method. Comput. Methods Appl. Mech. Eng., 190:6183–6200, 2001.

[31] L. Tan and N. Zabaras. A level set simulation of dendritic solidification with combined features of front-tracking and fixed-domain methods. J. Comput. Phys., 211:36–63, 2006.

[32] X. Wan and G. Karniadakis. An adaptive multi-element generalized polynomial chaos method for stochastic differential equations. J. Comput. Phys., 209:617–642, 2005.

[33] M. Wang, X. Wang, and D. Guo. A level set method for structural topology optimization. Comput. Methods Appl. Mech. Engrg., 192:227–246, 2003.

[34] D. Xiu and J. Hesthaven. High-order collocation methods for differential equations with random inputs. SIAM J. Sci. Comput., 27:1118–1139, 2005.

[35] D. Xiu and G. Karniadakis. The wiener-askey polynomial chaos for stochastic differential equations. SIAM J. Sci. Comput., 24:619–644, 2002.

Appendix A

Publication 1: Extended stochastic FEM for diffusion problems with uncertain material interfaces

ORIGINAL PAPER

Extended stochastic FEM for diffusion problems with uncertain material interfaces

Christapher Lang · Alireza Doostan · Kurt Maute

Abstract This paper is concerned with the prediction of heat transfer in composite materials with uncertain inclusion geometry. To numerically solve the governing equation, which is defined on a random domain, an approach based on the combination of the Extended finite element method (X-FEM) and the spectral stochastic finite element method is studied. Two challenges of the extended stochastic finite element method (X-SFEM) are choosing an enrichment function and numerical integration over the probability domain. An enrichment function, which is based on knowledge of the interface location, captures the C^0-continuous solution in the spatial and probability domains without a conforming mesh. Standard enrichment functions and enrichment functions tailored to X-SFEM are analyzed and compared, and the basic elements of a successful enrichment function are identified. We introduce a partition approach for accurate integration over the probability domain. The X-FEM solution is studied as a function of the parameters describing the inclusion geometry and the different enrichment functions. The efficiency and accuracy of a spectral polynomial chaos expansion and a finite element approximation in the probability domain are compared. Numerical examples of a two-dimensional heat conduction problem with a random inclusion show the spectral PC approximation with a suitable choice of enrichment function is as accurate and more efficient than the finite element approach. Though focused on heat transfer in composite materials, the techniques and

observations in this paper are also applicable to other types of problems with uncertain geometry.

1 Introduction

Uncertainty in geometry is important when performing numerical simulations to predict the behavior of a broad class of engineering systems. The sources of geometric uncertainty may include processing techniques, manufacturing tolerances, and measurement errors. One important example is predicting the effective properties of heterogeneous composite materials. The effective properties directly depend on the size, shape, and distribution of the inclusions within the host matrix. Even with precise processing techniques, these geometric parameters will vary throughout the material. Extensive testing may be required to characterize the resulting variability in material properties and performance. A computational approach which accounts for geometric uncertainty is essential for realistic predictions, can reduce costly and time consuming experimental characterization, and enables the study of manufacturing precision requirements.

For predicting the properties of composite materials, the effective macroscopic properties depend on the details of the microstructure. A homogenization technique which takes into account the stochastic distribution of the microstructure, such as one based on the self-consistent method [12], periodic media [27], or the Mori–Tanaka method [21], can be used to determine the macroscopic properties. The uncertainty analysis is performed on a representative microstructure, and the homogenization technique is used to determine

C. Lang
Structural Mechanics and Concepts Branch,
NASA Langley Research Center, Hampton, VA, USA

A. Doostan (✉) · K. Maute
Aerospace Engineering Sciences, University of Colorado, Boulder, CO, USA
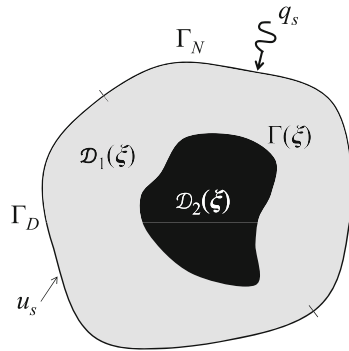e-mail: alireza.doostan@colorado.edu

Springer

Fig. 1 Schematic of the model problem with random inclusion geometry

effective macroscopic predictions. Another approach to include the details of the random microstructure in the macroscopic predictions is a multiscale stochastic analysis, such as in [1,13], which incorporates material features at different spatial scales. For both of these approaches, a microstructural analysis that includes geometric uncertainty must be performed.

The Extended Stochastic Finite Element Method (X-SFEM) is a recently proposed method for solving partial differential equations defined on random domains [22,24]. In this work, we study the X-SFEM in detail for solving a stationary diffusion equation with random geometry. Specifically, we are interested in solving the steady-state heat conduction in a material with a single inclusion which has uncertain geometry, as depicted in Fig. 1. This simple model problem allows the features of the numerical approach to be closely examined and describes the class of problems for which this work applies. The spatial domain is denoted by $\mathcal{D} \subset \mathbb{R}^n$, and $(\Omega, \mathcal{B}, P)$ is the probability space on which the geometric uncertainty is defined. Here Ω is the set of elementary events, $\mathcal{B}$ the σ-algebra of events, and P the probability measure. The random variables $\boldsymbol{\xi} : \Omega \to \mathbb{R}^d$, for some finite dimension $d \in \mathbb{N}$, characterize the geometric uncertainty. The domain $\mathcal{D}$ is comprised of two non-overlapping random subdomains, $\mathcal{D} = \mathcal{D}_1(\boldsymbol{\xi}) \cup \mathcal{D}_2(\boldsymbol{\xi})$, and the closure of $\mathcal{D}$ is denoted by $\bar{\mathcal{D}}$. The random interface which separates the two subdomains is defined by $\Gamma(\boldsymbol{\xi}) = \partial\mathcal{D}_1(\boldsymbol{\xi}) \cap \partial\mathcal{D}_2(\boldsymbol{\xi})$. The model problem consists of finding the random solution field $u(\boldsymbol{x}, \boldsymbol{\xi}) : \bar{\mathcal{D}} \times \Omega \to \mathbb{R}$, such that the following holds almost surely in Ω,

$$
\begin{aligned}
-\nabla^T (k\nabla u_i) &= f && \text{in } \mathcal{D}_i(\boldsymbol{\xi}) \\
(k\nabla u_i)^T \boldsymbol{n}_i &= q_s && \text{on } \partial\mathcal{D}_i \cap \Gamma_N \\
u_i &= u_s && \text{on } \partial\mathcal{D}_i \cap \Gamma_D \\
u_1 - u_2 &= 0 && \text{on } \Gamma(\boldsymbol{\xi}) \\
(k_1\nabla u_1)^T \boldsymbol{n}_1 + (k_2\nabla u_2)^T \boldsymbol{n}_2 &= 0 && \text{on } \Gamma(\boldsymbol{\xi}) ,
\end{aligned} \tag{1}
$$

for $i = 1, 2$, where k is the thermal conductivity, and u_i denotes the restriction of u to $\mathcal{D}_i(\boldsymbol{\xi})$. A heat flux q_s is specified on a Neumann boundary, denoted by Γ_N, with an outward unit normal to $\mathcal{D}_i$ denoted by $\boldsymbol{n}_i$. A temperature u_s is specified on a Dirichlet boundary, denoted by Γ_D. Volumetric heat source terms, f, are specified in $\mathcal{D}$. Isotropy is assumed for the material subdomains, and the conductivity is defined as

$$
k(\boldsymbol{x}, \boldsymbol{\xi}) = \begin{cases} 0 < k_{min} < k_1 < k_{max} < \infty & \text{if } \boldsymbol{x} \in \mathcal{D}_1(\boldsymbol{\xi}) \\ 0 < k_{min} < k_2 < k_{max} < \infty & \text{if } \boldsymbol{x} \in \mathcal{D}_2(\boldsymbol{\xi}) \end{cases} \tag{2}
$$

with constants k_1 and k_2. Without loss of generality, we only consider uncertainty in the interface geometry. Therefore we assume that the conductivities in both material phases, source terms, and boundary conditions are deterministic. For well-posedness, k_1 and k_2 are bounded by a minimum and maximum value. We note that the model problem is deterministic for a realization of the inclusion geometry (one possible outcome of $\boldsymbol{\xi}$). The solution for a fixed inclusion geometry, $u(\boldsymbol{x})$, and the solution for a fixed spatial location, $u(\boldsymbol{\xi})$, are both C^0-continuous across the material interface. The numerical method must capture the non-smooth (only C^0-continuous) solution in the spatial and probability domains.

The stochastic nature of the inclusion geometry must be described in order to solve the model problem. In general, numerous sample measurements of the geometry are required to construct an accurate characterization. Some techniques for identifying a random field to describe the random inclusion geometry are discussed in [7,10]. The approach proposed in [29] converts a set of material images, such as micrographs, into a probabilistic implicit description of the geometry based on a finite set of random variables. Using sample images is particularly practical for characterizing random inclusion geometry for composite materials.

A straightforward approach to solve the model problem in (1) defined on a random domain, is to use a Monte Carlo (MC) simulation (or other stochastic sampling techniques such as stochastic collocation [2,18,37]) coupled with a deterministic finite element solver. The solution of numerous deterministic problems are needed, each requiring a conforming mesh for the inclusion geometry. The computational costs can quickly become expensive and possibly prohibitive for problems involving complex geometries or large deterministic models. Other approaches for solving the model problem include transforming the governing equation so that it is defined on a deterministic domain by using a stochastic mapping [39] or the fictitious domain method [5]. These approaches are; however, limited in the level of complexity of the geometry that can be handled.

In the deterministic framework, the Extended Finite Element Method (X-FEM) is an approach for modeling problems with non-smooth solutions without requiring a mesh

that conforms to material interfaces [19]. In X-FEM, an enrichment function is used to capture the solution discontinuity that occurs when the material interface intersects an element. X-FEM is typically combined with the level set approach [25,28] to describe interface geometries and to define the enrichment function based on *a priori* knowledge of the interface location [3,4,8,14,20,30,31]. The advantages of this combination are that nodal data is used to specify the geometry, changes in topology can be easily handled, and a fixed non-conforming finite element mesh is used for each deterministic solution. The X-FEM can be used with a stochastic sampling technique to solve the stochastic model problem without generating a conforming mesh for each sample. However, numerous deterministic solutions are required.

For problems where the solution of interest depends smoothly on random inputs, a more efficient and widely-used approach is the spectral stochastic finite element method (SSFEM) [6,9,11,38]. The input parameters are modeled as random variables, and the spatial approximation is augmented with a stochastic approximation. In SSFEM, the degrees of freedom in the probability domain are approximated with a truncated polynomial chaos (PC) expansion [9,11,35,38], and a Galerkin projection [40] is used to determine the coefficients. The result from SSFEM fully describes the numerical solution in terms of the random variables representing input uncertainties. The statistics of the quantity of interest, such as the mean, variance, and probability distribution, can be determined directly from the expansion coefficients or by sampling the random variables in the resulting polynomial solution. For the model problem (1), the non-smooth solution behavior in the probability domain may not be accurately captured by the spectral approximation using SSFEM. This may lead to non-convergent solutions and introduce numerical inaccuracies (e.g. Gibbs phenomenon). An alternative to the spectral approximation in the probability domain is a finite element approximation [6], which may better approximate the non-smooth solution by increasing the number of elements in the probability domain. However, the computational expense increases rapidly with the number of elements. In the work by Wan and Karniadakis [33], an adaptive multi-element PC approach is used to more efficiently address the non-smooth solution in the probability domain. The work by Le Maître et. al. [16,17] addresses capturing non-smooth solutions by using multi-wavelets.

The X-SFEM is a combined approach which extends the X-FEM to the stochastic framework [23]. The X-SFEM addresses the issue of capturing the non-smooth solution behavior in both the physical and probability domains. A non-conforming finite element mesh is used for the physical domain, where the non-smooth solution behavior is captured by an enrichment function. The X-FEM

spatial approximation results in degrees of freedom which are approximated in the probability domain. The spectral PC approximation is used for the probability domain, and through a proper enrichment the smoothness of the spatial degrees of freedom can be improved. The choice of the enrichment function is an important aspect in capturing the non-smooth behavior and leading to an efficient and accurate approximation. As with SSFEM, the numerical solution represents the response of interest as an explicit function of both the spatial and random variables. The X-SFEM is also applicable to other problems involving variation in geometry such as surface shape changes and moving boundary problems.

This paper presents in-depth studies of the accuracy and convergence of the X-SFEM solutions to the model problem defined in (1). Various enrichment functions, both standard and tailored to X-SFEM, are investigated. The solution accuracy and smoothness of the degrees of freedom as a function of the random variables describing the uncertain geometry are studied by solving multiple deterministic problems with X-FEM. In addition to the spectral approach considered in [22], the accuracy and efficiency of a finite element stochastic approximation is studied. The introduction of enrichment functions to capture non-smooth solutions results in integrals with non-smooth integrands in the spatial and probability domains. For accurate numerical integration in the probability domain, a partition approach is introduced which aligns with the regions where the integrand quantities are piecewise regular. The solution convergence using X-SFEM is investigated for the two-dimensional domain shown in Fig. 1 with geometric uncertainties described by one and two random variables. Based on observations from the behavior of the degrees of freedom and the solution convergence, the basic elements of a successful enrichment function in X-SFEM are identified.

The paper is outlined as follows: a basic description of the level set method, X-FEM, and SSFEM are provided in Sects. 2–4. Details of X-SFEM and computational considerations are described in Sect. 5. Numerical examples showing the behavior of X-FEM and results from X-SFEM are discussed in Sect. 6.

2 Level set method

The random inclusion geometry is described implicitly by the level set method [25]. While the level set method is often used to track moving interfaces on a fixed mesh [15,26,32,34], herein the level set method is used to define the location of the inclusion interface and its stochastic variability. The location of the interface $\Gamma(\boldsymbol{\xi})$ is implicitly defined by the iso-zero of a random level set function, $\phi(\boldsymbol{x}, \boldsymbol{\xi}) : \mathcal{D} \times \Omega \rightarrow \mathbb{R}$. The properties of $\phi(\boldsymbol{x}, \boldsymbol{\xi})$ are given by
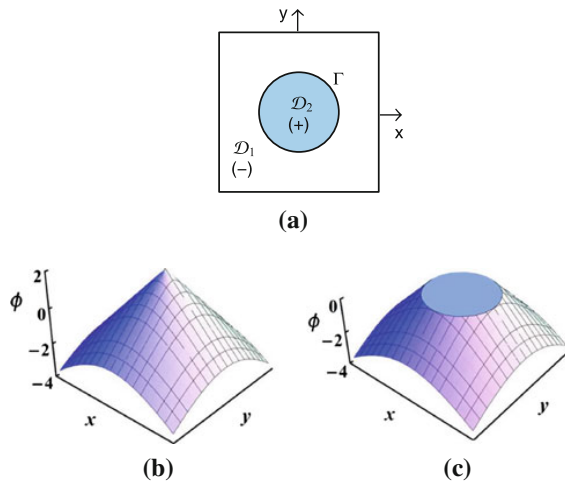
Fig. 2 The level set function for a (**a**) circular inclusion is a (**b**) cone, shown here with negative $(-)$ and positive $(+)$ value in $\mathcal{D}_1$ and $\mathcal{D}_2$, respectively. The iso-zero of the cone describes the inclusion geometry as shown in (**c**)

$$
\begin{aligned}
\phi(\boldsymbol{x}, \boldsymbol{\xi}) < 0 & \quad \text{if } \boldsymbol{x} \in \mathcal{D}_1(\boldsymbol{\xi}) \\
\phi(\boldsymbol{x}, \boldsymbol{\xi}) > 0 & \quad \text{if } \boldsymbol{x} \in \mathcal{D}_2(\boldsymbol{\xi}) \\
\phi(\boldsymbol{x}, \boldsymbol{\xi}) = 0 & \quad \text{if } \boldsymbol{x} \in \Gamma(\boldsymbol{\xi}) ,
\end{aligned}
\tag{3}
$$

where $\boldsymbol{\xi} : \Omega \to \mathbb{R}^d$ is a vector of random variables that describe the uncertainty of the inclusion geometry. The random level set function is discretized according to the finite element mesh of the spatial domain,

$$
\phi(\boldsymbol{x}, \boldsymbol{\xi}) = \sum_{i \in I} N_i(\boldsymbol{x}) \phi_i(\boldsymbol{\xi}) ,
\tag{4}
$$

where $N_i(\boldsymbol{x})$ are the finite element nodal basis functions, I is the set of all nodes in the finite element mesh of $\mathcal{D}$, and $\phi_i(\boldsymbol{\xi})$ is the random level set function at node i.

In this work, the signed distance function is used to define the level set function. The random level set functions at each node are given by

$$
\phi_i(\boldsymbol{\xi}) = \pm \min \|\boldsymbol{x}_i - \boldsymbol{x}_\Gamma(\boldsymbol{\xi})\| ,
\tag{5}
$$

where $\boldsymbol{x}_\Gamma(\boldsymbol{\xi})$ is the interface location and $\|\cdot\|$ denotes the L^2-distance in the physical space. The sign of $\phi_i(\boldsymbol{\xi})$ is negative in $\mathcal{D}_1$ and positive in $\mathcal{D}_2$. An example of the level set function for a circular inclusion is shown in Fig. 2. In this example, the circular inclusion is one possible outcome (realization) of the random geometry, and in this case the level set function represents a cone. The iso-zero of the level set function defines the boundary of the circular inclusion.

To construct $\phi_i(\boldsymbol{\xi})$ in the numerical examples that follow, the interface location is defined as a function of the random variables, $x_\Gamma(\boldsymbol{\xi})$. At each node in the finite element mesh, realizations of $\phi_i(\boldsymbol{\xi})$ are computed according to the signed

distance function in (5). An approach to construct the random level set function for a more realistic application is to collect a set of images that capture the variation in geometry being modeled. The random level set function is then defined using the approach outlined in [29].

3 Extended finite element method (X-FEM)

In this section, we consider solving the deterministic model problem for a particular realization of the random inclusion geometry. That is, the inclusion geometry is specified by particular values of $\boldsymbol{\xi}$. To accurately capture non-smooth solutions resulting from material interfaces, the traditional finite element method (FEM) requires a mesh that conforms to the inclusion geometry. The Extended Finite Element Method (X-FEM) eliminates the requirement of a conforming mesh by enriching the traditional FEM approximation with a suitably constructed enrichment function [19,31].

For the approximation of the solution, we introduce the weak formulation of the model problem. Let $u \in V$ be the solution and $v \in V_0$ an admissible test function. The space $V = H^1(\mathcal{D})$ is the Hilbert space consisting of functions with square integrable first derivatives and $V_0 = \{v \in H^1(\mathcal{D}), v|_{\Gamma_D} = 0\}$. The weak form of the deterministic model problem is stated as: Find $u \in V$ such that $u = u_s$ on Γ_D and

$$
\int_{\mathcal{D}} (k \nabla u)^T \nabla v \, d\boldsymbol{x} = \int_{\mathcal{D}} f v \, d\boldsymbol{x} + \int_{\Gamma_N} q_s v \, ds \quad \forall v \in V_0 ,
\tag{6}
$$

where s denotes the boundary of $\mathcal{D}$. Consider a finite element mesh, $\mathcal{T}_h$, for the domain $\mathcal{D}$ which consists of elements that do not necessarily conform to the interface Γ. The X-FEM approximation $\hat{u}(\boldsymbol{x})$ of the solution $u(\boldsymbol{x})$ is

$$
\hat{u}(\boldsymbol{x}) = \sum_{i \in I} N_i(\boldsymbol{x}) u_i + \sum_{i \in I^*} N_i(\boldsymbol{x}) \Psi(\boldsymbol{x}) a_i ,
\tag{7}
$$

where $\Psi(\boldsymbol{x})$ is an enrichment function. In this work, we use bilinear nodal basis functions for $N_i(\boldsymbol{x})$. The set I contains all the nodes in $\mathcal{T}_h$, and the set $I^* \subseteq I$ contains the enriched nodes. The set of enriched nodes are determined by the intersection of the interface and the support of the enriched nodal basis functions, $N_i(\boldsymbol{x}) \Psi(\boldsymbol{x})$, and therefore depend on the choice of the enrichment function. In other words,

$$
I^* = \{i \in I : \mathcal{S}_i \cap \Gamma \neq \emptyset\} ,
\tag{8}
$$

where $\mathcal{S}_i$ denotes the support of the enriched nodal basis function at node i. The first term in (7) is the standard FEM approximation. The second term in (7) is added to capture the non-smooth solution at material interfaces. The unknowns, u_i and a_i, are referred to as regular and enriched degrees of freedom, respectively.
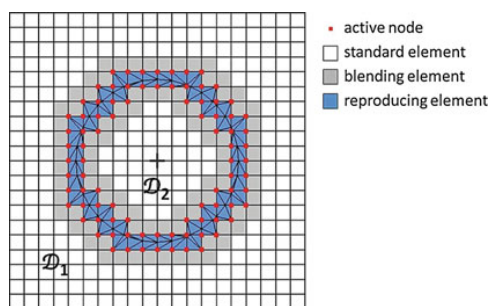
Fig. 3 Illustration of X-FEM terminology and the triangulation of intersected elements for a circular inclusion

The a priori knowledge of the interface location is incorporated into the enrichment function by defining $\Psi(\boldsymbol{x})$ as a function of $\phi(\boldsymbol{x})$. Since the solution for the model problem has a discontinuous first derivative at the interface, a natural choice for the enrichment function is the absolute value of the level set function. In this work, we implement various C^0-continuous enrichment functions, which satisfy continuity of the solution across the interface. Enrichment functions that are not C^0-continuous require a constraint equation to enforce continuity of the solution across the interface.

The following defines some common X-FEM terminology used throughout this paper. Active nodes refer to the nodes of intersected elements, as shown in Fig. 3 for a circular inclusion. Reproducing elements have all active nodes, standard elements have no active nodes, and blending elements have some active and some non-active nodes. Typically, I^* is defined as either the nodes of reproducing elements or the nodes of reproducing and blending elements. A discussion of possible issues with the approximation in blending elements and a general approach for modifying enrichment functions to avoid such issues is presented in [8].

To construct the system of equations, the approximation in (7) is substituted into the weak form (6). Following the Bubnov–Galerkin method, the test functions v are defined using the same basis functions as $N_i(\boldsymbol{x})$. The integration in (6) is performed over each element and assembled to form the system of equations. In intersected elements, $N_i(\boldsymbol{x})\Psi(\boldsymbol{x})$ is non-smooth by construction. For an accurate integration over an intersected element, we partition the element domain by a triangulation for piecewise integration. The triangulation for a circular inclusion with a finite element mesh constructed from recangular elements is shown in Fig. 3. The triangulation is only used to perform numerical integration and does not insert any additional degrees of freedom.

To solve the stochastic model problem, a MC simulation (or other stochastic sampling technique) can be used with X-FEM to repeatedly solve the deterministic problem for realizations of the interface geometry. The advantage of X-FEM is that conforming meshes are not generated for each

realization. However, computational costs can become prohibitive as numerous solutions are required due to the weak convergence of MC sampling.

4 Spectral stochastic finite element method (SSFEM)

In this section, we describe solving the model problem using the Spectral Stochastic Finite Element Method. SSFEM, introduced by Ghanem and Spanos [11] and later extended by [38] among others, is an approach for modeling systems with random parameters within the FE framework. The semi-discretized form of the model problem (1) is given by

$$\boldsymbol{K}(\boldsymbol{\xi})\boldsymbol{u}(\boldsymbol{\xi}) - \boldsymbol{f}(\boldsymbol{\xi}) = 0, \tag{9}$$

where $\boldsymbol{K}$ and $\boldsymbol{f}$ are the FE conduction matrix and load vector. The element conduction matrix $\boldsymbol{K}^e$ and load vector $\boldsymbol{f}^e$ are assembled to form $\boldsymbol{K}$ and $\boldsymbol{f}$. The vector $\boldsymbol{u}$ represents the nodal degrees of freedom of the FE approximation. The number of degrees of freedom is denoted by N. The system of equations in (9) is dependent on the input uncertainty defined by the random vector $\boldsymbol{\xi}$. Each component of the unknown vector $\boldsymbol{u}$ is approximated in the stochastic space using a PC expansion defined by

$$u_i(\boldsymbol{\xi}) = \sum_{j=1}^{M} H_j(\boldsymbol{\xi}) a_j^i, \tag{10}$$

where H_j are polynomials selected from the Wiener–Askey family [38], and a_j^i are the expansion coefficients to be determined. The Wiener–Askey family is a collection of polynomials which form an orthogonal basis of $L^2(\Omega)$ with respect to the probability density function of $\boldsymbol{\xi}$.

In the numerical examples of this work, random variables with independent uniform distributions, $U(-1, 1)$, are considered. Multi-dimensional Legendre polynomials form an orthogonal basis with respect to the uniform measure $P_{\boldsymbol{\xi}}(\boldsymbol{\xi}) = (\frac{1}{2})^d I_{[-1,1]^d}$, where $I_{[-1,1]^d}$ is the indicator set of the hypercube $[-1, 1]^d$ with d random variables. In other words,

$$\langle H_i, H_j \rangle = \int_{[-1,1]^d} H_i(\boldsymbol{\xi}) H_j(\boldsymbol{\xi}) P_{\boldsymbol{\xi}}(\boldsymbol{\xi}) d\boldsymbol{\xi} = \langle H_i^2 \rangle \delta_{ij}, \tag{11}$$

where δ_{ij} denotes the Kronecker delta, and $\langle \cdot \rangle$ denotes the mathematical expectation operator. The multi-dimensional basis functions, $\boldsymbol{H}(\boldsymbol{\xi})$, are constructed from the product of the one-dimensional Legendre polynomials [36]. The total order of each polynomial product is less than or equal to $p \in \mathbb{N} \cup \{0\}$, the order of the approximation.

The number of terms in the PC expansion, M, is determined by

$$M = \frac{(p+d)!}{p!d!}. \tag{12}$$

The polynomial expansion of u in (10) is introduced into the FE system of (9), and the Galerkin projection of the residual in the space spanned by $\{H_i(\boldsymbol{\xi})\}_{i=1}^M$ leads to the coupled system of equations for the vector of coefficients $\boldsymbol{a}_j$, i.e.,

$$\sum_{j=1}^M \langle \boldsymbol{K}(\cdot) H_j(\cdot) H_k(\cdot) \rangle \boldsymbol{a}_j \\ - \langle \boldsymbol{f}(\cdot) H_k(\cdot) \rangle = \boldsymbol{0}, \quad k = 1, \ldots, M. \tag{13}$$

The $(M \cdot N) \times (M \cdot N)$ system of equations is rewritten in compact form as

$$\boldsymbol{K}_s \hat{\boldsymbol{a}} - \boldsymbol{f}_s = \boldsymbol{0}, \tag{14}$$

where the vector $\hat{\boldsymbol{a}}$ collects all the expansion coefficients $\boldsymbol{a}_j$ of $\boldsymbol{u}(\boldsymbol{\xi})$. The matrix $\boldsymbol{K}_s$ and vector $\boldsymbol{f}_s$ are assembled from each spatial element integrated over the space of random variables. Each (j, k) block of the element matrix $\boldsymbol{K}_s^e$ is defined as

$$(\boldsymbol{K}_s^e)_{jk} = \langle \boldsymbol{K}^e(\cdot) H_j(\cdot) H_k(\cdot) \rangle, \quad j, k = 1, \ldots, M, \tag{15}$$

and each kth sub-vector component of $\boldsymbol{f}_s^e$ is defined as

$$(\boldsymbol{f}_s^e)_k = \langle \boldsymbol{f}^e(\cdot) H_k(\cdot) \rangle, \quad k = 1, \ldots, M. \tag{16}$$

For the case $u_i(\boldsymbol{\xi}) \in L^2(\Omega)$ smooth with respect to $\boldsymbol{\xi}$, the Wiener-Askey PC expansion converges in the mean-square sense [38], and the convergence rate may be exponential if $u_i(\boldsymbol{\xi})$ is analytic with respect to $\boldsymbol{\xi}$ [2]. However, for non-smooth $u_i(\boldsymbol{\xi})$ with respect to $\boldsymbol{\xi}$, the Wiener-Askey PC expansion may converge slowly or even fail to converge due to the Gibbs phenomenon. For the semi-discretized form of the model problem (9), $u_i(\boldsymbol{\xi})$ is non-smooth due to, for instance, the uncertainty in the inclusion geometry. Some modified approaches which address the poor convergence of SSFEM include multi-element generalized PC [33] and multi-wavelets [17]. For this work, the SSFEM approximation is combined with the X-FEM spatial approximation, which is described in the next section.

5 Extended stochastic finite element method (X-SFEM)

X-SFEM is a combined approach based on X-FEM and SSFEM for solving stochastic partial differential equations on random domains [22,24]. In X-SFEM, the non-smooth solution at the material interface is captured with a suitable choice for the enrichment function, and the stochastic response is approximated with SSFEM. The uncertain interface location is defined by the random level set function $\phi(\boldsymbol{x}, \boldsymbol{\xi})$. The numerical solution is an explicit function of the random variables, allowing fast post-processing to determine statistical moments and probability distributions for the quantities of interest.

5.1 Approximation

Approximate solutions are sought for the weak form of the stochastic model problem stated as: find $u \in L^2(\Omega; V)$ such that

$$\left\langle \int_{\mathcal{D}} (k \nabla u)^T \nabla v \, d\boldsymbol{x} \right\rangle = \left\langle \int_{\mathcal{D}} f v \, d\boldsymbol{x} + \int_{\Gamma_N} q_s v \, ds \right\rangle \\ \forall v \in L^2(\Omega; V_0), \tag{17}$$

where $L^2(\Omega; V)$ is a Hilbert space of $H^1(\mathcal{D})$-valued random fields with finite second moments, and V is defined in (3).

In the X-SFEM approach, the enrichment function and the degrees of freedom resulting from the spatial approximation (7) are functions of the random variables. The X-SFEM approximation of $u(\boldsymbol{x}, \boldsymbol{\xi})$ is defined as

$$\hat{u}(\boldsymbol{x}, \boldsymbol{\xi}) = \sum_{i \in I} N_i(\boldsymbol{x}) u_i(\boldsymbol{\xi}) + \sum_{i \in I^*} N_i(\boldsymbol{x}) \Psi(\boldsymbol{x}, \boldsymbol{\xi}) a_i(\boldsymbol{\xi}), \tag{18}$$

where a spectral approximation is made for the regular degrees of freedom $u_i(\boldsymbol{\xi})$ and the enriched degrees of freedom $a_i(\boldsymbol{\xi})$ in the probability domain. The definition of the enrichment function, $\Psi(\boldsymbol{x}, \boldsymbol{\xi})$, incorporates the random level set function (4). The uncertain location of the interface is accounted for in the enrichment function, allowing the approximation to capture solution irregularities in the spatial and probability domains. Here, the set I contains all nodes in the finite element mesh of $\mathcal{D}$, and $I^* \subseteq I$ contains the enriched nodes which must consider the possible locations of the random interface. The set I^* is dictated by the particular choice of enrichment function and is defined in Sect. 5.2 for each enrichment function explored in this work.

As in SSFEM, the spectral approximation for the regular and enriched degrees of freedom is defined as

$$u_i(\boldsymbol{\xi}) = \sum_{j=1}^M u_j^i H_j(\boldsymbol{\xi}) \quad \text{and} \quad a_i(\boldsymbol{\xi}) = \sum_{j=1}^M a_j^i H_j(\boldsymbol{\xi}), \tag{19}$$

where u_j^i and a_j^i are the PC expansion coefficients and $H_j(\boldsymbol{\xi})$ are spectral polynomials defined in Sect. 4.

It will be shown in Sects. 6.1 and 6.2 that the regular and enriched degrees of freedom may strongly oscillate with respect to the random variables. In this case, a finite element approximation in the probability domain may be better suited than a spectral approximation. Consider a finite element mesh, $\mathcal{T}_{h_s}^S$, of the probability domain Ω, where Ω here is the hypercube $[-1, 1]^d$. The linear FE approximation for the regular and enriched degrees of freedom in (18) is defined as

$$u_i(\boldsymbol{\xi}) = \sum_{j \in J} u_j^i N_j(\boldsymbol{\xi}) \quad \text{and} \quad a_i(\boldsymbol{\xi}) = \sum_{j \in J^*} a_j^i N_j(\boldsymbol{\xi}), \tag{20}$$

where N_j are linear FE nodal basis functions. The set J contains all nodes belonging to $\mathcal{T}_{h_s}^S$, and $J^* \subset J$ contains the

enriched nodes. The enriched nodes are the nodes of the elements in $\mathcal{T}_{h_s}^S$ which contain a value of $\boldsymbol{\xi}$ for which the spatial element is intersected. The number of unknown coefficients for the regular degrees of freedom, u_j^i, is equal to the number of nodes in $\mathcal{T}_{h_s}^S$. The number of unknown coefficients for the enriched degrees of freedom, a_j^i, depends on the choice of enrichment function. We use a uniform mesh for Ω and piecewise integration over the probability domain. A drawback of the linear FE approximation in the probability domain is that more unknowns may be required than for a spectral approximation when the degrees of freedom in (18) vary smoothly with the random parameters.

5.2 Enrichment functions

We compare the performance of four enrichment functions for X-SFEM. The first is the absolute value of the level set function [31] extended to the stochastic framework, defined as

$$\Psi_1(\boldsymbol{x}, \boldsymbol{\xi}) = |\phi(\boldsymbol{x}, \boldsymbol{\xi})| = \left| \sum_{i \in I} N_i(\boldsymbol{x}) \phi_i(\boldsymbol{\xi}) \right|. \tag{21}$$

The set I^* in (18) is defined as the set of nodes of all elements possibly intersected by the interface resulting from the random variation of the inclusion geometry. The support of $\Psi_1(\boldsymbol{x}, \boldsymbol{\xi})$ is the entire probability domain Ω for each spatial element. The Ψ_1 enrichment is a straightforward approach, but as shown in [20] convergence with spatial mesh refinement is not optimal for a deterministic analysis. As discussed in [8], the suboptimal convergence is due to problems in blending elements. However, it is included in this work to study and compare its performance in X-SFEM.

The second enrichment function is the deterministic enrichment proposed by Moës et al. [20] extended to the stochastic framework, defined as

$$\Psi_2(\boldsymbol{x}, \boldsymbol{\xi}) = \sum_{i \in I} N_i(\boldsymbol{x}) |\phi_i(\boldsymbol{\xi})| - |\phi(\boldsymbol{x}, \boldsymbol{\xi})|. \tag{22}$$

The set of enriched nodes I^* in (18) is defined as the set of nodes of all elements possibly intersected by the inclusion interface for the Ψ_2 enrichment (as in the absolute value enrichment). For a deterministic analysis, optimal convergence with mesh refinement is recovered using the Ψ_2 enrichment function [20]. The value of Ψ_2 is zero at all nodes. Therefore the regular degrees of freedom coincide with the solution value at the nodes according to (18). However, as it is shown later the regular and enriched degrees of freedom are non-smooth in the probability domain, which leads to poor convergence for a spectral PC approximation. Also, elements with small areas of intersection may lead to ill-conditioned systems. In a deterministic analysis, mesh refinement in regions near the interface will mitigate the

ill-conditioning issue as well as improve the representation of the inclusion geometry. In order to address this issue for a stochastic analysis, mesh refinement is needed in regions near all possible interface locations.

The third enrichment function is the absolute value enrichment with the modification described in [8] and extended to the stochastic framework, defined as

$$(\Psi_3(\boldsymbol{x}, \boldsymbol{\xi}))_i = (|\phi(\boldsymbol{x}, \boldsymbol{\xi})| - |\phi_i(\boldsymbol{\xi})|) R(\boldsymbol{x}), \tag{23}$$

where

$$R(\boldsymbol{x}) = \left(\sum_{i \in I^+} N_i(\boldsymbol{x}) \right). \tag{24}$$

Here, I^+ is defined as the set of nodes belonging to the intersected elements determined by the value of $\boldsymbol{\xi}$. Therefore, I^+ changes with $\boldsymbol{\xi}$. The set of enriched nodes I^* in (18) is defined as the set of nodes of all elements with at least one node in the possible sets I^+. We note that $(\Psi_3(\boldsymbol{x}, \boldsymbol{\xi}))_i$ is a nodal enrichment, such that $\Psi(\boldsymbol{x}, \boldsymbol{\xi})$ in (18) is replaced by $(\Psi_3(\boldsymbol{x}, \boldsymbol{\xi}))_i$. The Ψ_3 enrichment does not exhibit the numerical issues of the Ψ_2 enrichment when elements have small areas of intersection. The regular degrees of freedom coincide with the solution value at the nodes for the Ψ_3 enrichment, and the inaccuracy of the solution in blending elements (for the Ψ_1 enrichment) are resolved by adding the ramp function, $R(\boldsymbol{x})$. The ramp function is one for intersected elements, zero for standard elements, and varies continuously between zero and one for a blending element.

The fourth enrichment function is one proposed by Nouy et al. [22] and is defined as

$$\Psi_4(\boldsymbol{x}, \boldsymbol{\xi}) = \begin{cases} \sum_{i \in I^+} N_i(\boldsymbol{x})(\beta + \phi_i(\boldsymbol{\xi})) & \text{if } \boldsymbol{x} \in \mathcal{D}_1(\boldsymbol{\xi}) \\ \sum_{i \in I^+} N_i(\boldsymbol{x})(\beta - \phi_i(\boldsymbol{\xi})) & \text{if } \boldsymbol{x} \in \mathcal{D}_2(\boldsymbol{\xi}), \end{cases} \tag{25}$$

where

$$\beta \approx \sup_{i \in I^*} |\phi_i(\boldsymbol{\xi})|. \tag{26}$$

Here I^+ is defined as the set of nodes of all elements possibly intersected as a result of random variation of the inclusion geometry. The value of the constant β is chosen to improve the condition number of the system of equations. The set of enriched nodes I^* in (18) and (26) includes the set I^+ and the nodes of the blending elements for I^+. The support of $\Psi_4(\boldsymbol{x}, \boldsymbol{\xi})$ is the entire probability domain for each spatial element possibly intersected and the blending elements. Elements with small intersected areas do not cause numerical issues. Finally, the regular and enriched degrees of freedom are smooth in the probability domain, for which a spectral PC approximation is well suited.
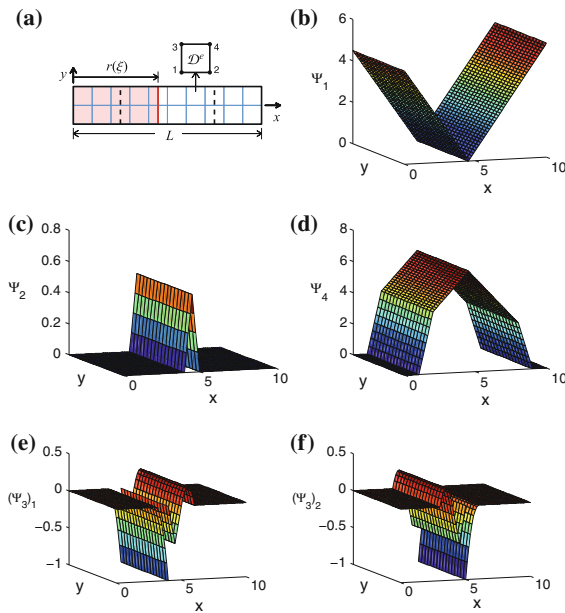
Fig. 4 (**a**) Random inclusion geometry and element node numbers for visualizing the enrichment functions. Realization of the (**b**) Ψ_1, (**c**) Ψ_2, (**d**) Ψ_4, and (**e**–**f**) Ψ_3 enrichment functions

A realization of the four enrichment functions for a bar with a vertical interface is shown in Fig. 4. The location of the interface is $x_\Gamma = r(\xi)$, where $r = 5 + 2.5\xi$ and ξ has a uniform distribution $U(-1, 1)$. The bar is shown with $L = 10$ and a mesh size of $h = 1$. The inclusion geometry for $r = 4.5$ is shaded, and the dashed lines represent the variation of the interface location with respect to ξ. The enrichment functions are shown for the interface location at $r = 4.5$. The Ψ_1 enrichment is zero on the interface and non-zero everywhere else in the domain. The Ψ_2 enrichment is nonzero only for an intersected element. The Ψ_3 enrichment is nonzero for an intersected element plus its blending element, and is defined for each node. The Ψ_4 enrichment is defined over the elements which are possibly intersected plus the blending elements. The Ψ_3 enrichment at node i is denoted by $(\Psi_3)_i$. The node numbers for the four node quadrilateral element is shown in Fig. 4a. In this example, there is no variation in the y-direction of the enrichment functions. Therefore $(\Psi_3)_1 = (\Psi_3)_3$ and $(\Psi_3)_2 = (\Psi_3)_4$. The Ψ_3 enrichment is shown for nodes 1 and 2.

Remark 1 More detailed interpretations of applying the different enrichment functions in X-SFEM, as well as using the spectral PC and linear FE approximation in the probability domain, have been deferred to the numerical examples in Sect. 6.
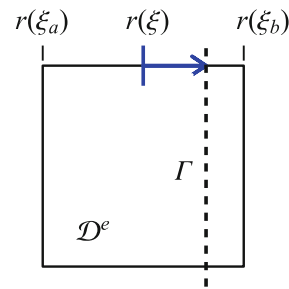
Fig. 5 Spatial element with a vertical interface determined by one random parameter

5.3 Numerical integration

To compute the matrix K_s and vector f_s in (14), the element quantities K_s^e and f_s^e in (15) and (16) are computed by integrating over the spatial and probability domains. The integration is performed for each spatial element, and the element quantities are assembled to construct the system of equations. For the spectral PC approximation of the degrees of freedom (19), the integration is performed over the entire probability domain. For the finite element approximation of the degrees of freedom (20), the integration is performed over each element in $\mathcal{T}_{h_s}^S$ and assembled to compute K_s^e and f_s^e.

The dependence of $K^e(\xi)$ and $f^e(\xi)$ on ξ is piecewise smooth. As described for X-FEM, a partition of the spatial domain for an intersected element is required for accurate integration. In addition, careful numerical integration over the probability domain is also required in X-SFEM. Due to the piecewise behavior, a partition of the probability domain is created in order to accurately integrate $K^e(\xi)$ and $f^e(\xi)$. The partition is only used to subdivide the probability domain for specifying integration points and does not produce any additional degrees of freedom. The appropriate quadrature points are specified per subdivision in order to accurately compute the integral.

To illustrate the dependence of $K^e(\xi)$ on ξ, consider the spatial element in Fig. 5. The location of the vertical interface, $r(\xi)$, depends on one random parameter and possibly extends beyond the boundaries of the element. The interface defines the boundary between different material conductivities. The matrix $K^e(\xi)$ is defined as

$$K^e(\xi) = \int_{\mathcal{D}^e} B(x)^T k(x, \xi) B(x) dx. \qquad (27)$$

Here we consider the matrix entries, $K_{ij}^e(\xi)$, with $(i, j) = 1, \ldots, 4$, corresponding to the regular degrees of freedom. Therefore $B(x)$ in (27) consists of the derivatives of $N_i(x)$. Assume the element is intersected for $\xi_a < \xi < \xi_b$, hence $r(\xi_a)$ and $r(\xi_b)$ correspond to interface locations at the left and right element edges, respectively. The $K_{ij}^e(\xi)$ are shown in Fig. 6 as functions of ξ, where $i = j$ and $i \neq j$
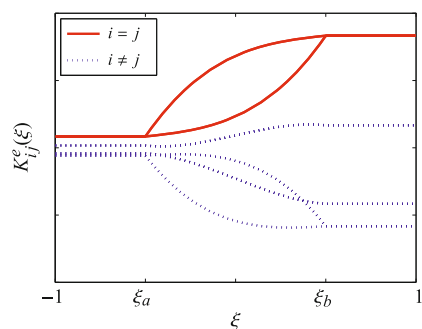
Fig. 6 The $K^e(\xi)$ entries as a function of ξ

represent the diagonal and off-diagonal entries, respectively. The $K_{ij}^e(\xi)$ are constant when the element is not intersected and vary between the constant states when intersected. For this illustration, the three subdivisions $\xi < \xi_a, \xi_a < \xi < \xi_b$, and $\xi > \xi_b$ align with the regions where $K^e(\xi)$ is smooth.

The nodal level set functions of each spatial element, $\phi_i(\boldsymbol{\xi})$, can be used to determine an appropriate partition of the probability domain. The partition should align with $\phi_i(\boldsymbol{\xi}) = 0$, which indicates where the interface intersects a node. The approach suggested in [24] uses a Cartesian mesh to partition the probability domain for a spectral PC approximation of the degrees of freedom. Recursive splitting is used to locally refine regions where $\phi_i(\boldsymbol{\xi}) = 0$. The level of refinement is specified to control the number of partitions and the accuracy of the alignment with $\phi_i(\boldsymbol{\xi}) = 0$. In this work, we use the union of $\phi_i(\boldsymbol{\xi}) = 0$ for each node of $\mathcal{D}^e$ and a Delaunay triangulation to minimize the number of required partitions for $d \geq 2$. For the case $d = 1$, $\phi_i(\xi) = 0$ correspond to points in the probability domain which define the partition. If the random level set function is constructed using a Karhunen–Loève expansion (as in the case of using material images [29]), then $\phi_i(\boldsymbol{\xi})$ may be linear with respect to $\boldsymbol{\xi}$. In this case, a triangulated partition will align with $\phi_i(\boldsymbol{\xi}) = 0$ with a low number of subdivisions. For the case when $\phi_i(\boldsymbol{\xi})$ is not linear with respect to $\boldsymbol{\xi}$, creating a triangulated partition is more complex than constructing the Cartesian mesh with recursive splitting.
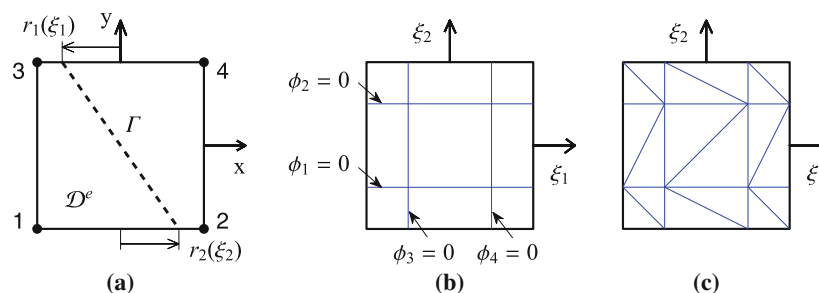
For the example shown in Fig. 5 with $d = 1$, there are two locations where the interface intersects a node (which in this case correspond to intersecting an edge). These two locations, ξ_a and ξ_b, define the three subdivisions of the probability domain.

As an example of the triangulated partition for two random variables, consider the spatial element in Fig. 7. The slanted interface location is determined by two random variables, ξ_1 and ξ_2. If ξ_1 and ξ_2 have uniform distributions $U(-1, 1)$, $r_1(\xi_1) = 2\xi_1$, $r_2(\xi_2) = 2\xi_2$, and the element domain is $\mathcal{D}^e = (-1, 1) \times (-1, 1) \subset \mathbb{R}^2$, then four lines in the probability domain define $\phi_i(\boldsymbol{\xi}) = 0$, as illustrated. The union of these lines create nine regions of the probability domain. As the four lines represent the zero value of $\phi_i(\boldsymbol{\xi})$, each of the nine regions have unique combinations of positive and negative $\phi_i(\boldsymbol{\xi})$. The subdivisions for piecewise integration are created by a Delaunay triangulation of the nine regions.

6 Numerical examples

The performance of the four enrichment strategies and stochastic approximation techniques will be examined in this section. The examples considered are steady state heat conduction problems with no internal heat generation ($f = 0$ in (1)) in a two-dimensional domain with a material inclusion. The probabilistic description of the material interface location is assumed to be known for each example and is defined by the random parameters $\boldsymbol{\xi}$. Consistent units are assumed for the parameters used in the examples.

6.1 Example 1

The first numerical example is the heat conduction problem shown in Fig. 8. The example consists of a bar of length $L = 20$ with a center inclusion. The material interface is determined by the length of the inclusion, described by one random variable. The length of the inclusion is $2r$, where $r = 5 + 2.5\xi$ and ξ has a uniform distribution $U(-1, 1)$. In Fig. 8, the dashed lines represent the variation of each interface location, and the inclusion geometry for $r = 5.5$
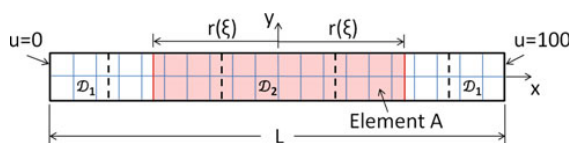
Fig. 7 (**a**) Spatial element with a slanted interface defined by two random variables. (**b**) Regions of the probability domain defined by $\phi_i(\boldsymbol{\xi}) = 0$. (**c**) The probability domain is triangulated for numerical integration

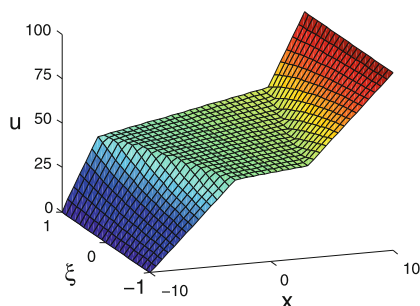**Fig. 8** Problem description for Example 1

Fig. 9 Analytical solution for Example 1

is shaded. Material 1 has conductivity $k_1 = 2$ in $\mathcal{D}_1$ and material 2 (inclusion) has conductivity $k_2 = 20$ in $\mathcal{D}_2$. The temperature is fixed at $u = 0$ on the left edge and $u = 100$ on the right edge. The top and bottom edges are adiabatic. The spatial mesh consists of square elements of size $h = 1$. We note that the spatial approximation is converged for this mesh size.

Since the material interfaces are vertical and the top and bottom edges are adiabatic, the solution is one-dimensional in the spatial domain. This example was chosen because an analytical solution exists for any realizations of ξ, and details of the numerical approach can be easily visualized. The analytical solution is shown as a function of $\boldsymbol{x} = (x, 0)$ and ξ in Fig. 9. The analytical solution is piecewise smooth in the spatial and probability domains.

Before assessing the performance of X-SFEM with the different enrichment functions, it is instructive to examine the behavior of the solution and the spatial degrees of freedom in the probability domain. Deterministic X-FEM solutions are computed for a number of realizations of

the inclusion geometry starting with $\xi = -1$ ($r = 2.5$) and ending with $\xi = 1$ ($r = 7.5$) with a step size of $\Delta \xi = 0.05$. The values of the degrees of freedom and solution for the node at $\boldsymbol{x} = (5, 0)$ are shown in Fig. 10. Each line in the graph corresponds to a different enrichment function. Each symbol on a line represents an X-FEM solution for a particular inclusion geometry. Note that the inclusion interface passes through the node at $\boldsymbol{x} = (5, 0)$ when $\xi = 0$. The regular and enriched degrees of freedom are non-smooth with respect to ξ for the Ψ_1, Ψ_2, and Ψ_3 enrichments. Both the regular and enriched degrees of freedom are smooth for the Ψ_4 enrichment. A spectral PC approximation will accurately capture the smooth behavior of the degrees of freedom for the Ψ_4 enrichment. However, a finite element approximation will be better suited to capture the non-smooth behavior of the degrees of freedom for the other enrichment functions. The regular degrees of freedom for the Ψ_2 and Ψ_3 enrichments correspond to the solution value at the node because the value of the enrichment function is zero at the node. The solution is accurately captured using the Ψ_2, Ψ_3, and Ψ_4 enrichments. The solution is not accurately captured by the Ψ_1 enrichment, confirming X-FEM results discussed in [8].

As discussed in Sect. 5.3, a partition is needed to accurately integrate over the probability domain to compute $\boldsymbol{K}_s^e$. The behavior of the $\boldsymbol{K}^e$ matrix as a function of ξ is examined for each enrichment function. The entries of $\boldsymbol{K}^e$ for element A (see Fig. 8) corresponding to the regular and enriched degrees of freedom as a function of the random variable are shown in Fig. 11, where $i = j$ and $i \neq j$ represent the diagonal and off-diagonal entries, respectively, and $(i, j) = 1, \ldots, 4$. The behavior of K_{ij}^e as a function of ξ is piecewise smooth. A partition of the probability domain which aligns with the regions where $\boldsymbol{K}^e$ is piecewise smooth allows efficient and accurate integration in (15). The $\boldsymbol{K}^e$ matrix entries corresponding to the regular degrees of freedom do not change with the choice of enrichment function. The $\boldsymbol{K}^e$ matrix entries corresponding to the coupled regular and enriched degrees of freedom are not shown, but they show a similar dependency on the
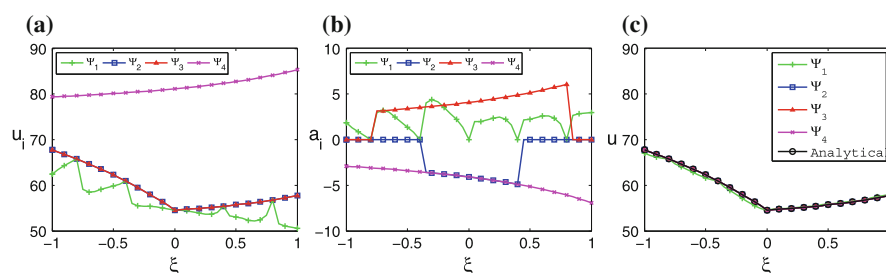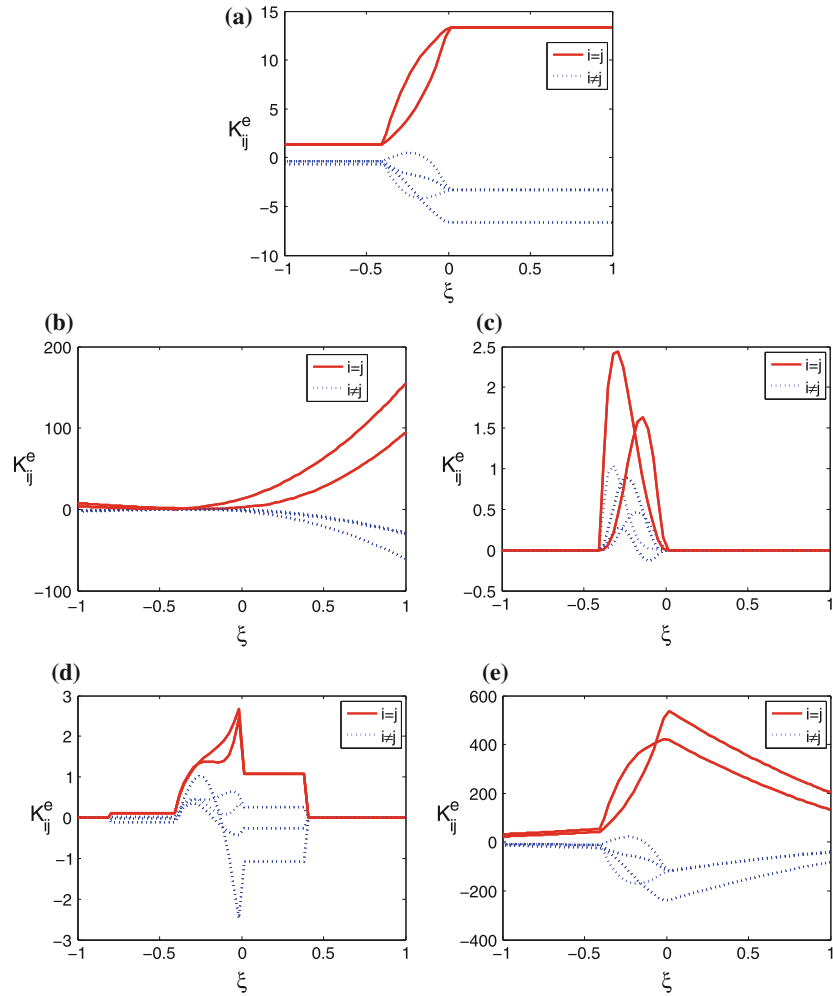

Fig. 10 The (**a**) regular DOF values, (**b**) enriched DOF values, and (**c**) solution at $\boldsymbol{x} = (5, 0)$ as a function of ξ for the different enrichment strategies for Example 1

Fig. 11 Dependency of K^e on the random variable for element A in Fig. 8 corresponding to the (**a**) regular degrees of freedom and the enriched degrees of freedom using the (**b**) Ψ_1, (**c**) Ψ_2, (**d**) Ψ_3, and (**e**) Ψ_4 enrichment strategies

random variable and thus the same partition is necessary for an accurate numerical quadrature.

For this example, the variation of K^e with respect to the random variable shown in Fig. 11 establishes the importance of partitioning the probability domain for integration. If the integration points are specified without a proper partition, sharp gradients or local behavior in the K^e matrix entries may not be captured. The system of equations may become singular if the interval of local behavior does not include any integration points. A proper partition allows a minimum number of quadrature points to be used for an accurate numerical integration.

The performance of X-SFEM can be assessed by examining the behavior of the error of X-SFEM solutions obtained with the different enrichment functions and the spectral PC and linear FE approximations in the probability domain.

Denoting an X-SFEM solution by $\hat{u}$ and the analytical solution by u, the relative error in the X-SFEM solution is given by

$$e = \frac{\|u - \hat{u}\|_{L^2(\Omega; L^2(\mathcal{D}))}}{\|u\|_{L^2(\Omega; L^2(\mathcal{D}))}}. \tag{28}$$

The convergence of the error in the X-SFEM solutions with respect to the order of the spectral PC approximation (p) is shown in Fig. 12 and with respect to the mesh size of the linear FE stochastic approximation (h_s) in Fig. 13. Each line in the figure corresponds to a different enrichment function. The approximate convergence rates are noted on the figures for the Ψ_2, Ψ_3, and Ψ_4 enrichment functions. The convergence rate for the Ψ_1 enrichment function is approximately zero and is not shown. The poor convergence for the Ψ_1 enrichment was expected from the behavior of the degrees
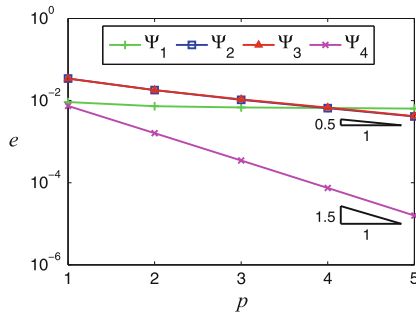
Fig. 12 Convergence of the relative error in $L^2(\Omega; L^2(\mathcal{D}))$ using a spectral PC stochastic approximation for Example 1

of freedom and the solution accuracy shown in Fig. 10. The convergence rates for the Ψ_2 and Ψ_3 enrichments improve using a linear FE stochastic approximation as compared to using the spectral PC approximation. The Ψ_4 enrichment has the highest convergence rate for both of the stochastic approximation techniques. For this example, a uniform stochastic mesh size of $h_s = 0.2/n$, for any positive integer n, aligns the stochastic elements with the variation of the degrees of freedom for enrichments Ψ_2 and Ψ_3. The misaligned stochastic mesh sizes chosen in Fig. 13a were $h_s \in \{1, 0.5, 0.25, 0.125, 0.0625\}$, and the aligned stochastic mesh sizes chosen in Fig. 13b were $h_s \in \{0.2, 0.1, 0.05\}$. The stochastic mesh size does not affect the convergence rate using the Ψ_1 and Ψ_4 enrichments. For an aligned stochastic mesh, the error using the Ψ_2 and Ψ_3 enrichments is similar to the Ψ_4 enrichment. Finally, the same level of error is achieved with the Ψ_4 enrichment for the spectral PC approximation using fewer degrees of freedom per node than the linear finite element approximation. The spectral PC approximation with $p = 5$ uses 12 degrees of freedom per enriched node while the linear FE approximation with $h_s = 0.05$ uses 82 degrees of freedom per enriched node. Note that the total number of degrees of freedom depends on the number of enriched nodes for each enrichment type. Therefore there is
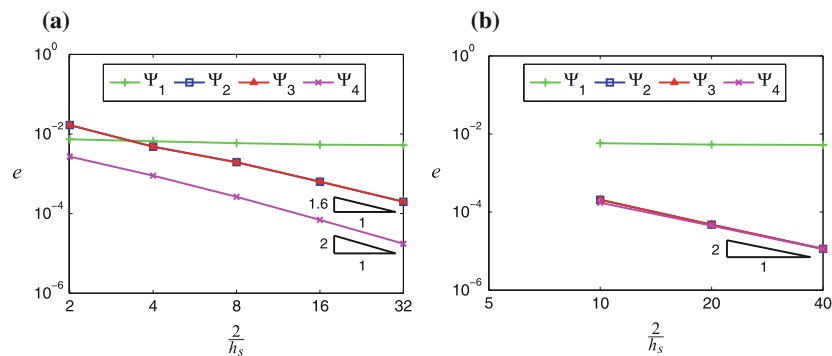
a difference whether or not the enriched nodes of the blending elements are included.

Example 1 provides a first insight into the characteristics of a successful enrichment function for X-SFEM with a spectral PC stochastic approximation. In order to achieve global smoothness of the degrees of freedom in the probability domain, $\Psi(x, \xi)$ should not be zero at all nodes. As seen with the Ψ_2 and Ψ_3 enrichments, if the enrichment function is zero at the nodes, the regular degrees of freedom will only be piecewise smooth. A finite element approximation in the probability domain can be used to capture the piecewise smooth behavior, but there may be a strong dependency of the accuracy of the approximation on the stochastic mesh. Also, for global smoothness the support of $\Psi(x, \xi)$ should include all possibly intersected elements plus blending elements for a given value of ξ. The blending elements are included to satisfy the partition of unity as discussed in [8], and the enrichment function should ramp to zero on the blending elements. The spectral PC approximation in the probability domain is as accurate and more efficient than a finite element approximation if the degrees of freedom are globally smooth. We note that these observations apply to C^0 continuous enrichment functions and may not apply to other types of enrichment.

6.2 Example 2

The second numerical example is the heat conduction problem shown in Fig. 14. The square domain $\mathcal{D} = (-10, 10) \times (-10, 10) \subset \mathbb{R}^2$ has a centered circular inclusion. The radius of the inclusion is determined by one random variable, $r = 5 + 2\xi$, in which ξ has a uniform distribution $U(-1, 1)$. In Fig. 14, the dashed lines represent the variation of the inclusion radius, and the inclusion material is shaded for $r = 4.75$. Material 1 has a conductivity $k_1 = 2$ in $\mathcal{D}_1$, and material 2 a conductivity $k_2 = 20$ in $\mathcal{D}_2$. The temperature is fixed at $u = 0$ on the left edge and $u = 100$ on the right edge. Adiabatic boundary conditions are enforced on the top and bottom edges. The purpose of this numerical example is to examine the effect of spatial mesh refinement on the smooth-
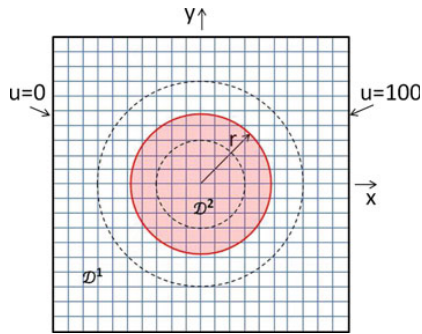
Fig. 13 Convergence of the relative error in $L^2(\Omega; L^2(\mathcal{D}))$ for a linear FE stochastic approximation for Example 1 using a (**a**) misaligned stochastic mesh and an (**b**) aligned stochastic mesh for Ψ_2 and Ψ_3

Fig. 14 Problem description for Example 2

ness of the degrees of freedom for the different enrichment functions.

In order to study the impact of spatial mesh refinement on the smoothness of the degrees of freedom as a function of ξ, the X-FEM solution was computed for multiple realizations of the inclusion geometry. A step size of $\Delta \xi = 0.001$ was used, and a deterministic X-FEM solution was computed for each of the realizations with four spatial mesh sizes h. Note that spatial mesh refinement improves simultaneously the resolution of the solution field and the resolution of the inclusion geometry since the level set function is discretized according to the finite element mesh (4). The values of the regular and enriched degrees of freedom for the node at $x = (5, 0)$ are shown for each enrichment function in Figs. 15, 16, 17 and 18 for different values of h. As more nodes are added by mesh refinement, some of the degrees of freedom show additional local minimum and maximum values. Here we consider the smoothness of the degrees of freedom to improve with spatial mesh refinement when the magnitudes of the local minimum and maximum values are reduced. The smoothness of both the regular and enriched degrees of freedom using the Ψ_1, Ψ_2, and Ψ_3 enrichments does not improve with spatial mesh refinement. Even for the Ψ_4 enrichment, the DOF values are not globally smooth functions of the random variable. However, spatial mesh refinement improves the smoothness of both the regular and enriched DOF values using the Ψ_4 enrichment.

For the Ψ_2 enrichment, elements with small areas of intersection led to an ill-conditioning of the system of equations resulting in solution inaccuracies. The Ψ_2 enrichment is local to an intersected element, and the magnitude of the enrichment approaches zero for small intersections. Therefore the contribution to the K matrix for the enriched degrees of freedom associated with the small intersected area will be almost zero. The ill-conditioning does not occur for the other enrichment strategies because the Ψ_1 and Ψ_4 enrichments are defined over all possibly intersected elements, and the Ψ_3 enrichment is defined over the intersected element plus the blending elements. Spatial mesh refinement reduces the

numerical inaccuracy for the Ψ_2 enrichment because the element areas formed by the intersection become more equal. The inaccuracies in the solution can be seen in Fig. 16a, as the regular DOF values are also the solution since $\Psi_2 = 0$ at a node. In Fig. 16b, the enriched DOF values are nonzero only when an element containing the node at $x = (5, 0)$ is intersected. The enriched DOF values exhibit jumps when the interface approaches a node. Note the vertical scale in Fig. 16b has been adjusted for the comparison using the different spatial mesh sizes, such that the minimum values are not shown. The jumps occur whenever the intersected area of an element is small. The ill-conditioning is handled in the deterministic case by refining the spatial mesh near the interface. When working problems for uncertain geometry, local mesh refinement would be needed for all regions where the intersection may occur. The Ψ_2 enrichment is not well suited for problems with uncertain geometry and will not be considered in the remainder of this paper.

In order to study the impact of the smoothness of the degrees of freedom on the approximate solution, the relative error in the energy norm of the X-SFEM solution from the spectral PC and linear FE stochastic approximation is compared. The energy norm of the stochastic solution is defined as

$$\|u\|_E^2 = \left\langle \int_{\mathcal{D}} (\kappa \nabla u)^T \nabla u \, dx \right\rangle = u^T K_s u . \tag{29}$$

Since an analytical solution is not available for this example, a reference value is computed as the mean of the energy norm of multiple X-FEM solutions using a MC simulation. The X-FEM solution using the Ψ_1, Ψ_3, and Ψ_4 enrichment functions converges as the spatial mesh is refined, but the convergence rate varies because the approximation spaces are different. Therefore a reference value for each enrichment function is computed using a spatial mesh size of $h = 0.25$ and a converged MC simulation with 150,000 samples. A measure for the accuracy of the X-SFEM approximation using the energy norm is computed as

$$\varepsilon_E = \frac{\|\hat{u}\|_E}{\|u_{ref}\|_E} , \tag{30}$$

where $\|u_{ref}\|_E$ is the MC based reference energy norm. The reference energy norm values for the Ψ_1, Ψ_3, and Ψ_4 enrichment strategies are 168.605, 168.490, and 168.505, respectively. The 95 % confidence intervals for the mean values for each enrichment function are $\pm$ 0.0672. The reference values are not identical for the different enrichment strategies because the spatial mesh is not converged. The spatial mesh size used for the reference value was limited by the available computational resources. Therefore ε_E as defined in (30) is not a true indicator of the error. However it provides a comparative measure for the accuracy of the X-SFEM solution using the different enrichment functions. Note that a value

Fig. 15 (**a**) Regular and (**b**) enriched degrees of freedom for the node at $\boldsymbol{x} = (x, y) = (5, 0)$ with respect to ξ using the Ψ_1 enrichment from X-FEM for Example 2. Here h denotes the length of elements along the x and y directions
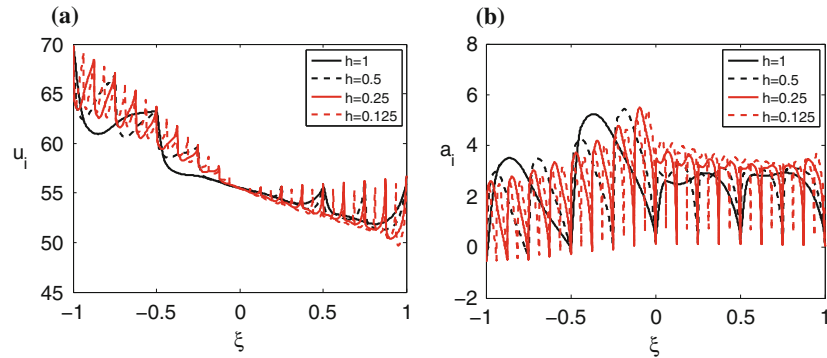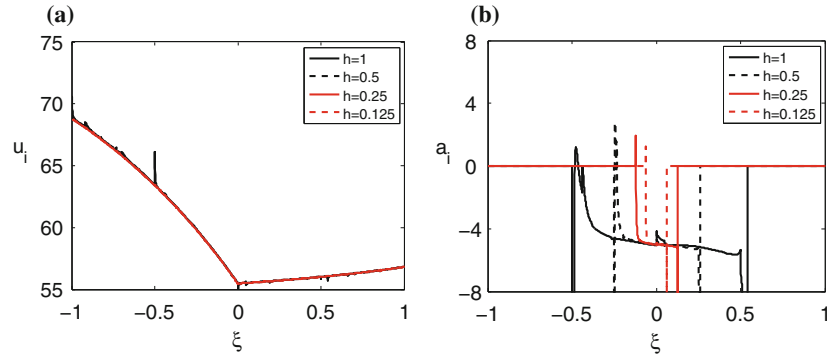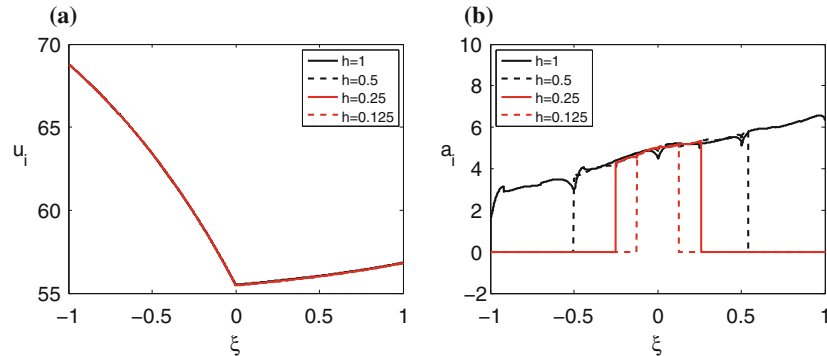

Fig. 16 (**a**) Regular and (**b**) enriched degrees of freedom for the node at $\boldsymbol{x} = (x, y) = (5, 0)$ with respect to ξ using the Ψ_2 enrichment from X-FEM for Example 2. Here h denotes the length of elements along the x and y directions

Fig. 17 (**a**) Regular and (**b**) enriched degrees of freedom for the node at $\boldsymbol{x} = (x, y) = (5, 0)$ with respect to ξ using the Ψ_3 enrichment from X-FEM for Example 2. Here h denotes the length of elements along the x and y directions

Fig. 18 (**a**) Regular and (**b**) enriched degrees of freedom for the node at $\boldsymbol{x} = (x, y) = (5, 0)$ with respect to ξ using the Ψ_4 enrichment from X-FEM for Example 2. Here h denotes the length of elements along the x and y directions
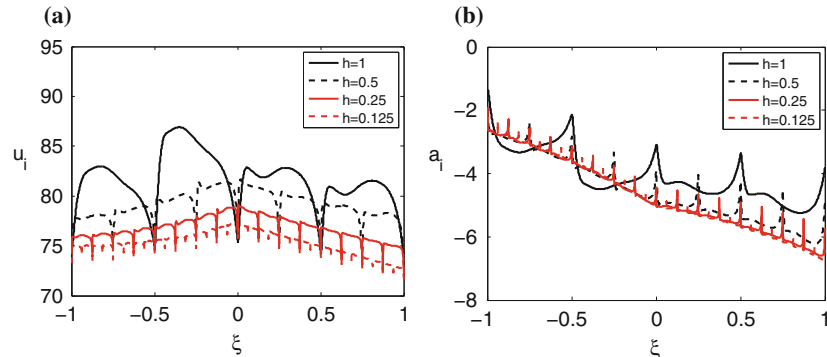
Fig. 19 Measure ε_E of the X-SFEM solution accuracy with a spectral PC approximation in the probability domain for increasing PC expansion p with (**a**) $h = 0.5$ and (**b**) $h = 0.25$ for Example 2
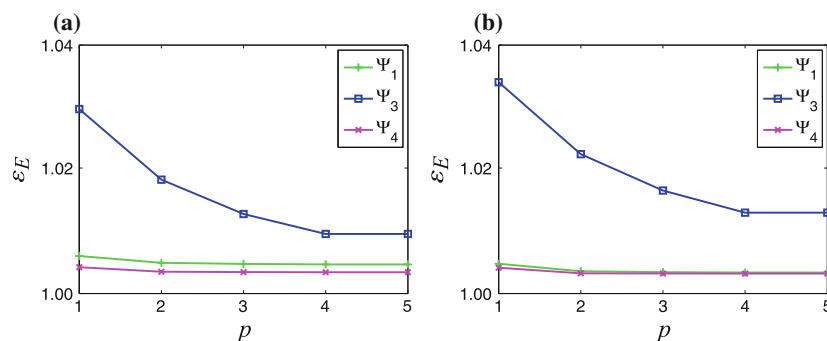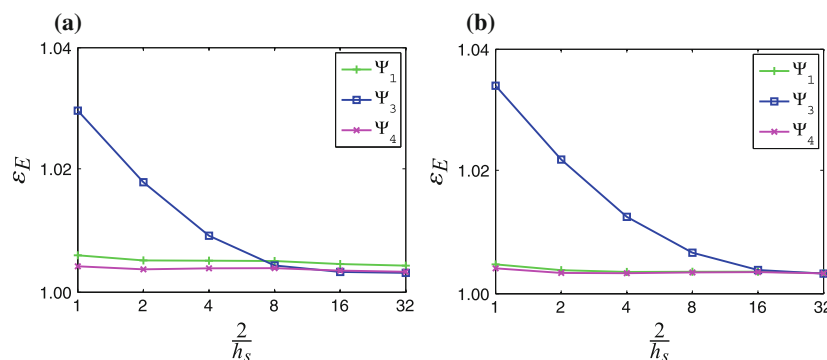

Fig. 20 Measure of the X-SFEM solution accuracy with a linear FE approximation in the probability domain for decreasing h_s with (**a**) $h = 0.5$ and (**b**) $h = 0.25$ for Example 2

of $\varepsilon_E = 1$ indicates that the energy norm of the X-SFEM approximation equals the MC based reference energy norm.

The measure, ε_E, is shown in Fig. 19 for increasing orders of the spectral approximation and spatial mesh sizes of $h = 0.5$ and $h = 0.25$. For the Ψ_1 and Ψ_4 enrichments, the measure is converged at low orders of the spectral PC approximation with a smaller converged value for the Ψ_4 enrichment. The measure using the Ψ_3 enrichment converges slower since the regular degrees of freedom are only piece-wise smooth for all spatial mesh sizes. Also, the measure for the Ψ_3 enrichment increases as the spatial mesh size is decreased. The spectral approximation becomes less accurate as the spatial mesh is refined because the variation of the enriched degrees of freedom becomes more localized, as shown in Fig. 17b. We note that an adaptive multi-element generalized PC approximation may improve the performance of the Ψ_3 enrichment [33].

The measure, ε_E, is shown in Fig. 20 for the linear FE approximation with decreasing stochastic mesh sizes for spatial mesh sizes of $h = 0.5$ and $h = 0.25$. The values of ε_E using the Ψ_1 and Ψ_4 enrichments show a similar behavior as with the spectral PC approximation. The values of ε_E using the Ψ_3 enrichment is improved using the linear FE approximation in the probability domain, and the converged measure has the same value as the Ψ_4 enrichment. An approach to improve the performance of the linear FE
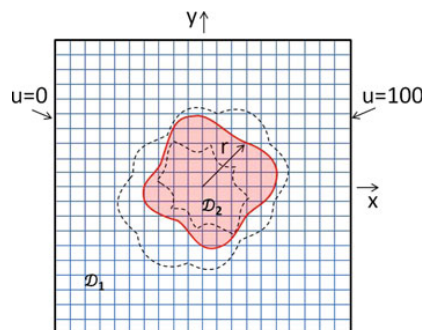

**Fig. 21** Problem description for Example 3, shown with a spatial mesh size of $h = 1$

approximation with the Ψ_3 enrichment is to use an aligned mesh for the probability domain, as discussed in Sect. 6.1. The partition constructed for piecewise integration over the probability domain can be used to define an aligned mesh for the probability domain, however this approach was not studied in this work.

6.3 Example 3

The third numerical example is the heat conduction problem shown in Fig. 21. This example is similar to Example 2,

Table 1 Energy norm of the X-SFEM solution and MC based reference energy norm for Example 3

		Ψ_1			Ψ_3			Ψ_4		
		h = 1	h = 0.5	h = 0.25	h = 1	h = 0.5	h = 0.25	h = 1	h = 0.5	h = 0.25
p	1	158.157	157.922	157.811	158.435	159.033	159.470	158.050	157.853	157.785
	2	158.019	157.787	157.659	157.875	158.310	158.670	157.891	157.652	157.587
	3	157.980	157.761	157.637	157.700	157.987	158.319	157.850	157.617	157.559
	4	157.962	157.750	157.630	157.590	157.811	158.095	157.834	157.602	157.549
	5	157.950	157.744	157.627	157.560	157.711	157.949	157.824	157.595	157.545
h_s	2	158.100	157.869	157.746	158.248	158.780	159.195	157.987	157.789	157.713
	1	157.994	157.774	157.651	157.755	158.078	158.416	157.863	157.641	157.586
	0.5	157.944	157.741	157.627	157.553	157.677	157.885	157.820	157.596	157.548
	0.25	157.927	157.726	157.618	157.507	157.545	157.618	157.806	157.583	157.540
ref				157.611			157.526			157.537
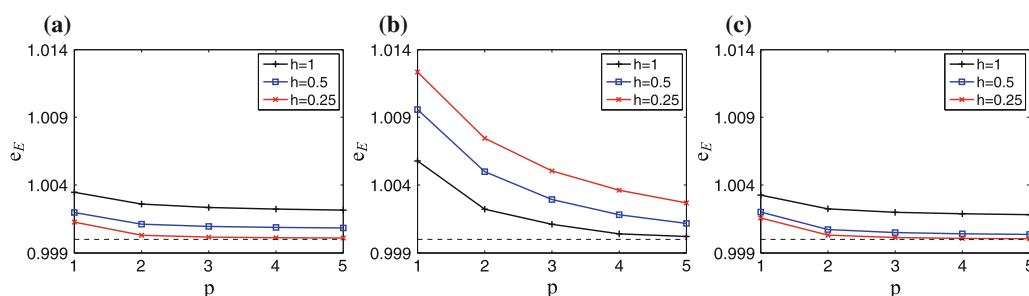
Fig. 22 Measure of the X-SFEM solution accuracy using the spectral PC stochastic approximation for the (**a**) Ψ_1, (**b**) Ψ_3, and (**c**) Ψ_4 enrichments for Example 3

except that the inclusion geometry depends on two random variables. The square domain $\mathcal{D} = (-10, 10) \times (-10, 10)$ $\subset \mathbb{R}^2$ has an inclusion with radius

$$r(\theta, \boldsymbol{\xi}) = \bar{r} + \sigma \sum_{k=1}^{2} \frac{1}{k} \xi_k \left[cos(k^2\theta) + sin(k^2\theta) \right], \qquad (31)$$

where $\bar{r}$ and σ are constants. Both ξ_1 and ξ_2 have uniform distributions $U(-1, 1)$ and are statistically independent. The angle θ is measured counterclockwise from the positive x-axis, and the constants $\bar{r} = 4$ and $\sigma = 1$ are used. The dashed lines in Fig. 21 define the maximum and minimum extent of the interface geometry, such that any realization of the material interface lies within the region between the dashed lines. The inclusion material is shaded for one sample of the possible geometry, $\boldsymbol{\xi} = (0.45, 0.80)$. The purpose of Example 3 is to investigate the convergence of the solution using the different enrichment functions and compare the spectral PC and linear FE stochastic approximations for the case of a two-dimensional probability domain.

As in Sect. 6.2, a measure for the accuracy of the X-SFEM approximation using the energy norm (30) is used

to investigate the convergence. The X-FEM reference solution for each enrichment function is computed using a MC simulation with 50,000 samples and a spatial mesh size of $h = 0.25$. The 95 % confidence intervals for the mean values of the reference solution for each enrichment function are ± 0.0040. The MC based reference energy norm and the X-SFEM solution energy norms for spatial mesh and stochastic refinement are shown in Table 1. Stochastic refinement for the spectral PC approximation refers to increasing the order of the approximation, p. For the linear FE approximation, stochastic refinement refers to decreasing the mesh size, h_s, in the probability domain. The measures, ε_E, are shown in Figs. 22 and 23 for the different enrichment functions with spatial mesh refinement and stochastic refinement. The dashed line represents a value of $e_E = 1$, which indicates when the energy norm of the X-SFEM approximation equals the MC based reference energy norm. The Ψ_1 and Ψ_4 enrichments show similar performance for the spectral PC and linear FE approximations. However, recall from Sect. 6.1 that the Ψ_1 enrichment is not an accurate deterministic approximation. The Ψ_4 enrichment with the spectral PC approximation at $p = 5$ approaches a similar measure as the
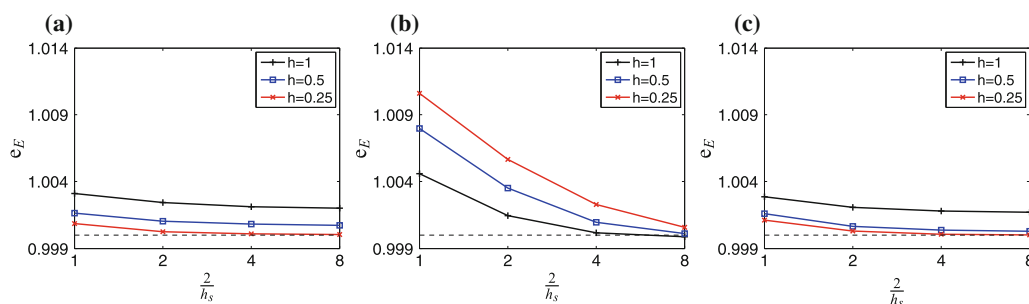
Fig. 23 Measure of the X-SFEM solution accuracy using the linear FE stochastic approximation for the (**a**) Ψ_1, (**b**) Ψ_3, and (**c**) Ψ_4 enrichments for Example 3

linear FE approximation at $h_s = 0.25$, but significantly fewer degrees of freedom are used. The spectral PC approximation with $p = 5$ uses 42 degrees of freedom per enriched node while the linear FE approximation with $h_s = 0.25$ uses 162 degrees of freedom per enriched node.

For the Ψ_3 enrichment, as the spatial mesh is refined the approximation in the probability domain must be simultaneously refined in order to maintain or reduce the measure ε_E. As can be seen in Figs. 22b and 23b, if only the spatial mesh is refined the measure increases. This effect is more pronounced for the spectral PC approximation than the linear FE approximation in the probability domain because the variation of the enriched degrees of freedom becomes more localized as the spatial mesh is refined. The convergence behavior with the Ψ_3 enrichment is opposite to what is observed for the other enrichment functions.

In contrast to the other enrichment strategies, it is interesting that the X-SFEM solution with the Ψ_3 enrichment converges to the correct solution using the coarsest spatial mesh with stochastic refinement. This suggests that the deterministic solution with the Ψ_3 enrichment converges faster as the spatial mesh is refined. In the present example, this characteristic allows a coarse spatial discretization to be used to achieve a level of accuracy, while the other enrichment strategies require a finer spatial discretization to achieve the same accuracy. However, for other problems this advantage of the Ψ_3 enrichment might be offset for its use in X-SFEM by the need for a fine resolution in the probability domain.

To summarize the behavior of the different enrichment strategies for the present example, the accuracy of the X-SFEM solution with the Ψ_1 and Ψ_4 enrichments is limited by the spatial resolution. In other words, the X-SFEM solution with these enrichments converges quickly with refinement of the stochastic approximation but requires a rather fine spatial mesh. In contrast, the accuracy of the X-SFEM solution with the Ψ_3 enrichment is limited by the resolution in the probability domain and converges quickly as the spatial mesh is refined. The main drawback of the Ψ_3 enrichment is the need to simultaneously increase the resolutions of the

spatial and stochastic approximations to maintain a particular level of accuracy.

7 Conclusions

The solution of partial differential equations with uncertainty in geometry was considered, and the Extended Stochastic Finite Element Method (X-SFEM) was studied for two-dimensional heat conduction of materials with uncertain inclusion geometry. A random field which characterizes the uncertain geometry is needed in X-SFEM, and the numerical solution can be used to predict statistical moments and probability distributions for the quantities of interest. The advantages of the X-SFEM approach include the avoidance of remeshing for realizations of the interface geometry and the ability to deal with complex inclusion geometries. For accurate integration in the probability domain, a partition approach was introduced using a triangulation which aligns with the regions where the integrand quantities are piecewise regular based on the random nodal level set values.

Four possible enrichment functions for X-SFEM were studied and compared. Two of the enrichment functions have global spatial support while the other two enrichments have local spatial support for a realization of the random parameters. For the two enrichments with local spatial support, one included the blending elements and the other did not. For the two enrichments with global spatial support, one simply used the absolute value of the level set function while the other was introduced in [22]. Here we considered a spectral polynomial chaos (PC) and a linear finite element (FE) approach for the approximation in the probability domain. Ideally for a spectral PC approximation in the probability domain, the degrees of freedom should be globally smooth. The smoothness of the degrees of freedom as functions of the random parameters depend on the chosen enrichment function and the spatial mesh size. The linear FE approximation was considered as an alternative since the degrees of freedom may be piecewise smooth functions of the random parameters. For the linear

FE approximation, there may be a strong dependency of the stochastic mesh on the accuracy of the approximation. For globally smooth functions, the spectral PC approximation is more efficient since fewer coefficients are needed. Of the four enrichment functions studied, only the enrichment introduced in [22] showed that in general the smoothness of the regular and enriched degrees of freedom as a function of the random parameters improves with spatial mesh refinement. The X-SFEM solution with the enrichment from [22], which has global spatial support, converges quickly with stochastic refinement but may require a fine spatial mesh to achieve global smoothness of the degrees of freedom in the probability domain. The X-SFEM solution with the enrichment which has local spatial support and includes the blending elements converges with a coarse spatial mesh but its accuracy is limited by the resolution in the probability domain. The drawback of using the enrichment with local spatial support is that simultaneous refinement of the spatial and stochastic approximations is needed to increase the accuracy. For the diffusive model problem presented in this paper, the X-SFEM solution using the spectral PC approximation in the probability domain with the enrichment function introduced in [22] showed the best performance in terms of accuracy and convergence properties. However, for other classes of problems, this conclusion has to be confirmed.

The numerical studies suggest that for diffusive problems, the spectral PC approximation is as accurate and more efficient than the linear FE approximation in the probability domain for an appropriate choice of enrichment function. For a successful enrichment function, the support of $\Psi(x, \xi)$ should include all possibly intersected elements plus the blending elements for a given value of ξ. In order to achieve global smoothness of the degrees of freedom as functions of the random parameters, the spatial support of $\Psi(x, \xi)$ should be global and should not introduce local oscillations which increase with spatial mesh refinement.

References

1. Asokan B, Zabaras N (2006) A stochastic variational multiscale method for diffusion in heterogeneous random media. J Comput Phys 218:654–676
2. Babuška I, Nobile F, Tempone R (2007) A stochastic collocation method for elliptic partial differential equations with random input data. SIAM J Numer Anal 43:1005–1034
3. Belytschko T, Moës N, Usui S, Parimi C (2001) Arbitrary discontinuities in finite elements. Int J Numer Meth Eng 50:993–1013
4. Belytschko T, Parimi C, Moës N, Sukumar N, Usui S (2003) Structured extended finite element methods for solids defined by implicit surfaces. Int J Numer Meth Eng 56:609–635
5. Canuto C, Kozubek T (2007) A fictitious domain approach to the numerical solution of pdes in stochastic domains. Numer Math 107:257–293
6. Deb M, Babuška I, Oden T (2001) Solution of stochastic partial differential equations using galerkin finite element techniques. Comput Methods Appl Mech Eng 190:6359–6372
7. Desceliers C, Ghanem R, Soize C (2006) Maximum likelihood estimation of stochastic chaos representations from experimental data. Int J Numer Meth Eng 66:978–1001
8. Fries T (2008) A corrected x-fem approximation without problems in blending elements. Int J Numer Meth Eng 75:503–532
9. Ghanem R (1999) Ingredients for a general purpose stochastic finite elements implementation. Comput Methods Appl Mech Eng 168:19–34
10. Ghanem R, Doostan A (2006) On the construction and analysis of stochastic models: Characterization and propagation of the errors associated with limited data. J Comput Phys 217:63–81
11. Ghanem R, Spanos P (1991) Stochastic finite elements: a spectral approach. Springer, New York
12. Hill R (1965) A self-consistent mechanics of composite materials. J Mech Phys Solids 13:213–222
13. Hou T, Wu X (1997) A multiscale finite element method for elliptic problems in composite materials and porous media. J Comput Phys 134:169–189
14. Ji H, Chopp D, Dolbow J (2002) A hybrid extended finite/level set method for modeling phase transformations. Int J Numer Meth Eng 54:1209–1233
15. Luo XY, Ni MJ, Ying A, Abdou M (2006) Application of the level set method for multi-phase flow computation in fusion engineering. Fusion Eng Des 81:1521–1526
16. Maître OL, Knio O, Najm H, Ghanem R (2004) Uncertainty propagation using wiener-haar expansions. J Comput Phys 197:28–57
17. Maître OL, Najm H, Ghanem R, Knio O (2004) Multi-resolution analysis of wiener-type uncertainty propagation schemes. J Comput Phys 197:502–531
18. Mathelin L, Hussaini M (2003) A stochastic collocation algorithm for uncertainty analysis. Tech. Rep. CR-2003-212153, NASA
19. Moës N, Dolbow J, Belytschko T (1999) A finite element method for crack growth without remeshing. Int J Numer Meth Eng 46:131–150
20. Moës N, Cloirec M, Cartraud P, Remacle JF (2003) A computational approach to handle complex microstructure geometries. Comput Methods Appl Mech Eng 192:3163–3177
21. Mori T, Tanaka K (1973) Average stress in matrix and average elastic energy of materials with misfitting inclusions. Acta Metall 21:571–574
22. Nouy A, Clément A (2010) Extended stochastic finite element method for the numerical simulation of heterogeneous materials with random material interfaces. Int J Numer Meth Eng 83:1312–1344
23. Nouy A, Schoefs F, Moës N (2007) X-sfem, a computational technique based on x-fem to deal with random shapes. Eur J Comput Mech 16:277–293
24. Nouy A, Clément A, Schoefs F, Moës N (2008) An extended stochastic finite element method for solving stochastic partial differential equations on random domains. Comput Methods Appl Mech Eng 197:4663–4682
25. Osher S, Sethian J (1988) Fronts propogating with curvature-dependent speed: Algorithms based on hamilton-jacobi formulations. J Comput Phys 79:12–49
26. Qian J, Cheng L, Osher S (2003) A level set-based eulerian approach for anisotropic wave propagation. Wave Motion 37:365–379

27. Sanchez-Palencia E (1980) Non-homogeneous media and vibration theory. Springer, New York
28. Sethian J (1999) Level set methods and fast marching methods: evolving interfaces in computational geometry, fluid mechanics, computer vision, and materials science. Cambridge University Press, Cambridge
29. Stefanou G, Nouy A, Clément A (2009) Identification of random shapes from images through polynomial chaos expansion of random level set functions. Int J Numer Meth Eng 79:127–155
30. Stolarska M, Chopp D, Moës N, Belytschko T (2001) Modelling crack growth by level sets in the extended finite element method. Int J Numer Meth Eng 51:943–960
31. Sukumar N, Chopp D, Moës N, Belytschko T (2001) Modeling holes and inclusions by level sets in the extended finite element method. Comput Methods Appl Mech Eng 190:6183–6200
32. Tan L, Zabaras N (2006) A level set simulation of dendritic solidification with combined features of front-tracking and fixed-domain methods. J Comput Phys 211:36–63
33. Wan X, Karniadakis G (2005) An adaptive multi-element generalized polynomial chaos method for stochastic differential equations. J Comput Phys 209:617–642
34. Wang M, Wang X, Guo D (2003) A level set method for structural topology optimization. Comput Methods Appl Mech Eng 192:227–246
35. Wiener N (1938) The homogenous chaos. Am J Math 60:897–936
36. Xiu D (2010) Numerical methods for stochastic computations: a spectral method approach. Princeton University Press, Princeton
37. Xiu D, Hesthaven J (2005) High-order collocation methods for differential equations with random inputs. SIAM J Sci Comput 27:1118–1139
38. Xiu D, Karniadakis G (2002) The wiener-askey polynomial chaos for stochastic differential equations. SIAM J Sci Comput 24:619–644
39. Xiu D, Tartakovsky D (2006) Numerical methods for differential equations in random domains. SIAM J Sci Comput 28:1167–1185
40. Zienkiewicz O, Taylor R (1989) The finite element method, 4th edn. McGraw-Hill, New York

Appendix B

Publication 2: A simple and efficient preconditioning scheme for heaviside enriched XFEM

ORIGINAL PAPER

A simple and efficient preconditioning scheme for heaviside enriched XFEM

**Christapher Lang · David Makhija ·
Alireza Doostan · Kurt Maute**

Abstract The extended finite element method (XFEM) is
an approach for solving problems with non-smooth solutions,
which arise from geometric features such as cracks, holes,
and material inclusions. In the XFEM, the approximate solu-
tion is locally enriched to capture the discontinuities with-
out requiring a mesh which conforms to the geometric fea-
tures. One drawback of the XFEM is that an ill-conditioned
system of equations results when the ratio of volumes on
either side of the interface in an element is small. Such inter-
face configurations are often unavoidable, in particular for
moving interface problems on fixed meshes. In general, the
ill-conditioning reduces the performance of iterative linear
solvers and impedes the convergence of solvers for nonlin-
ear problems. This paper studies the XFEM with a Heaviside
enrichment strategy for solving problems with stationary and
moving material interfaces. A generalized formulation of the
XFEM is combined with the level set method to implicitly
define the embedded interface geometry. In order to avoid
the ill-conditioning, a simple and efficient scheme based on
a geometric preconditioner and constraining degrees of free-
dom to zero for small intersections is proposed. The geomet-
ric preconditioner is computed from the nodal basis func-
tions, and therefore may be constructed prior to building
the system of equations. This feature and the low-cost of
constructing the preconditioning matrix makes it well suited
for nonlinear problems with fixed and moving interfaces.
It is shown by numerical examples that the proposed pre-
conditioning scheme performs well for discontinuous prob-
lems and C^0-continuous problems with both the stabilized
Lagrange and Nitsche methods for enforcing the continu-
ity constraint at the interface. Numerical examples are pre-
sented which compare the condition number and solution
error with and without the proposed preconditioning scheme.
The results suggest that the proposed preconditioning scheme
leads to condition numbers similar to that of a body-fitted
mesh using the traditional finite element method without loss
of solution accuracy.

Keywords Level set method · Extended finite element
method · Heaviside enrichment · Ill-condition ·
Preconditioner

1 Introduction

A standard tool for numerically solving problems defined by
a set of partial differential equations in many engineering dis-
ciplines is the finite element method (FEM). The solution to
problems which feature embedded interfaces, such as mate-
rial inclusions or voids, is non-smooth due to strong or weak
discontinuities which occur at the interface. A strong discon-
tinuity occurs when the solution is discontinuous across the
interface. A weak discontinuity occurs when the solution is
continuous but its spatial derivatives are discontinuous across
the interface. Conventionally, a finite element mesh is used
which conforms to the interface in order to approximate the
non-smooth solution. However, mesh generation may lead
to robustness issues and increase the computational cost for
problems with complex geometries or moving interfaces.

A widely used alternative for solving problems with
embedded interfaces is the extended finite element method
(XFEM) [21,32]. Local enrichment functions are added to

C. Lang
Structural Mechanics and Concepts Branch, NASA Langley
Research Center, Hampton, VA, USA

D. Makhija · A. Doostan (✉) · K. Maute
Aerospace Engineering Sciences, University of Colorado,
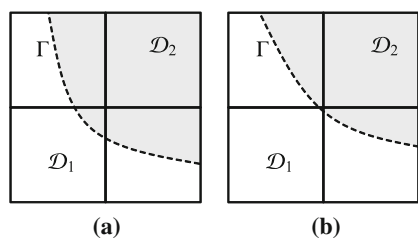Boulder, CO, USA
e-mail: doostan@colorado.edu

Fig. 1 Configuration of four quadrilateral elements which lead to a **a** well-conditioned and **b** ill-conditioned system. The lower left element in **b** has a small ratio of areas bisected by the interface

the standard FEM basis to represent the strong or weak solution discontinuities. The enrichment functions are constructed based on the position of the interface, which is implicitly defined by the level set method [23,28]. The XFEM does not require a mesh that conforms to the interface, which reduces the complexity of mesh construction. This feature is particularly advantageous for complex geometries as well as problems with moving or changing interface configurations [5,15,16,38]. However, the XFEM can lead to ill-conditioned systems when an intersected element(s) has a small ratio of areas bisected by the interface, as illustrated in Fig. 1. Ill-conditioned systems are a particular issue for nonlinear problems and iterative linear solvers [2,10].

The focus of this work is on a new scheme to mitigate the ill-conditioning issue in the XFEM. The goal is to obtain condition numbers using the XFEM that are of the same order of magnitude as standard FEM with a conforming mesh. Various approaches for dealing with this ill-conditioning have been proposed. A straight-forward approach is to construct a mesh that avoids small intersections with a uniform ratio of intersected element areas. Another approach is to move the nodes of intersected elements in order to avoid any intersected areas less than a specified amount [6]. However these approaches require adaptive meshing and mesh updating strategies which typically encounter efficiency and robustness issues for complex geometries and moving interfaces.

Other approaches involve modifications to the discretized system of equations such that careful mesh construction or moving the nodes is not necessary. Reusken [24] suggested constraining degrees of freedom associated with small supports to zero. This approach improves the condition number of the system by removing the constrained degrees of freedom. However, there is a trade-off between the accuracy of the solution and the ill-conditioning of the system which depends on the criterion for selecting the degrees of freedom to be constrained. The criterion must be carefully chosen in order to improve the condition number without decreasing the solution accuracy beyond an acceptable level. Preconditioning schemes have been proposed to improve the condition number of the system matrices to be solved. Sauerland and

Fries [27] study a Jacobi preconditioner, and preconditioners based on a Cholesky decomposition are introduced by Béchet et al. [2] and Menk and Bordas [20]. These alternative schemes are well suited for linear problems. However, the preconditioner can be built only after the discretized system of equations is assembled and must be reconstructed in each solution step for nonlinear problems, even when the interface geometry remains fixed.

A third class of methods modify the enrichment function to avoid the ill-conditioning issue. In [25], an approach for dealing with small intersections using b-spline finite elements is introduced. Interior and exterior b-splines are defined by the intersection size, and b-splines with a small intersection are denoted as exterior. The degrees of freedom associated with the exterior b-splines are expressed by a linear combination of the interior b-spline degrees of freedom. In [29,30], a modified XFEM approach is proposed which introduces an enrichment function associated with nodes defined by the intersection of the interface with element edges. The enrichment function is a scaled linear combination of Lagrangian shape functions of the integration elements. A stable XFEM is described in [1,27] which uses a local enrichment function constructed from a linear interpolant of the global enrichment function in the intersected elements. For problems with a weak discontinuity in the solution at the interface, the enrichment proposed in [22] is an example of a stable XFEM which leads to optimal convergence rates. We note that the stability of the enrichment in [1] relies on the use of a scaling matrix. This, therefore, indicates that the enrichment proposed in [22] also requires preconditioning to avoid ill-conditioning due to small element intersections.

Finally, Hansbo et al. [13] and Wadbro et al. [37] propose to augment the weak formulation to produce a well-conditioned system of equations independent of the interface position. The solution for each subdomain separated by the interface is considered, and a version of Nitsche's method is used to enforce the interface conditions. By adding additional volume terms to the weak formulation, the ill-conditioning is mitigated, but the solution error at the interface is increased. While this error decreases with mesh refinement, for a given mesh size this approach alters the solution of the discretized system. Also, new formulations are required for different governing equations since this approach alters the weak form.

In this work, a preconditioning scheme is proposed for a generalized Heaviside enrichment [18] that consists of a linear preconditioner and constraining degrees of freedom associated with small intersections. The Heaviside enriched XFEM formulation provides great flexibility in being applicable to a broad range of problem types with strong and weak discontinuities, though enforcing continuity at the interface is required for the latter. While a direct comparison of the proposed preconditioning scheme to other preconditioning methods is outside the scope of this paper,

some conceptual advantages for the proposed scheme are that no special considerations are necessary in the mesh generation, the enrichment function is not modified, and the weak formulation is unchanged. The construction of the preconditioner only requires the nodal basis functions and interface geometry; therefore, it may be constructed prior to building the discretized system of equations and is well suited for nonlinear problems. One drawback is that constraining degrees of freedom associated with small element intersections is necessary. However, the sensitivity of the solution error to the constrained degrees of freedom is reduced by the preconditioner.

Problems with static and prescribed moving interfaces are studied, and numerical examples show condition numbers for the XFEM using the proposed preconditioning scheme similar to the standard FEM. The proposed approach shows satisfactory performance for discontinuous problems and C^0-continuous problems with the stabilized Lagrange and Nitsche methods [8,14,31] for enforcing continuity at the interface.

The remainder of this paper is organized as follows: Sect. 2 defines the model problem which is used to describe the details of the proposed approach. Section 3 describes the XFEM framework, Heaviside enrichment strategy, and interface constraint formulation. Section 4 presents the proposed preconditioning scheme for handling small intersections. In Sect. 5, four numerical examples are presented to demonstrate the key features of the preconditioning scheme.

2 Model setup

Here we consider solving a stationary diffusion equation for a material with a single inclusion, as depicted in Fig. 2. The model problem is used for the description of the numerical method, and the first two numerical examples of Sect. 5 are concerned with diffusion problems at steady state. While we focus on this model problem for describing the details of the preconditioning scheme, the method is applicable to other problem types. In particular, the performance of the preconditioning scheme for a transient nonlinear fluid flow
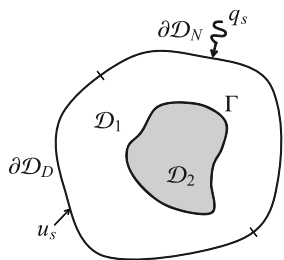

Fig. 2 Schematic of the model diffusion problem

problem with moving interfaces and a stationary interfacial debond problem are presented in the third and fourth numerical examples in Sect. 5.

The domain is comprised of two non-overlapping subdomains, such that $\mathcal{D} = \mathcal{D}_1 \cup \mathcal{D}_2$ and $\mathcal{D}_1 \cap \mathcal{D}_2 = \emptyset$. The interface between the two subdomains is defined as $\Gamma = \partial \mathcal{D}_1 \cap \partial \mathcal{D}_2$. A level set function $\phi(x)$ is constructed to define the location of Γ, such that

$$\begin{aligned} \phi(x) &< 0 \quad \text{if } x \in \mathcal{D}_1 \\ \phi(x) &> 0 \quad \text{if } x \in \mathcal{D}_2 \\ \phi(x) &= 0 \quad \text{if } x \in \Gamma. \end{aligned} \tag{1}$$

In this work, the signed distance function is used to define the level set function,

$$\phi(x) = \pm \min \|x - x_\Gamma\|, \tag{2}$$

where x_Γ is the interface location and $\| \cdot \|$ denotes the L^2-distance. Considering the particular case of diffusive heat conduction, the model problem consists of finding the temperature distribution, $u(x)$, such that

$$\begin{aligned} -\nabla \cdot (\kappa \nabla u_i) &= f \quad \text{in } \mathcal{D}_i \\ u_i &= u_s \quad \text{on } \partial \mathcal{D}_i \cap \partial \mathcal{D}_D \\ (\kappa \nabla u_i) \cdot n_i &= q_s \quad \text{on } \partial \mathcal{D}_i \cap \partial \mathcal{D}_N \end{aligned} \tag{3}$$

for $i = 1, 2$, where κ is the thermal conductivity tensor, f is a volumetric heat source, and u_i denotes the restriction of u to $\mathcal{D}_i$. The temperature distribution u_s is specified on a Dirichlet boundary $\partial \mathcal{D}_D$, and the heat flux q_s is specified on a Neumann boundary $\partial \mathcal{D}_N$. The outward unit normal to $\mathcal{D}_i$ is denoted by n_i. Additionally, continuity of the solution and flux across the interface Γ must be satisfied, such that

$$\begin{aligned} [\![u]\!] &= u_1 - u_2 = 0 \quad \text{on } \Gamma \\ k_1 \nabla u_1 \cdot n_1 + k_2 \nabla u_2 \cdot n_2 &= 0 \quad \text{on } \Gamma. \end{aligned} \tag{4}$$

Without loss of generality, the materials are assumed to be isotropic, i.e. $\kappa = k\,\mathbf{I}$. The conductivity k is defined as

$$k(x) = \begin{cases} k_1 & \text{if } x \in \mathcal{D}_1 \\ k_2 & \text{if } x \in \mathcal{D}_2 \end{cases} \tag{5}$$

with constants k_1 and k_2.

3 Extended finite element method

The traditional finite element method requires a mesh which conforms to the interface to implicitly satisfy the temperature

continuity and to capture the discontinuity in the temperature gradients at Γ. Alternatively, the extended finite element method is used to locally capture the non-smooth solution at the interface without using a mesh which conforms to Γ. In this section, we briefly outline the particular XFEM approach used here for solving the governing equation in (3).

The weak form of the governing equations is constructed by multiplying (3) by a set of admissible test functions and integrating over $\mathcal{D}$. The space $V = H^1(\mathcal{D})$ is the Hilbert space consisting of functions with square integrable first derivatives and $V_0 = \{v \in V : v|_{\partial \mathcal{D}_D} = 0\}$. Let $u \in V$ be the solution and $v \in V_0$ be an admissible test function. The weak form of the model problem is stated as: Find $u \in V$ such that $u = u_s$ on $\partial \mathcal{D}_D$ and

$$\int_{\mathcal{D}} (\boldsymbol{\kappa} \nabla u) \cdot \nabla v \, d\boldsymbol{x} - \int_{\mathcal{D}} f v \, d\boldsymbol{x} - \int_{\partial \mathcal{D}_N} q_s v \, ds = 0 \quad \forall v \in V_0. \tag{6}$$

Note that the continuity conditions were used to express the weak form in (6), such that $[\![u]\!] = 0$ at Γ and

$$\int_{\Gamma} (k_1 \nabla u_1 \cdot \boldsymbol{n}_1) v \, ds + \int_{\Gamma} (k_2 \nabla u_2 \cdot \boldsymbol{n}_2) v \, ds = 0. \tag{7}$$

In the XFEM, the traditional finite element approximation is augmented by an enrichment function and additional degrees of freedom. The choice of enrichment function affects the convergence and accuracy of the approximation, and various types of enrichment functions have been proposed. A C^0-continuous enrichment function [3,9,22,32] inherently satisfies the solution continuity at Γ and is applicable to problems with a weak discontinuity at the interface. A step enrichment function, such as a Heaviside or sign function, may be applied to problems with a strong or weak discontinuity in the solution at Γ. For the latter approach, the approximation of the weak form (6) needs to be augmented by constraints to satisfy the temperature continuity at the interface.

Here, we follow the work of Terada et al. [33] and Tran et al. [35] and adopt a generalized version of the Heaviside enrichment strategy of Hansbo and Hansbo [12]. As recently shown by Makhija and Maute [18], this implementation of the XFEM provides great flexibility in discretizing a broad range of partial differential equations with multiple phases for any choice of nodal basis functions. However, the Heaviside enrichment can lead to a system of equations that is ill-conditioned [10,20]. The remainder of this section describes the details of the generalized Heaviside enrichment strategy and the interface constraint formulation.

3.1 Generalized heaviside enrichment

Consider a finite element mesh, $\mathcal{T}_h$, for $\mathcal{D}$ consisting of elements with edges that do not necessarily coincide with Γ. A Heaviside enrichment function is implemented in the XFEM formulation such that the approximation of $u(\boldsymbol{x})$, denoted by $u^h(\boldsymbol{x})$, for two phases is defined as

$$u^h(\boldsymbol{x}) = \sum_{m=1}^{M} \left(H(-\phi(\boldsymbol{x})) \sum_{i \in I} N_i(\boldsymbol{x}) u_{i,m}^{(1)} \right.$$
$$\left. + H(\phi(\boldsymbol{x})) \sum_{i \in I} N_i(\boldsymbol{x}) u_{i,m}^{(2)} \right), \tag{8}$$

where I is the set of all nodes in $\mathcal{T}_h$, $N_i(\boldsymbol{x})$ is the nodal basis function, M is the maximum number of enrichment levels, $u_{i,m}^{(p)}$ is the degree of freedom at node i for phase $p \in \{1, 2\}$, and H is the Heaviside function,

$$H(z) = \begin{cases} 1 & z > 0 \\ 0 & z \le 0 \end{cases}. \tag{9}$$

In this formulation, a single basis function, N_i, is used for each node. Additional nodal degrees of freedom are added for each phase and enrichment level.

The need for multiple enrichment levels is illustrated by the example configurations shown in Fig. 3. For the multiple

Fig. 3 Example configurations requiring multiple enrichment levels at the center node for **a** multiple inclusions and **b** a single inclusion

inclusions in Fig. 3a, four quadrilateral elements share a central node that is connected to the phase 1 domain and three inclusions belonging to phase 2. The center node requires one degree of freedom for the phase 1 solution and three degrees of freedom in order to individually interpolate the solutions in the three inclusions. The work in [35] addresses configurations with multiple inclusions by assigning multiple level set functions and adding enriched degrees of freedom for each. However, additional enrichment levels may also be required for a single inclusion. For the configuration in Fig. 3b, the center node requires one degree of freedom for the phase 1 solution and two degrees of freedom for the the disconnected regions belonging to phase 2.

By generalizing the Heaviside enrichment to multiple levels, accurate solutions can be determined for neighboring intersected elements and elements intersected more than once using a single level set function. The number of enrichment levels required at a single node is determined by the number of disconnected regions of the same phase included in the support of the nodal basis function. Note that while a maximum number of enrichment levels is specified in (8), some enrichment levels are not used. The degrees of freedom corresponding to the unused enrichment levels are removed from the system of equations. Further details of this generalized enrichment strategy is provided in [18].

3.2 Interface constraint formulation

While the continuity of the solution at the interface (4) is inherently satisfied using a C^0-continuous enrichment function, the Heaviside enrichment requires an additional constraint to enforce the continuity. Common approaches for enforcing an interface constraint in the XFEM include the stabilized Lagrange multiplier and Nitsche methods [8,14,31]. Here, both constraint formulations are used for enforcing continuity at the interface for the model problem.

The weak form using the stabilized Lagrange multiplier method is stated as: Find $(u, \lambda) \in (V \times W)$ such that $u = u_s$ on $\partial \mathcal{D}_D$ and

$$
\int_{\mathcal{D}} (\kappa \nabla u) \cdot \nabla v d\mathbf{x} - \int_{\mathcal{D}} f v d\mathbf{x} - \int_{\partial \mathcal{D}_N} q_s v ds
$$
$$
- \int_{\Gamma} [\![v]\!] \lambda d\Gamma + \int_{\Gamma} \mu (\lambda - \{k \nabla u \cdot \mathbf{n}\}) d\Gamma
$$
$$
+ \gamma_S \int_{\Gamma} \mu [\![u]\!] d\Gamma = 0 \quad \forall (v, \mu) \in (V_0 \times W), \tag{10}
$$

where λ is the Lagrange multiplier, $W = H^{-1/2}(\Gamma)$ is the space for the Lagrange multiplier, μ is the associated test function, γ_S is a constraint factor, and $\{\cdot\} = \frac{1}{2}(\cdot)_1 + \frac{1}{2}(\cdot)_2$ denotes the mean operator on the interface.
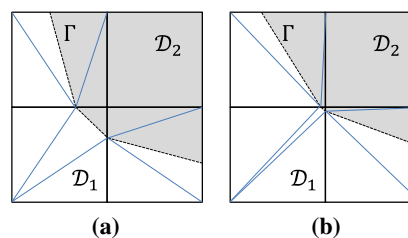

Fig. 4 Triangulated partition of a four element configuration leading to a **a** well-conditioned and **b** ill-conditioned system

For Nitsche's method, the weak form is stated as: Find $u \in V$ such that $u = u_s$ on $\partial \mathcal{D}_D$ and

$$
\int_{\mathcal{D}} (\kappa \nabla u) \cdot \nabla v d\mathbf{x} - \int_{\mathcal{D}} f v d\mathbf{x} - \int_{\partial \mathcal{D}_N} q_s v ds
$$
$$
- \int_{\Gamma} [\![v]\!] \{k \nabla u \cdot \mathbf{n}\} d\Gamma - \int_{\Gamma} \{k \nabla v \cdot \mathbf{n}\} [\![u]\!] d\Gamma
$$
$$
+ \gamma_N \int_{\Gamma} [\![v]\!] [\![u]\!] d\Gamma = 0 \quad \forall v \in V_0, \tag{11}
$$

where γ_N is a constraint factor for Nitsche's method.

3.3 Discretization

The level set function is discretized by the finite element mesh, such that

$$
\phi(\mathbf{x}) = \sum_{i \in I} N_i(\mathbf{x}) \phi_i, \tag{12}
$$

where ϕ_i is the value of the level set function at node i. In this work, the interface position is prescribed by determining ϕ_i at each node using the signed distance function (2). Since $\phi(\mathbf{x})$ is discretized by the finite element mesh, the resolution of the inclusion geometry is dependent on $\mathcal{T}_h$ and improves with mesh refinement. The intersection of Γ with an element edge is identified by a sign change in ϕ_i for a pair of edge nodes. The intersection of Γ directly through a node or an element edge is avoided by enforcing $\phi_i \neq 0$. For any node i where $|\phi_i| < \phi_{min}$, the nodal level set value is changed to $\phi_i = -\phi_{min}$. For the examples in this work, $\phi_{min} = 2 \times 10^{-9} \sqrt{\frac{A^e}{\pi}}$ where A^e is the geometric element area.

Accurate integration over intersected elements is performed by partitioning the element domain, $\mathcal{D}^e$, for piecewise integration. In particular, we partition $\mathcal{D}^e$ using a triangulation aligned with Γ. An illustration of the triangulation is shown in Fig. 4 for two configurations of the interface using four elements.

We consider a uniform mesh for $\mathcal{T}_h$ constructed with quadrilateral elements. Bilinear nodal basis functions are used for $N_i(\mathbf{x})$, and elemental Lagrange multipliers are intro-

duced for the stabilized Lagrange multiplier method. We choose a constant or linear approximation of λ along the interface Γ in an intersected element. This approximation for λ is chosen for convenience, as it allows condensing the Lagrange multiplier degree of freedom at an elemental level; other approximations of the Lagrange multiplier can be used in the formulation (10).

The system of equations is constructed by substituting the approximation (8) into the weak form (10) or (11). Following the Bubnov–Galerkin method, the integration in (10) or (11) is performed over each element and assembled to construct the system of equations. The discretized system of equations is given by

$$K\hat{u} = f, \tag{13}$$

where $\hat{u}$ is the solution vector collecting the degrees of freedom $u_{i,m}^{(1)}$ and $u_{i,m}^{(2)}$, and K and f are the conduction matrix and load vector, respectively. For the case in which (13) may be linear or nonlinear, the system residual and Jacobian may be used with the Newton–Raphson method to solve the system. For the remainder of this paper, we refer to the system residual, R, and Jacobian, J, defined as

$$R = K\hat{u} - f \tag{14}$$

$$J_{ij} = \frac{\partial R_i}{\partial u_j}. \tag{15}$$

Note that for a linear system of equations, $J = K$ and only one iteration in the Newton–Raphson method is required.

4 Preconditioning scheme

We propose a preconditioning scheme in order to transform the system of equations into a form that is well-conditioned and suitable for solving iteratively. For the configuration shown in Fig. 4b, the lower left element has a small ratio of intersected areas. The region of influence for the degree of freedom at the lower left node interpolating phase 2 approaches zero as the interface approaches the center node. The region of influence for a degree of freedom is the intersection of the nodal basis function support with the physical subdomain $\mathcal{D}_i$. Our aim is to mitigate the sensitivity of the residual to the dissimilar regions of influence for the degrees of freedom. The proposed approach consists of transforming the degrees of freedom by a preconditioning matrix and constraining degrees of freedom associated with small intersections to zero. The small intersections are ignored for the constrained degrees of freedom, which are removed from the equations when solving the system. When constraining degrees of freedom only without using the preconditioning matrix [24], the solution accuracy decreases as the condition

number is reduced. The proposed approach solves the problem in a transformed space and does not change the solution to the discrete problem. We will show in Sect. 5 that the preconditioning scheme maintains an approximately constant condition number without loss of solution accuracy.

A geometric preconditioner T is introduced, such that the solution in the physical space, $\hat{u}$, is obtained by

$$\hat{u} = T\tilde{u}, \tag{16}$$

where $\tilde{u}$ is the solution in the transformed space. The residual and Jacobian of the system in the transformed space are defined as

$$\tilde{R} = T^T R$$
$$\tilde{J} = T^T J T. \tag{17}$$

Note, the residual R and the Jacobian J are constructed in a standard fashion using the XFEM. For problems with dynamically evolving interfaces, such as phase change and multi-phase flow problems [4,5,38], the discretized level set field contributes degrees of freedom to the solution vectors $\hat{u}$ and $\tilde{u}$. In this case, the Jacobian $\tilde{J}$ contains additional terms. We omit a detailed discussion of this class of problems and focus on problems with static or prescribed interface geometries.

The purpose of the geometric preconditioner is to balance the influence for degrees of freedom as the intersected areas approach zero. There are two issues associated with the intersected areas approaching zero. First, the partitioned element integration, and therefore the diagonal entry of the element matrix, approaches zero because the area of integration is small. Second, the influence of a degree of freedom on the residual will vanish as the region of influence approaches zero.

Here, we construct a diagonal preconditioning matrix for T from the nodal basis functions and their support in order to transform the degrees of freedom. The proposed approach accommodates other choices for T, both diagonal and non-diagonal. However, diagonal scaling is more computationally efficient in terms of memory and matrix operations. The preconditioning matrix T is constructed by integrating the nodal basis functions (T_N) or derivatives (T_B) over the nodal support. The diagonal components of the T_N preconditioning matrix are defined as

$$T_{i,m}^{(p)} = \left(\max_{e \in E_i} \frac{\int_{\mathcal{D}_{p,m}^e} N_i(\boldsymbol{x}) d\boldsymbol{x}}{\int_{\mathcal{D}^e} N_i(\boldsymbol{x}) d\boldsymbol{x}} \right)^{-\frac{1}{2}}, \tag{18}$$

where $T_{i,m}^{(p)}$ corresponds to the degree of freedom $u_{i,m}^{(p)}$ at node i, and E_i is the set of elements connected to node i. Here, $\mathcal{D}_{p,m}^e$ denotes the element domain which belongs to phase p

Comput Mech

for enrichment level m. The diagonal components of the T_B preconditioning matrix are defined as

$$T_{i,m}^{(p)} = \left(\max_{e \in E_i} \frac{\int_{\mathcal{D}_{p,m}^e} \nabla N_i(\boldsymbol{x}) \cdot \nabla N_i(\boldsymbol{x}) dx}{\int_{\mathcal{D}^e} \nabla N_i(\boldsymbol{x}) \cdot \nabla N_i(\boldsymbol{x}) dx} \right)^{-\frac{1}{2}}. \qquad (19)$$

In practice, the components $T_{i,m}^{(p)}$ are only computed at nodes connected to an intersected element. If all elements in E_i are non-intersected, then the degrees of freedom at node i are not transformed and $T_{i,m}^{(p)} = 1$.

The T_N and T_B geometric preconditioners both lead to scaling terms that increase as the region of influence for degrees of freedom approaches zero. The region of influence is measured by $\max_{e \in E_i} \int_{\mathcal{D}_p^e} N_i(\boldsymbol{x}) dx$ and $\max_{e \in E_i} \int_{\mathcal{D}_p^e} \nabla N_i(\boldsymbol{x}) \cdot \nabla N_i(\boldsymbol{x}) dx$ in (18) and (19), respectively. For a given problem, the choice of the preconditioner type can be determined by the dominating operator in the partial differential equation. Based on the construction of the system of equations, the T_B preconditioning matrix is more appropriate for diffusion dominated problems, while T_N is appropriate for convection or reaction dominated problems.

The preconditioner T improves the condition number by balancing the influence of the degrees of freedom. However, as the preconditioner is constructed using the nodal basis functions, the scaling terms in T do not approach ∞ at the same rate as the region of influence approaches zero. Therefore, an ill-conditioned system of equations may still result when the ratio of intersected areas approaches zero. In addition to the preconditioner, we propose to constrain degrees of freedom to zero with small regions of influence. The criterion for selecting the degrees of freedom to be constrained to zero is defined as

$$T_{i,m}^{(p)} > T_{tol}, \qquad (20)$$

where T_{tol} is a specified tolerance. It is shown in Sect. 5 that there is a wide range for the choice of T_{tol} which does not impact the numerical error and condition number. Constraining degrees of freedom to zero is needed when $T_{i,m}^{(p)} \gg 1$. The numerical studies in Sect. 5 suggest values for T_{tol} between 10^4 and 10^8.

A summary of applying the proposed preconditioning scheme to a nonlinear problem solved by the Newton–Raphson method is outlined below:

1. Construct $\mathcal{T}_h$ and ϕ.
2. Construct T using (18) or (19) and mark degrees of freedom to be constrained by (20).
3. Obtain transformed initial guess by the inverse operation of (16).
4. Solve iteratively the problem $\tilde{\boldsymbol{R}} = 0$ for $\tilde{\boldsymbol{u}}$ as follows:

   (a) Reconstruct T and update degrees of freedom to be constrained.
   (b) Obtain current solution by (16).
   (c) Construct $\boldsymbol{R}$ and $\boldsymbol{J}$.
   (d) Obtain $\tilde{\boldsymbol{R}}$ and $\tilde{\boldsymbol{J}}$ by (17).
   (e) Solve transformed system for $\Delta \tilde{\boldsymbol{u}}$.
   (f) Update solution and check for convergence.

5. Obtain final solution, $\hat{\boldsymbol{u}}$, by (16)

As shown in the implementation outline, T is constructed prior to computing the residual and Jacobian. If the interface geometry is prescribed and independent of the solution, then the level set field and hence T do not change in the Newton iterations. In this case, step 4(a) is not necessary.

5 Numerical examples

In this section, the performance of the preconditioning scheme is studied for four problems. The first example illustrates the basic concept of the preconditioning scheme when solving a diffusion problem for a two-material bar. The second example is a diffusion problem with a circular material inclusion. For these examples, the accuracy of the solution as well as the condition number of the systems are examined with and without the proposed preconditioning scheme. The third example is a transient flow problem with a moving rigid obstacle, modeled by the incompressible Navier–Stokes equations. This example demonstrates the applicability of the proposed scheme to nonlinear transient problems with moving interfaces. Finally, the fourth example studies the solution accuracy and system condition number for an interfacial debond problem with and without the proposed preconditioning scheme. While the examples in this paper consider 2D problems, the extension of the proposed preconditioning scheme to 3D problems is straight-forward as discussed in [36].

5.1 Example 1: two-material bar diffusion

We illustrate the basic concept of the preconditioning scheme for a simple example with an analytical solution. We consider solving the heat conduction model for the two-material bar shown in Fig. 5. The length of the bar is L, and temperatures u_1 and u_2 are specified at $x = 0$ and $x = L$, respectively. The material conductivity is $k_1 = 1$ in $\mathcal{D}_1$ and $k_2 = 2$ in $\mathcal{D}_2$. The position of the vertical interface is measured from the left end and specified by r. The problem is solved using quadrilateral elements. While the exact solution can be captured using one element, we discretize the bar with five elements in order to vary the position of the interface across one element. Note that while this example is useful for explaining
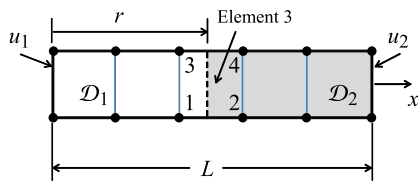
Fig. 5 Problem description for example 1

the concept and demonstrating the reduced condition number, it is not well suited to illustrate a change in the accuracy of the solution due to an ill-conditioned system. Without preconditioning, an ill-conditioned system will occur when the interface is nearly aligned with an element edge. In the intersected element, a ratio of the area of the phase 1 and phase 2 regions with a value less than 10^{-13} results in a condition number greater than 10^{14}. With the level set shift described in Sect. 3.3 and a converged mesh, the XFEM solution matches the analytical solution for this example.

The interface position is varied from $r/L = 0.3$ to $r/L = 0.7$ in steps of $\Delta r/L = 0.002$. Element 3 is intersected for $0.4 < r/L < 0.6$. As r/L approaches 0.4 and 0.6, the ratio of intersected areas in element 3 becomes small. The preconditioning scheme using the $\boldsymbol{T}_B$ matrix and $T_{tol} = 10^4$ is selected for the example bar problem. The stabilized Lagrange multiplier method with $\gamma_S = k_1 + k_2$ and an element-wise constant approximation for λ is used for enforcing continuity at the interface.

There are four degrees of freedom for element 3 at nodes 1 to 4 which have small regions of influence as the interface position is varied. Since the problem is one-dimensional, we only consider nodes 1 and 2, and focus on the degrees of freedom $u_{1,1}^{(2)}$ and $u_{2,1}^{(1)}$. The degree of freedom $u_{1,1}^{(2)}$ is used for interpolating the phase 2 solution in element 3, and it has a small region of influence when $r/L \approx 0.6$. The degree of freedom $u_{2,1}^{(1)}$ is used for interpolating the phase 1 solution in element 3, and it has a small region of influence when $r/L \approx 0.4$.

The $\boldsymbol{T}_B$ values corresponding to these degrees of freedom are shown in Fig. 6a as the interface location varies. The $T_{1,1}^{(2)}$ and $T_{2,1}^{(1)}$ values increase as the ratio of intersected areas in element 3 decrease. The diagonal components of $\tilde{\boldsymbol{J}}$ corresponding to $u_{1,1}^{(2)}$ and $u_{2,1}^{(1)}$ without preconditioning ($\boldsymbol{T} = \boldsymbol{I}$) and with the preconditioner $\boldsymbol{T}_B$ are shown in Fig. 6b. The diagonal components of $\tilde{\boldsymbol{J}}$ with $\boldsymbol{T} = \boldsymbol{T}_B$ do not reduce to zero as the ratio of intersected areas approach zero. The jumps in $\tilde{J}_{ii}$ at $r/L = 0.4$ and $r/L = 0.6$ result from the stabilized Lagrange method for enforcing continuity at the interface.

The condition number of $\tilde{\boldsymbol{J}}$ is shown as a function of the interface position in Fig. 7. The condition number was determined without and with the preconditioning scheme, denoted by $\boldsymbol{T} = \boldsymbol{I}$ and $\boldsymbol{T} = \boldsymbol{T}_B$, respectively. No degrees of free-
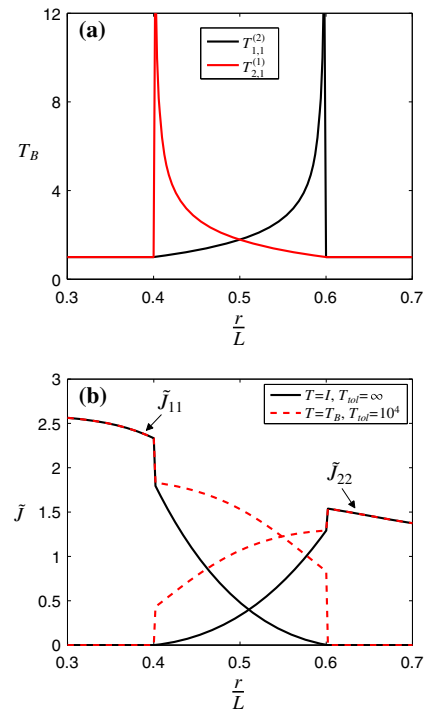
Fig. 6 The diagonal components of **a** $\boldsymbol{T}_B$ and **b** $\tilde{\boldsymbol{J}}$ corresponding to the degrees of freedom $u_{1,1}^{(2)}$ and $u_{2,1}^{(1)}$. Here $\tilde{J}_{11}$ and $\tilde{J}_{22}$ correspond to $u_{1,1}^{(2)}$ and $u_{2,1}^{(1)}$, respectively

dom were constrained for $T_{tol} = \infty$. The condition number is improved for $\boldsymbol{T} = \boldsymbol{T}_B$ and $T_{tol} = \infty$, but is still large near $r/L = 0.4$ and $r/L = 0.6$. By constraining degrees of freedom according to T_{tol} in (20), the condition number at $r/L = 0.4$ and $r/L = 0.6$ is significantly reduced. The physical and transformed solutions for the degrees of freedom $u_{1,1}^{(2)}$ and $u_{2,1}^{(1)}$ are shown in Fig. 8. The physical degrees of freedom jump to zero when element 3 is not intersected. The influence of the preconditioning for $u_{1,1}^{(2)}$ and $u_{2,1}^{(1)}$ occurs when element 3 is intersected. The projected degrees of freedom vary to zero as the ratio of intersected areas approach zero.

5.2 Example 2: circular inclusion diffusion

The second numerical example is the heat transfer problem shown in Fig. 9. The model problem (3) is solved for a square domain $\mathcal{D} = (-10, 10) \times (-10, 10)$ with a centered circular inclusion of radius r. The radius is varied from $r = 3$ to $r = 7$ in steps of $\Delta r = 0.02$. Material 1 has a conductivity $k_1 = 2$ in $\mathcal{D}_1$, and material 2 has a conductivity $k_2 = 2 \times 10^3$ in $\mathcal{D}_2$. The temperature is specified as $u = 0$ on the left boundary and $u = 100$ on the right boundary. The top and bottom edges are adiabatic. The computational domain is discretized
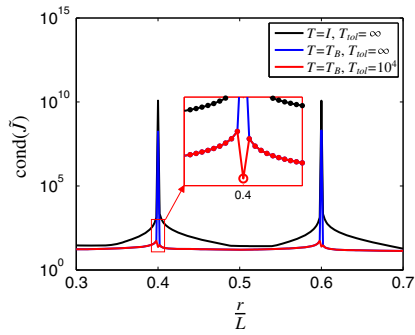
Fig. 7 Condition number as a function of the interface position for the two-material bar. In the inset figure, $\Delta r/L = 2 \times 10^{-5}$ and the open circle marks the r/L value for which degrees of freedom were constrained
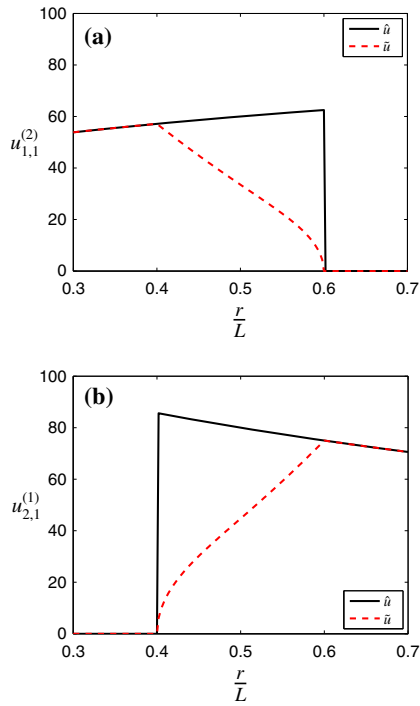

Fig. 8 The physical ($\hat{u}$) and projected ($\tilde{u}$) solutions for the degrees of freedom **a** $u_{1,1}^{(2)}$ and **b** $u_{2,1}^{(1)}$

with a uniform 20×20 mesh resulting in approximately 470 unknowns. The exact number of degrees of freedom depends on the intersection configuration. The two methods of enforcing the solution continuity at the interface (10) and (11) are considered with $\gamma_S = k_1 + k_2$ and $\gamma_N = 10^{-3}(k_1 + k_2)$. An element-wise constant approximation for λ is used for the stabilized Lagrange multiplier method.

The condition number of the system of equations depends on the configuration of the intersections and the ratio of con-
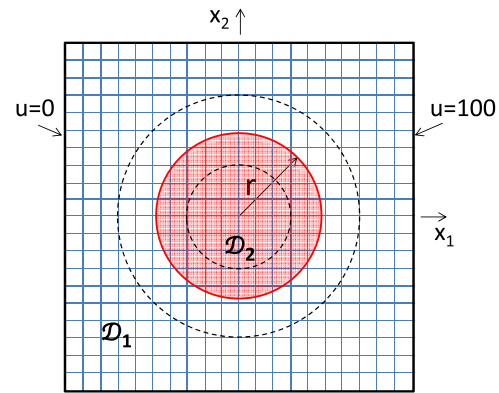
Fig. 9 Problem description for example 2
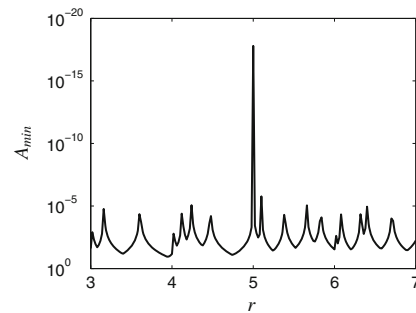
Fig. 10 Minimum element area ratio, A_{min}, for example 2

ductivities. A high ratio of conductivities, also considered in [7,19], is used here to highlight the ill-conditioning issue for this simple example problem. The ratio of intersected areas is examined for the variation of the radius by determining the minimum element area ratio, defined as

$$A_{min} = \min_{e \in \mathcal{T}_h^c} \frac{\mathcal{D}_1^e}{\mathcal{D}_2^e},\qquad(21)$$

where $\mathcal{T}_h^c$ is the set of intersected elements. The variation of A_{min} with r is shown in Fig. 10. Note the vertical axis is reversed, such that small intersections are indicated by the peaks. The minimum area ratios of order 10^{-5} and 10^{-18} which occur for the variation of r lead to a high condition number of the system.

Three studies were performed for this example. The first study shows the influence of T_{tol} in (20) on the condition number and solution accuracy. The second study is a comparison of the condition number using a body-fitted mesh, XFEM with a Jacobi preconditioner, and XFEM with the proposed preconditioning scheme. Finally, we study the influence of the preconditioning scheme on the performance of an iterative solver.

To study the influence of T_{tol} on the condition number and solution accuracy, the T_B preconditioning matrix and the

stabilized Lagrange multiplier method are used. The value of T_{tol} is varied from $T_{tol} = 10$ to $T_{tol} = 10^8$. The maximum condition number of $\tilde{J}$ and solution error is computed for each value of T_{tol} by considering all values of r. The maximum condition number, cond_{max}, is defined by

$$\text{cond}_{max} = \max_r \ \text{cond}(\tilde{J}). \tag{22}$$

The accuracy of the XFEM solution is measured by integrating the L_2 relative error, such that the total error for each value of T_{tol} is defined by

$$e_{total} = \int_3^7 \frac{\|u^h(r) - u_{ref}(r)\|_2}{\|u_{ref}(r)\|_2} dr, \tag{23}$$

where $u_{ref}(r)$ is a reference solution for radius r obtained using a body-fitted finite element mesh with an element size of $h \approx 0.05$ leading to approximately 154,000 degrees of freedom.

The influence of T_{tol} on the condition number and solution error is shown in Fig. 11 with and without the preconditioning matrix. For $T = I$, the preconditioning matrix is only used for the criterion on constraining degrees of freedom in (20) and not applied when solving the system of equations. In both cases, $T = I$ and $T = T_B$, the solution error decreases as T_{tol} is increased. For $T = I$, this corresponds to a drastic increase in the condition number while the condition number
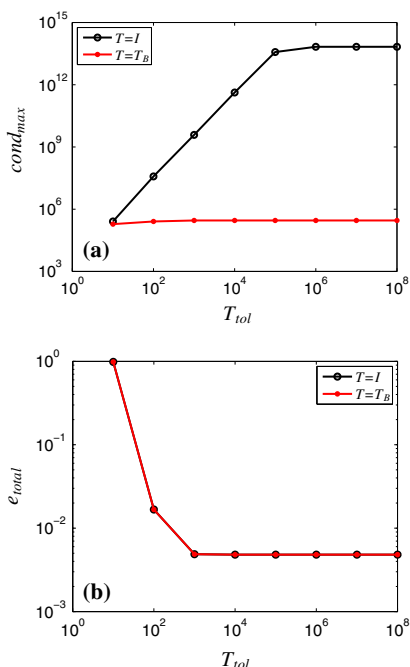

Fig. 11 Influence of T_{tol} on the **a** maximum condition number and **b** approximation error computed from (22)–(23) for example 2
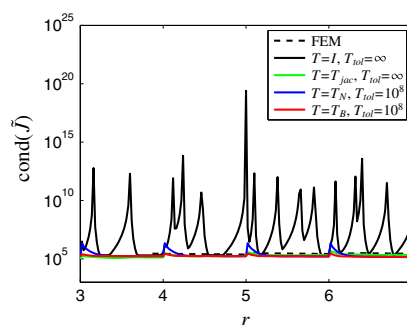

Fig. 12 Comparison of the condition number for a varying inclusion radius using the stabilized Lagrange method for example 2
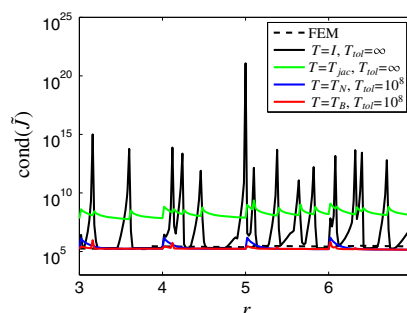

Fig. 13 Comparison of the condition number for a varying inclusion radius using Nitsche's method for example 2

remains approximately constant for $T = T_B$. Note that the same number of degrees of freedom were constrained to zero for T_{tol} values of 10^6, 10^7, and 10^8.

The second study compares the condition number for various choices of T. The condition number of $\tilde{J}$ is computed for the variation of r using XFEM with the stabilized Lagrange and Nitsche methods. The condition number of $\tilde{J}$ using a body-fitted mesh with an element size of $h \approx 0.5$ and $T = I$ was also computed. A Jacobi preconditioner is implemented by defining

$$T_{jac} = \text{diag}(J)^{-\frac{1}{2}}. \tag{24}$$

Note that T_{jac} is a solver preconditioner which operates on the Jacobian after it is assembled. In contrast to the proposed preconditioner, T_{jac} does not utilize geometric information of the intersection configuration. Finally, the condition number of $\tilde{J}$ is computed using the T_N and T_B preconditioning matrices with $T_{tol} = 10^8$. A comparison of the condition numbers for the variation of r is shown in Figs. 12 and 13. No degrees of freedom were constrained for $T = I$ and $T = T_{jac}$, which corresponds to $T_{tol} = \infty$. For $T = I$, the condition number using XFEM varies with the size of the inclusion up to an order of 10^{20}. The r values of the high

condition numbers correspond to the small intersections seen in Fig. 10. For $T = T_{jac}$, the condition number is comparable to that of the body-fitted FEM system for the stabilized Lagrange method (Fig. 12) but not Nitsche's method (Fig. 13). This suggests that the condition number is influenced by the off-diagonal terms in J for Nitsche's method. However, for $T = T_N$ and $T = T_B$, the XFEM condition number is comparable to the body-fitted FEM system for both stabilized Lagrange and Nitsche methods for all interface positions.

The third study examines the influence of the preconditioning scheme on the performance of an iterative solver by solving the system of equations using the generalized minimal residual method (GMRES) [26]. A solver preconditioner, M, was implemented to compare with the performance of the preconditioning scheme. A Jacobi, M_{jac}, and incomplete LU with zero fill-in, M_{ilu}, were chosen as the solver preconditioners. The number of iterations, n_{itr}, required to satisfy $\|f - K\hat{u}\|_2 < 10^{-6}$ was determined using the physical solution. The solution error was determined as

$$e_{L_2} = \|u^h - u_{ref}\|_2, \tag{25}$$

where u_{ref} is a reference solution computed on the 20×20 mesh using a direct solver with $T = I$. Note, the body-fitted FEM reference solution was not used here in order to distinguish the iterative solver error and the discretization error.

Also, the reference solution and the error e_{L_2} at $r = 5$ is not available because the direct solver fails due to the high condition number. A comparison of the number of required iterations and the solution error is shown in Figs. 14 and 15 with and without T_B and M. No degrees of freedom were constrained for $T = I$, denoted by $T_{tol} = \infty$. The combination of the geometric preconditioner and Jacobi solver preconditioner was not included here since both are diagonal preconditioners.

As expected, the number of required iterations is reduced with the preconditioning scheme using both the stabilized Lagrange and Nitsche methods. The solver preconditioners reduce the number of iterations more than the projection scheme alone. However, the Jacobi preconditioner is not robust as the solver fails for some of the values of r. The geometric preconditioning scheme may be combined with a solver preconditioner. The incomplete LU preconditioner with and without T_B has the fewest required iterations. In this case, the proposed preconditioning scheme adds robustness, ensuring an almost constant number of iterations for all interface geometries. While the geometric and solver preconditioners may be combined, the advantage of the geometric preconditioner is that it is computed prior to constructing the system matrices. This is particularly useful for large size and/or nonlinear problems, as the geometric preconditioner is only computed once for each interface configuration.
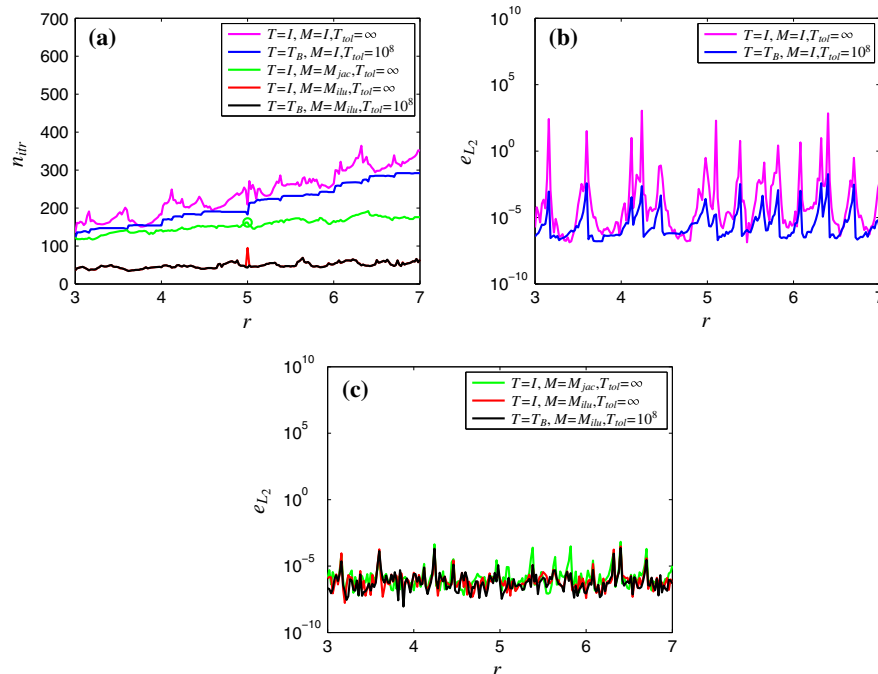

Fig. 14 The a number of iterations, b e_{L_2} with no solver preconditioner, and c e_{L_2} with solver preconditioners M_{jac} and M_{ilu} using the stabilized Lagrange method. The open circles in a mark the values of r at which the iterative solver failed to satisfy the stopping criterion
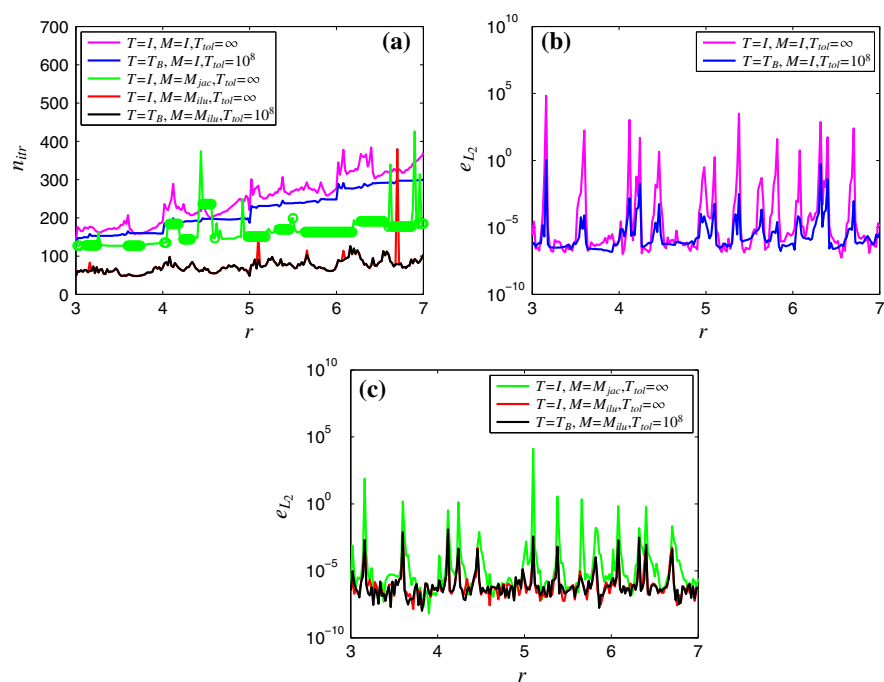
Fig. 15 The **a** number of iterations, **b** e_{L_2} with no solver preconditioner, and **c** e_{L_2} with solver preconditioners M_{jac} and M_{ilu} using Nitsche's method. The open circles in a mark the values of r at which the iterative solver failed to satisfy the stopping criterion
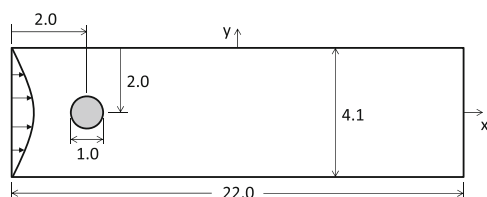

Fig. 16 Problem description for example 3

Fig. 17 Evolution of non-dimensional inlet and cylinder velocities

5.3 Example 3: moving cylinder in channel flow

In this example, a 2D transient nonlinear problem with a moving interface is considered. A rigid cylinder immersed in a channel flow is oscillating perpendicular to the inflow direction. The flow is modeled by the incompressible Navier–Stokes equations, and the motion of the cylinder is prescribed by defining the level set field as an explicit function of time. The problem setup is depicted in Fig. 16. Note the fluid problem is modeled and solved in non-dimensional form. We study the stability and accuracy of the flow solution with and without the proposed preconditioning scheme for different T_{tol} values for constraining degrees of freedom.

Along the channel inlet a parabolic inflow is prescribed. The outlet is assumed traction-free, and stick conditions are enforced at the upper and lower channel walls. The position
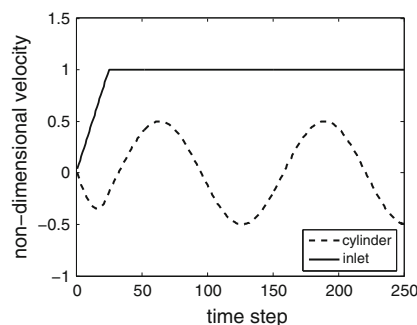
of the cylinder and velocity along the cylinder surface, i.e. fluid–solid interface, are determined from the prescribed evolution of the discretized level set field. The flow response is simulated over 250 time steps with a non-dimensional time step size of $\Delta t = 0.05$. To facilitate the transient simulation of the flow field, we ramp up over time both the inlet conditions and the motion of the cylinder. The velocity profiles of the cylinder and inlet flow are depicted in Fig. 17. The Reynolds number with respect to the maximum average inlet velocity is 100.

The weak form of the incompressible Navier–Stokes equations is discretized by four-node finite elements, i.e. the
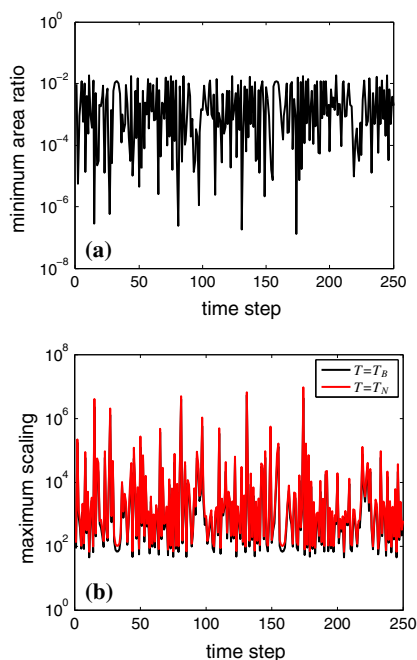
Fig. 18 The **a** minimum elemental fluid area ratio, and **b** the maximum entry in the preconditioning matrices T_N and T_B in each time step

Table 1 Maximum number of constrained degrees of freedom

T_{tol}	Max constrained dofs
10^8	0
10^6	3
10^4	9
10^2	18
10^1	30

velocity and pressure fields are approximated piecewise by bilinear, equal-order interpolations. To avoid numerical instabilities we employ an SUPG/PSPG stabilization scheme [34]. The velocity boundary condition along the fluid–solid interface is enforced by a stabilized Lagrange multiplier formulation [11]. The Lagrange multipliers are approximated element-wise by bilinear shape functions. The reader is referred to Kreissl and Maute [15] for additional details on the XFEM implementation of the flow model. The flow solution is advanced in time with an Euler-backward time integration scheme. In each time step, the nonlinear sub-problem is solved by the Newton–Raphson method, and a direct solver is applied to the linearized problem. The nonlinear residual is required to drop by 10% in each time step.

First we discretize the channel with 6912 elements and 7105 nodes. The mesh in the vicinity of the cylinder is uniform with a non-dimensional element size of 0.085×0.085. Initially, 48 elements are intersected by the fluid–solid interface and the flow field is approximated by 63, 255 degrees of freedom. As the cylinder oscillates, the intersection configuration, number of intersected elements, and number of degrees of freedom change slightly. The evolutions of the minimum ratio of elemental fluid area over the total elemental area and the maximum entries in the preconditioning matrix for the T_N and T_B formulations are shown in Fig. 18. The minimum area ratios of order 10^{-7} lead to large entries in the preconditioning matrix. The maximum entries in T_N are

slightly larger than the ones in T_B but are of the same order. The evolution of both formulations is similar.

We compare the performance of the proposed preconditioning scheme against an approach where only degrees of freedom with vanishing influence are constrained. We examine the evolution of the total horizontal and vertical forces acting on the cylinder, and we consider $T_{tol} = [10^8, 10^6, 10^4, 10^2, 10^1]$ for determining the constrained degrees of freedom. As shown in Fig. 18, the maximum value of the preconditioning matrix is less than 10^8 for all time steps. Therefore no degrees of freedom are constrained for $T_{tol} = 10^8$. For $T_{tol} \leq 10^6$, the number of constrained degrees of freedom increases as T_{tol} is reduced. The number of constrained degrees of freedom varies with time, and the maximum is shown in Table 1 when T_B is applied.

Without the proposed preconditioning scheme, the transient simulation diverges for $T_{tol} > 10^4$. The evolutions of the total horizontal and vertical forces for $T_{tol} = [10^4, 10^2, 10^1]$ are depicted in Fig. 19. Note, the results are shown only after 50 time steps for which the influence of ramping up the inlet and cylinder velocities has sufficiently faded. The force evolutions for $T_{tol} = 10^4$ and $T_{tol} = 10^2$ are similar. However, if T_{tol} is chosen too low, here $T_{tol} = 10^1$, the forces erroneously oscillate. The different intersection configurations due to the moving cylinder lead to oscillating errors, as discussed in Sect. 5.2. The smaller values for T_{tol} increase the error by constraining more degrees of freedom associated with small intersected areas. The proper choice of T_{tol} is not known *a priori*.

In contrast, no convergence issues were observed with the proposed preconditioning scheme for both formulations of the preconditioning matrix. In Fig. 20, the evolution of the total forces are shown using the T_B preconditioning matrix. Note, as the results for $T_{tol} = [10^8, 10^6, 10^4]$ are indistinguishable, only the results for $T_{tol} = [10^8, 10^2, 10^1]$ are shown. The results for the T_N preconditioning matrix are nearly identical and therefore not shown. Using either T_B or T_N in determining the degrees of freedom to be constrained to zero, a similar behavior can be observed: if T_{tol} is too low the forces erroneously oscillate with a high frequency. This behavior seems to be less pronounced when the preconditioning matrix is used.
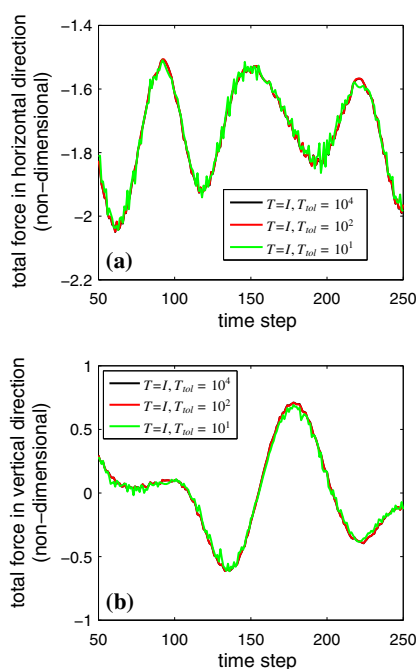
Fig. 19 Evolution of the total force in the **a** horizontal and **b** vertical directions for different values of T_{tol} when no geometric preconditioner is applied
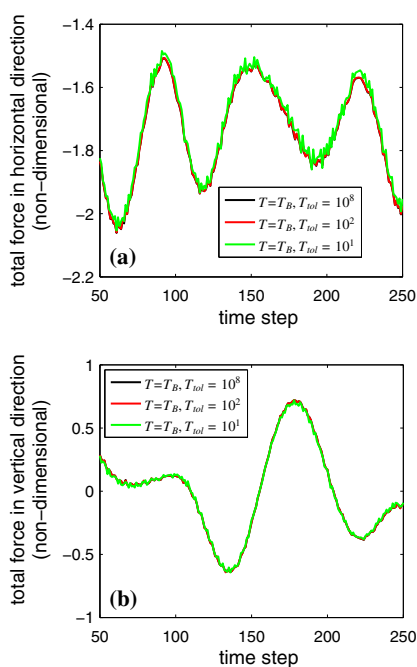

Fig. 20 Evolution of the total force in the **a** horizontal and **b** vertical directions for different values of T_{tol} using the T_B preconditioning matrix
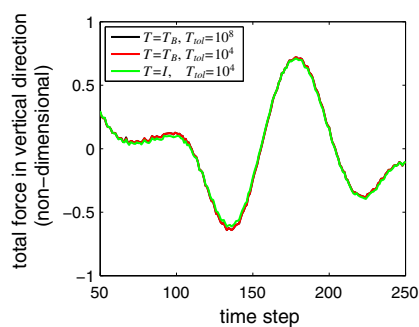

Fig. 21 Comparison of the total vertical force for different values of T_{tol} with and without T_B

Table 2 Mesh refinement study

Nodes	Elements	Intersected elements
7,105	6,912	48
12,545	12,288	64
28,033	27,648	92
37,465	37,044	120

A direct comparison of the results obtained with and without the T_B preconditioning matrix are depicted in Fig. 21. Here we only compare the total force in vertical direction for $T_{tol} = [10^8, 10^4]$. The results for the total force in the horizontal direction show similar behaviors and are therefore omitted. Recall the simulations diverge for $T_{tol} = 10^8$ when no preconditioner is used. While the results with T_B are indistinguishable for $T_{tol} = [10^8, 10^4]$, the cross-comparison between the force evolutions for $T_{tol} = 10^4$ shows a slight difference. This is attributed to the different convergence behavior; the convergence of the Newton–Raphson method is once monitored in the physical and once in the transformed space. As a stricter convergence is enforced, the difference decreases.

The robustness provided by the preconditioning scheme allows the problem to be solved on refined meshes. We examine the total horizontal and vertical forces acting on the cylinder using different mesh sizes. The considered mesh sizes and the number of initially intersected elements are given in Table 2. The evolution of the total force for a sequence of refined meshes is shown in Fig. 22. For $T_{tol} = 10^8$, no degrees of freedom were constrained for all mesh sizes. The force evolutions converge as the mesh is refined. The high frequency oscillations present in the coarsest mesh vanish with mesh refinement.

5.4 Example 4: circular inclusion interfacial debond

The fourth numerical example considers a problem with a strong discontinuity in the solution at the interface. Follow-
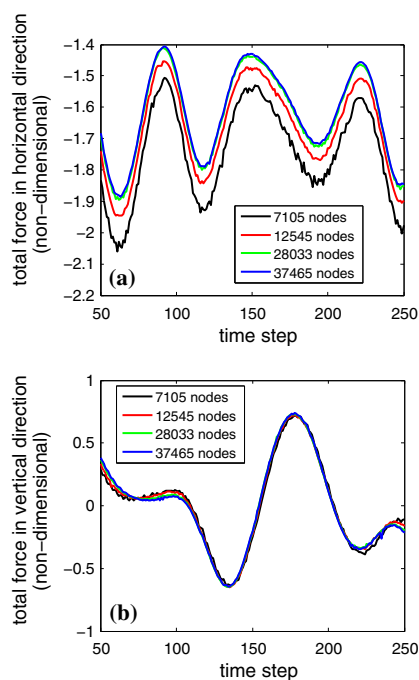
Fig. 22 Evolution of total vertical forces in horizontal and vertical directions for different mesh refinement levels using the T_B formulation of the geometric preconditioner with $T_{tol} = \infty$

Fig. 23 Problem description for example 4 shown with a mesh size of $h = 1$
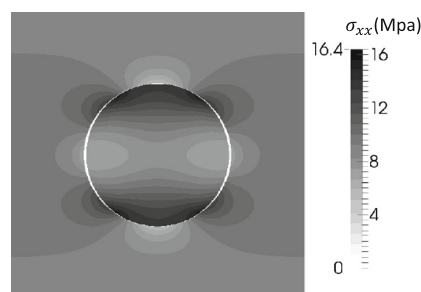
Fig. 24 Microscopic stress in the x direction with $h = 0.0625$ for example 4

ing the work in [17], the interfacial debonding in a micromechanical analysis of a composite material is studied using the proposed preconditioning scheme. The problem setup is depicted in Fig. 23. The problem is solved on a square domain with a centered circular fiber inclusion in tension along the x direction. The debond between the fiber and matrix is modeled before crack initiation under plane strain conditions. The radius of the fiber is varied from $r = 3$ to $r = 7$ mm in steps of $\Delta r = 0.02$, and the size of the domain is $L = 20$ mm. The Young's modulus and Poisson's ratio for the matrix material in $\mathcal{D}_1$ are $E_1 = 4.6$ GPa and $\nu_1 = 0.4$, respectively. The fiber material in $\mathcal{D}_2$ has $E_2 = 232$ GPa and $\nu_1 = 0.3$. The normal displacement at the bottom, left, and top edges is constrained to zero. The normal displacement at the right edge is specified as $u_d = 0.02$ mm.

The bilinear cohesive zone model described in [17] is used for the interface debond with the properties $\sigma_{max} = 0.01$ GPa, $\delta_c = 0.001$ mm, and $\delta_e = 0.02$ mm. The solution procedure uses 10 uniform steps to ramp up the specified displacement. Figure 24 shows the microscopic stress σ_{xx} for $r = 5$ mm with the debond between matrix and fiber depicted.

Two studies were performed for this example to investigate the performance of the preconditioning scheme. The first study compares the condition number of the system of equations with and without the geometric preconditioner. The sec-
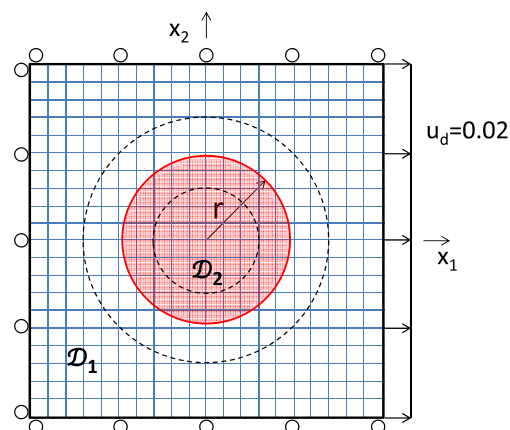
ond study shows the influence of T_{tol} on the condition number and solution accuracy. Note that the interface configurations for this example obtained by varying the inclusion radius are the same as Example 2. Therefore the minimum element area ratio shown in Fig. 10 also applies to this example for a mesh size of $h = 1$.

To study the performance of the preconditioning scheme on the conditioning of the system of equations, the condition number was computed for the final Newton iteration of the last solution step. There is little change in the condition number of the system of equations during the Newton iterations and load steps. The condition number was computed with no preconditioner and the T_N and T_B preconditioning matrices for a mesh size of $h = 1$. No degrees of freedom were constrained without the preconditioner, and $T_{tol} = 10^8$ was used for both preconditioning types. Figure 25 shows the condition number is reduced using the preconditioning schemes. For this problem, $T = T_B$ shows the best performance at reducing the condition number for all interface positions.

The second study investigates the influence of T_{tol} on the condition number and solution accuracy with and without the T_B preconditioning matrix. The value of T_{tol} is varied from
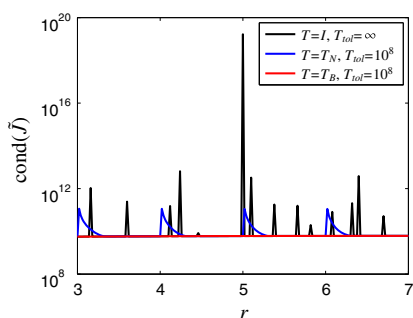
Fig. 25 Comparison of the condition number for a varying inclusion radius with $h = 1$ for example 4
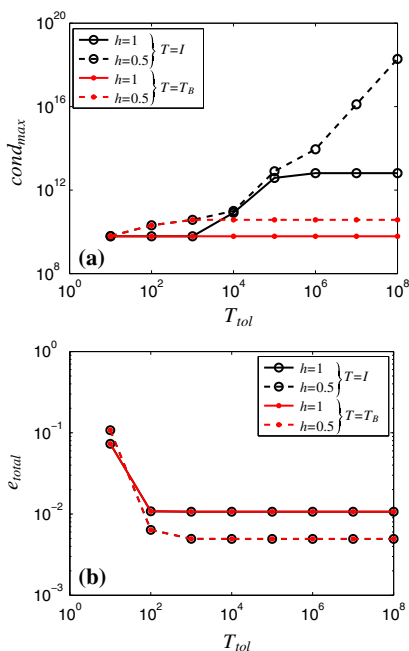

Fig. 26 Influence of T_{tol} on the **a** maximum condition number and **b** approximation error for example 4

$T_{tol} = 10$ to $T_{tol} = 10^8$, and the condition number for the final load step and displacement approximation u^h is determined for each value of r. For $T = I$, the preconditioning matrix is only used in (20) and not applied when solving the system of equations. The maximum condition number and total solution error are determined by (22–23). The reference solution, u_{ref}, is computed using XFEM with a uniform mesh of size $h = 0.0625$. The influence of T_{tol} on the maximum condition number and total solution error is shown in Fig. 26 with and without the preconditioning matrix for mesh sizes of $h = 1$ and $h = 0.5$. The influence of T_{tol} is similar to the results for Example 2 shown in Fig. 11. The maximum condition number is reduced by decreasing T_{tol} for $T = I$,

as more degrees of freedom are constrained to zero. But the solution error increases as the condition number is reduced. Using $T = T_B$, the maximum condition number is reduced for all values of T_{tol}. The insensitivity of the condition number with respect to T_{tol} for $T = T_B$ allows using a higher T_{tol}, which results in a lower solution error.

6 Conclusions

A simple and efficient preconditioning scheme has been proposed for Heaviside enriched XFEM problems which transforms the discretized governing equations into a well-conditioned form. The preconditioning scheme consists of a geometric preconditioner and constraining degrees of freedom to zero which interpolate the solution in small areas of intersection. The geometric preconditioner is constructed from the nodal basis functions and the interface configuration. Therefore the preconditioning matrix can be computed prior to constructing the system matrices, making it well-suited for nonlinear problems. The ill-conditioning due to small element intersections is eliminated, and the condition number of the system matrices is comparable to that of a body-fitted mesh using the traditional FEM.

Constraining degrees of freedom associated with small intersections is necessary. However, the proposed preconditioner reduces the sensitivity of the solution error with respect to the condition number. We have shown that when only selecting degrees of freedom to constrain to zero without the preconditioning matrix, there is a strong trade-off with reducing the condition number and a loss in solution accuracy. By implementing the proposed preconditioning scheme the condition number is reduced, and a loss in solution accuracy only occurs if the tolerance criterion for selecting the degrees of freedom to constrain is too small. The proposed preconditioning scheme also allows an infinitesimal level set shift for preventing intersections through a node or an element edge.

Generic solver preconditioners help to reduce the condition number, but they suffer from robustness issues and their performance depends on the formulation of the interface condition. The proposed preconditioning scheme is robust and efficient for solving linear and nonlinear problems. Additionally, the proposed approach performs well for discontinuous problems and C^0-continuous problems with both the stabilized Lagrange and Nitsche methods for enforcing continuity at the interface.

In this work two diagonal forms of the preconditioning matrix were studied. Additional approaches for building the preconditioning matrix can be further explored, including diagonal and non-diagonal forms. While this paper studied heat diffusion, fluid flow, and interfacial debonding, the preconditioning scheme is directly applicable to other problem types. However, as presented in this paper, the proposed

preconditioning scheme is specific to Heaviside enriched XFEM. Only 2D problems with static and prescribed moving interfaces were considered. The extension of the proposed preconditioning scheme to 3D problems is straight forward and is discussed in [36].

A formal and comprehensive comparison of the present preconditioner approach with that of [22] and [2] for C^0-continuous problems, while beyond the scope of this work, forms an ongoing study. Additionally, the performance of the preconditioning scheme for problems with dynamically evolving interfaces will be investigated in future studies.

References

1. Babuška I, Banerjee U (2012) Stable generalized finite element method (SGFEM). Comput Methods Appl Mech Eng 201–204:91–111

2. Béchet E, Minnebo H, Moës N, Burgardt B (2005) Improved implementation and robustness study of the X-FEM for stress analysis around cracks. Int J Numer Methods Eng 64:1033–1056

3. Belytschko T, Parimi C, Moës N, Sukumar N, Usui S (2003) Structured extended finite element methods for solids defined by implicit surfaces. Int J Numer Methods Eng 56:609–635

4. Chessa J, Belytschko T (2003) An extended finite element method for two-phase fluids. J Appl Mech 70:10–17

5. Chessa J, Smolinski P, Belytschko T (2002) The extended finite element method (xfem) for solidification problems. Int J Numer Methods Eng 53:1959–1977

6. Choi Y, Hulsen M, Meijer H (2012) Simulation of the flow of a viscoelastic fluid around a stationary cylinder using an extended finite element method. Comput Fluids 57:183–194

7. Ewing R, Iliev O, Lazarov R (2001) A modified finite volume approximation of second-order elliptic equations with discontinuous coefficients. SIAM J Sci Comput 23:1335–1351

8. Fernández-Méndez S, Huerta A (2004) Imposing essential boundary conditions in mesh-free methods. Comput Methods Appl Mech Eng 193:1257–1275

9. Fries TP (2008) A corrected X-FEM approximation without problems in blending elements. Int J Numer Methods Eng 75:503–532

10. Fries TP, Belytschko T (2010) The extended/generalized finite element method: an overview of the method and its applications. Int J Numer Methods Eng 84:253–304

11. Gerstenberger A, Wall WA (2010) An embedded Dirichlet formulation for 3D continua. Int J Numer Methods Eng 82:537–563

12. Hansbo A, Hansbo P (2004) A finite element method for the simulation of strong and weak discontinuities in solid mechanics. Comput Methods Appl Mech Eng 193:3523–3540

13. Hansbo P, Larson M, Zahedi S (2014) A cut finite element method for a stokes interface problem. Appl Numer Math 85:90–114

14. Juntunen M, Stenberg R (2008) Nitsche's method for general boundary conditions. Math Comput 78:1353–1374

15. Kreissl S, Maute K (2012) Levelset based fluid topology optimization using the extended finite element method. Struct Multidiscip Optim 46:311–326

16. Lang C, Doostan A, Maute K (2013) Extended stochastic fem for diffusion problems with uncertain material interfaces. Comput Mech 51:1031–1049

17. Li S, Ghosh S (2007) Modeling interfacial debonding and matrix cracking in fiber reinforced composites by the extended Voronoi cell FEM. Finite Elem Anal Des 43:397–410

18. Makhija D, Maute K (2014) Numerical instabilities in level set topology optimization with the extended finite element method. Struct Multidiscip Optim 49(2):185–197

19. Mandel J, Brezina M (1996) Balancing domain decomposition for problems with large jumps in coefficients. Math Comput 65:1387–1401

20. Menk A, Bordas S (2011) A robust preconditioning technique for the extended finite element method. Int J Numer Methods Eng 85:1609–1632

21. Moës N, Dolbow J, Belytschko T (1999) A finite element method for crack growth without remeshing. Int J Numer Methods Eng 46:131–150

22. Moës N, Cloirec M, Cartraud P, Remacle JF (2003) A computational approach to handle complex microstructure geometries. Comput Methods Appl Mech Eng 192:3163–3177

23. Osher S, Sethian J (1988) Fronts propogating with curvature-dependent speed: Algorithms based on Hamilton-Jacobi formulations. J Comput Phys 79:12–49

24. Reusken A (2008) Analysis of an extended pressure finite element space for two-phase incompressible flows. Comput Vis Sci 11:293–305

25. Rüberg T, Cirak F (2012) Analysis of an extended pressure finite element space for two-phase incompressible flows. Comput Vis Sci 209–212:266–283

26. Saad Y, Schultz M (1986) GMRES: A generalized minimal residual algorithm for solving nonsymmetric linear systems. SIAM J Sci Stat Comput 7:856–869

27. Sauerland H, Fries TP (2013) The stable XFEM for two-phase flows. Comput Fluids 87:41–49

28. Sethian J (1999) Level set methods and fast marching methods: evolving interfaces in computational geometry, fluid mechanics, computer vision, and materials science. Cambridge University Press, Cambridge

29. Soghrati S, Aragón A, Duarte C, Geubelle P (2010) An interface-enriched generalized finite element method for problems with discontinuous gradient fields. Int J Numer Methods Eng 00:1–19

30. Soghrati S, Thakre P, White S, Sottos N, Geubelle P (2012) Computational modeling and design of actively-cooled microvascular materials. Int J Heat Mass Transf 55:5309–5321

31. Stenberg R (1995) On some techniques for approximating boundary conditions in the finite element method. J Comput Appl Math 63:139–148

32. Sukumar N, Chopp D, Moës N, Belytschko T (2001) Modeling holes and inclusions by level sets in the extended finite element method. Comput Methods Appl Mech Eng 190:6183–6200

33. Terada K, Asai M, Yamagishi M (2003) Finite cover method for linear and non-linear analyses of heterogeneous solids. Int J Numer Methods Eng 58:1321–1346

34. Tezduyar TE, Mittal S, Ray SE, Shih R (1992) Incompressible flow computations with stabilized bilinear and linear equal-order-interpolation velocity-pressure elements. Comput Methods Appl Mech Eng 95:221–242

35. Tran A, Yvonnet J, He QC, Toulemonde C, Sanahuja J (2010) A multiple level set approach to prevent numberical artefacts in complex microstructures with nearby inclusions within XFEM. Int J Numer Methods Eng 85:1436–1459

36. Villanueva C, Maute K (2014) Density and level set-XFEM schemes for topology optimization of 3-d structures. Comput Mech 54(1):133–150

37. Wadbro E, Zahedi S, Kreiss G, Berggren M (2013) A uniformly well-conditioned, unfitted Nitsche method for interface problems. BIT Numer Math 53:791–820

38. Zabaras N, Ganapathysubramanian B, Tan L (2006) Modelling dendritic solidification with melt convection using the extended finite element method. J Comput Phys 218:200–227

Appendix C

Publication 3: Heaviside enriched extended stochastic FEM for problems with uncertain material interfaces

Heaviside Enriched Extended Stochastic FEM for Problems with Uncertain Material Interfaces

Christapher Lang · **Ashesh Sharma** ·
Alireza Doostan · **Kurt Maute**

Abstract This paper is concerned with the modeling of heterogeneous materials with uncertain inclusion geometry. The eXtended Stochastic Finite Element Method (X-SFEM) is a recently proposed approach for modeling stochastic partial differential equations defined on random domains. The X-SFEM combines the deterministic eXtended Finite Element Method (XFEM) with a Polynomial Chaos Expansion (PCE) in the stochastic domain. The X-SFEM has been studied for random inclusion problems with a C^0-continuous solution at the inclusion interface. This work proposes a new formulation of the X-SFEM using the Heaviside enrichment for modeling problems with discontinuous solutions at the uncertain inclusion interface. The Heaviside enrichment formulation employs multiple enrichment levels for each material subdomain which allows more complex inclusion geometry to be accurately modeled. A PCE is applied in the stochastic domain, and a random level set function implicitly defines the uncertain interface geometry. The Heaviside enrichment leads to a discontinuous solution in the spatial and stochastic domains. Adjusting the support of the stochastic approximation according to the active stochastic subdomain for each degree of freedom is proposed. Numerical examples for heat diffusion and linear elasticity are studied to illustrate convergence and accuracy of the scheme under spatial and stochastic refinements. In addition to problems with discontinuous solutions, the Heaviside enrichment is applicable to problems with C^0-continuous solutions by enforcing continuity at the interface. A higher convergence rate is achieved using the proposed Heaviside enriched X-SFEM for C^0-continuous problems when compared to using a C^0-continuous enrichment.

Keywords X-SFEM · Level Set Method · Heaviside Enrichment · Polynomial Chaos · Uncertainty Quantification

C. Lang
Structural Mechanics and Concepts Branch, NASA Langley Research Center, Hampton, VA

A. Sharma · A. Doostan (✉) · K. Maute
Aerospace Engineering Sciences, University of Colorado, Boulder, CO
E-mail: alireza.doostan@colorado.edu

1 Introduction

Computational methods for the propagation of uncertainties through models governed by partial differential equations are powerful tools for the prediction of a system's response, model validation, and engineering design. For heterogeneous composite materials, the material layout has uncertainty due to processing techniques. In order to relate the effective properties to the material layout, the uncertainty in geometry requires methods that account for the random material interfaces. This work proposes an approach to model problems with a strong discontinuity across a random material interface. Examples from this class of problems include imperfectly bonded interfaces, crack analysis, and the phonon Boltzmann transport model for heat diffusion at the submicron scale. The proposed approach is also applicable to problems with a weak discontinuity across the random material interface by enforcing a continuous solution using an interface constraint method such as the stabilized Lagrange multiplier and Nitsche methods [5, 18]. The proposed approach introduces the Heaviside enrichment function in the eXtended Stochastic Finite Element Method (X-SFEM) [12], which extends the eXtended Finite Element Method (XFEM) [10] to the stochastic domain using a Polynomial Chaos Expansion (PCE) [25] to approximate the degrees of freedom based on the random parameters characterizing the interface position.

Following the work by Hansbo and Hansbo [4], the Heaviside enriched XFEM is a deterministic approach for solving problems with discontinuities across an embedded interface without requiring a mesh which conforms to the interface geometry. The XFEM formulation in this work implements multiple enrichment levels to approximate all disconnected regions of the same phase [9, 21]. The use of additional enrichment levels accurately models neighboring intersected elements as well as elements intersected more than once. This implementation of the XFEM is particularly useful for modeling problems with a varying interface geometry, as mesh regeneration is avoided and robustness is added for more complex interface configurations.

A Monte Carlo (MC) simulation combined with the XFEM may be utilized to solve the stochastic problem. In Savvas et al. [14], the homogenization of random media with varying inclusion geometry is studied using the XFEM coupled with MC simulation. While the XFEM avoids remeshing for each realization of the inclusion geometry, numerous solutions may be required for sampling the varying inclusion geometry. An alternative is the X-SFEM [11], which requires one solution of a larger system of equations. The X-SFEM was recently introduced for modeling problems with C^0-continuous solutions at random material interfaces. The spatial domain is discretized by the XFEM and extended to the stochastic domain by a PCE based on the random parameters characterizing the uncertain interface geometry. The dimension of the stochastic domain is determined by the finite set of random parameters chosen to characterize the interface geometry. Each spatial degree of freedom is approximated in the stochastic space using a PCE, and a Galerkin projection leads to a finite system of equations to be solved for the expansion coefficients. The Wiener-Askey PCE [25] defines polynomial sets which are orthogonal with respect to the probability density function of the random parameters. The application of PCE may lead to exponential convergence rates if the degrees of freedom vary smoothly with respect to the random parameters. However, for non-smooth behavior of the degrees of freedom in the stochastic domain,

the PCE may converge slowly or fail to converge. The X-SFEM was studied for problems with C^0-continuous solutions at the random material interface with various enrichment functions in [6]. This work proposes a new implementation of the X-SFEM in order to solve problems with a discontinuous solution at the random material interface using the Heaviside enrichment function.

Building on the work in [6, 8], a method for extending the Heaviside enriched XFEM to the stochastic domain using a PCE is proposed. A random level set function is utilized to implicitly define the interface position, which depends on a set of random parameters. The Heaviside enrichment is required to model the strong discontinuity across the material interface, which leads to degrees of freedom that are discontinuous in the stochastic domain as well as in the spatial domain. Here a degree of freedom refers to an unknown in the XFEM system of equations. Each degree of freedom is a function of the random inputs. The discontinuous behavior in the stochastic domain results from each degree of freedom being nonzero for only a portion of the stochastic domain. To illustrate the discontinuous behavior of the degrees of freedom in the stochastic domain, consider the bimaterial bar example in Figure 1(a). The two material subdomains are given as $\mathcal{D}_1$ and $\mathcal{D}_2$, and the uncertain interface location is defined by $r(\boldsymbol{\xi})$ where $\boldsymbol{\xi}$ is a vector of random parameters. Each degree of freedom is nonzero (active) over part of the stochastic subdomain depending on the variation of the interface. An example of a degree of freedom (dof) variation for 2 random parameters is shown in Figure 1(b) in which the active subdomain is a rectangle in the stochastic domain.
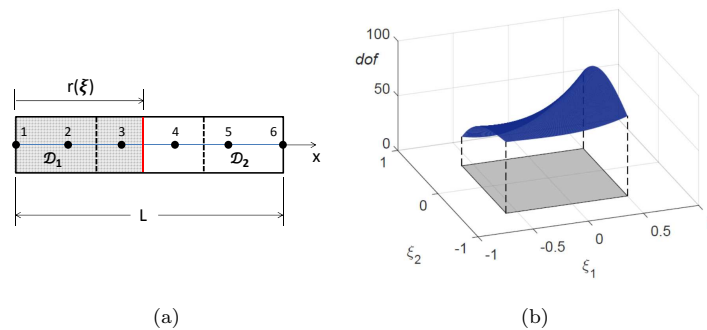

(a)   (b)

Fig. 1 (a) Bar example with an uncertain interface. (b) An active stochastic subdomain for 2 random parameters.

The X-SFEM generally uses a set of polynomial basis defined globally over the stochastic space for the approximation. Due to the non-smooth behavior and possibly local behavior of the degrees of freedom in the stochastic domain, such a global basis is not well suited. This work proposes adjusting the support of the PCE basis functions for the approximation of each degree of freedom. The support of the PCE basis functions are adjusted to match the active stochastic subdomain, e.g., the gray region in Figure 1(b). The adjustment of the PCE basis functions depends on the characterization of the interface geometry and is determined by the spatial mesh as well as the random level set function. Adjusting the support of the

PCE basis functions increases accuracy, and the system remains well-conditioned for higher approximation orders of the PCE.

The focus is on discontinuous and C^0-continuous example problems in heat diffusion and linear elasticity. While the proposed method is designed to solve problems with a strong discontinuity, C^0-continuous problems are included in order to compare the performance of the proposed approach with existing methods. The remainder of the paper is organized as follows: Section 2 defines the model problem and random level set function. The Heaviside enriched XFEM is presented in Section 3. The extension of the XFEM to the stochastic domain is described in Section 4. Four numerical examples are presented in Section 5 to describe and examine the performance of the proposed method.

2 Model Problems

The focus of this work is solving the model problem depicted in Figure 2 for heat diffusion and linear elasticity. The model problem contains an inclusion embedded in a matrix, and the geometry of the inclusion is uncertain. While the model problem consists of a material with a single random inclusion for simplicity, the proposed method is applicable to multiple inclusions. The level set method is used to define the random interface geometry. This section describes the setup and the governing equations for the model problem.

2.1 Domain Description

The governing equations are solved over the spatial domain $\mathcal{D} \subset \mathbb{R}^n$, and the probability space is denoted by $(\Sigma, \mathcal{B}, P)$. Here, Σ is the set of elementary events, $\mathcal{B}$ is the σ-algebra of events, and P is the probability measure. The random inclusion geometry is characterized by a finite set of random parameters, $\boldsymbol{\xi} : \Sigma \to \Omega \subseteq \mathbb{R}^d$. The spatial domain is comprised of two non-overlapping material subdomains, such that $\mathcal{D} = \mathcal{D}_1(\boldsymbol{\xi}) \cup \mathcal{D}_2(\boldsymbol{\xi})$. The material interface has zero thickness and is defined as $\Gamma(\boldsymbol{\xi}) = \mathcal{D}_1(\boldsymbol{\xi}) \cap \mathcal{D}_2(\boldsymbol{\xi})$. The boundary of $\mathcal{D}$ is comprised of a Dirichlet boundary, $\partial \mathcal{D}_D$, and a Neumann boundary, $\partial \mathcal{D}_N$.

2.2 Random Level Set

The level set method [15] is used to implicitly define the random interface geometry. The level set method is frequently used in the XFEM to define geometric features [2, 19, 20, 23]. A random level set function is introduced to define the random interface geometry for the model problem. The random interface location, $\Gamma(\boldsymbol{\xi})$, is defined by the zero contour of a random level set function $\phi(\boldsymbol{x}, \boldsymbol{\xi}) : \mathcal{D} \times \Omega \to \mathcal{R}$. The properties of $\phi(\boldsymbol{x}, \boldsymbol{\xi})$ are given by

$$\begin{aligned}
\phi(\boldsymbol{x}, \boldsymbol{\xi}) < 0 \quad &\text{if } \boldsymbol{x} \in \mathcal{D}_1(\boldsymbol{\xi}) \\
\phi(\boldsymbol{x}, \boldsymbol{\xi}) > 0 \quad &\text{if } \boldsymbol{x} \in \mathcal{D}_2(\boldsymbol{\xi}) \\
\phi(\boldsymbol{x}, \boldsymbol{\xi}) = 0 \quad &\text{if } \boldsymbol{x} \in \Gamma(\boldsymbol{\xi}).
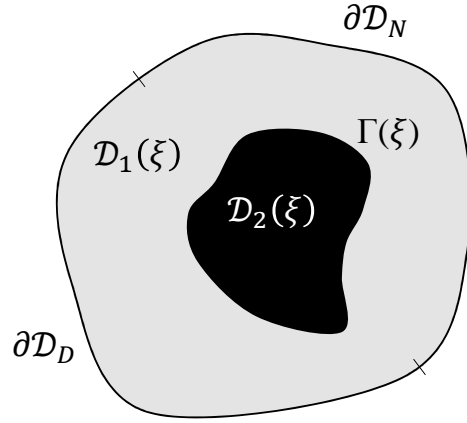\end{aligned} \tag{1}$$

Fig. 2 Schematic of the model problem with a single random inclusion.

The random level set function is discretized according to the finite element mesh of $\mathcal{D}$,

$$\phi(\boldsymbol{x}, \boldsymbol{\xi}) = \sum_{i \in I} M_i(\boldsymbol{x}) \phi_i(\boldsymbol{\xi}), \tag{2}$$

where $M_i(\boldsymbol{x})$ are the nodal basis functions, I is the set of all nodes in the mesh, and $\phi_i(\boldsymbol{\xi})$ is the value of the random level set function at node i. For this work, the basis functions used to interpolate the level set function $(M_i(\boldsymbol{x}))$ are the same as the basis functions used to interpolate the solution $(N_i(\boldsymbol{x})$, introduced in Section 3.2).

In this work, the characterization of the random interface geometry is assumed to be known. For realistic problems, the random interface characterization often requires a collection of measurement data for numerous outcomes of the interface geometry [16, 17]. The measurement data may be collected from various experimental approaches, such as optical images and micrographs. The approach used in this work to define the random level set function is by computing $\phi_i(\boldsymbol{\xi})$ as realizations of the interface geometry. An example of this approach uses the signed distance function, defined as

$$\phi(\boldsymbol{x}_i, \boldsymbol{\xi}) = \pm \min \|\boldsymbol{x}_i - \boldsymbol{x}_\Gamma(\boldsymbol{\xi})\| \tag{3}$$

where $\boldsymbol{x}_\Gamma(\boldsymbol{\xi})$ is the interface location, $\boldsymbol{x}_i$ is the spatial coordinate at node i, and $\|\cdot\|$ denotes the L^2-distance. With this approach, the random level set function is constructed by defining the interface location as a function of $\boldsymbol{\xi}$. Another example of defining the random level set function is discussed in Section 5.4.

2.3 Heat Diffusion with Random Geometry

The stationary heat diffusion equation is solved for a single inclusion with random interface geometry. The model heat diffusion problem consists of finding the ran-

dom temperature field, $u(\boldsymbol{x}, \boldsymbol{\xi})$, such that the following holds almost surely in Ω for phase $i = 1, 2$,

$$-\nabla \cdot (k \nabla u_i) = f \quad \text{in } \mathcal{D}_i(\boldsymbol{\xi})$$
$$(k \nabla u_i) \cdot \boldsymbol{n}_i = q_T \quad \text{on } \partial \mathcal{D}_i \cap \partial \mathcal{D}_N$$
$$u_i = u_T \quad \text{on } \partial \mathcal{D}_i \cap \partial \mathcal{D}_D, \tag{4}$$

where k is the thermal conductivity of an isotropic material, f is the volumetric heat source, and u_i denotes the restriction of u to $\mathcal{D}_i$. A temperature u_T is specified on $\partial \mathcal{D}_D$, and a heat flux q_T is specified on $\partial \mathcal{D}_N$ with an outward unit normal to $\mathcal{D}_i$ denoted by $\boldsymbol{n}_i$. The conductivity is defined as

$$k(\boldsymbol{x}, \boldsymbol{\xi}) = \begin{cases} 0 < k_{min} < k_1 < k_{\max} < \infty & \text{if } \boldsymbol{x} \in \mathcal{D}_1(\boldsymbol{\xi}) \\ 0 < k_{min} < k_2 < k_{\max} < \infty & \text{if } \boldsymbol{x} \in \mathcal{D}_2(\boldsymbol{\xi}) \end{cases} \tag{5}$$

with constants k_1 and k_2. For well-posedness, k_1 and k_2 are bounded by a minimum and maximum value. A thermal resistance is assumed to exist at the interface, which may be due to imperfect contact or a thin coating, leading to a discontinuous solution. The flux at the interface for the discontinuous solution is defined as

$$q_1 = \alpha(u_1 - u_2) \quad \text{on } \Gamma^-(\boldsymbol{\xi})$$
$$q_2 = -\alpha(u_1 - u_2) \quad \text{on } \Gamma^+(\boldsymbol{\xi}), \tag{6}$$

where q_1 and q_2 are the heat flux at the interface in the phase 1 and phase 2 domains, respectively, and α is the unit thermal conductance at the interface. The phase 1 side of the interface is denoted by Γ^-, and the phase 2 side of the interface is denoted by Γ^+. For imperfect contact, α represents the conduction across the interface with $\alpha = 0$ representing no conduction. For a thin layer, $\alpha = \frac{k_\Gamma}{t_\Gamma}$, where k_Γ and t_Γ are the conductivity and thickness of the interface layer. The solution is C^0-continuous for perfect thermal contact at the interface. In this case, continuity of the solution and flux across the random interface is enforced by the following interface conditions:

$$[\![u]\!] = u_1 - u_2 = 0 \quad \text{on } \Gamma(\boldsymbol{\xi})$$
$$k_1 \nabla u_1 \cdot \boldsymbol{n}_1 + k_2 \nabla u_2 \cdot \boldsymbol{n}_2 = 0 \quad \text{on } \Gamma(\boldsymbol{\xi}). \tag{7}$$

2.4 Linear Elasticity with Random Geometry

The model linear elasticity problem consists of finding the random displacement field, $\boldsymbol{u}(\boldsymbol{x}, \boldsymbol{\xi})$, such that the following holds almost surely in Ω for $i = 1, 2$,

$$-\nabla \cdot (\boldsymbol{\sigma}_i) = \boldsymbol{b} \quad \text{in } \mathcal{D}_i(\boldsymbol{\xi})$$
$$\boldsymbol{\sigma}_i \cdot \boldsymbol{n}_i = \boldsymbol{t}_d \quad \text{on } \partial \mathcal{D}_i \cap \partial \mathcal{D}_N$$
$$\boldsymbol{u}_i = \boldsymbol{u}_d \quad \text{on } \partial \mathcal{D}_i \cap \partial \mathcal{D}_D \tag{8}$$

where $\boldsymbol{\sigma}_i$ is the stress tensor and $\boldsymbol{u}_i$ is the displacement solution restricted to $\mathcal{D}_i$. The applied body forces are denoted by $\boldsymbol{b}$, and prescribed displacements $\boldsymbol{u}_d$ and tractions $\boldsymbol{t}_d$ are imposed on ∂D_D and ∂D_N, respectively. The constitutive relation for a linear elastic material is defined as

$$\boldsymbol{\sigma}_i = \boldsymbol{C}_i : \boldsymbol{\varepsilon}(\boldsymbol{u}_i) \quad \text{in } \mathcal{D}_i(\boldsymbol{\xi}), \tag{9}$$

where $\boldsymbol{C}_i$ is the elasticity tensor and $\boldsymbol{\varepsilon}$ is the strain tensor. Assuming small strains and displacements, the kinematics model is defined as

$$\boldsymbol{\varepsilon} = \frac{1}{2}(\nabla \boldsymbol{u}_i + \nabla \boldsymbol{u}_i^T). \tag{10}$$

A crack or other imperfect bond at the interface leads to a discontinuous displacement. A zero normal stress at the crack interface is assumed, defined as

$$\begin{aligned}
\sigma_1 \cdot \boldsymbol{n}_1 &= 0 \quad \text{on } \Gamma^-(\boldsymbol{\xi}) \\
\sigma_2 \cdot \boldsymbol{n}_2 &= 0 \quad \text{on } \Gamma^+(\boldsymbol{\xi}).
\end{aligned} \tag{11}$$

For a perfect bond at the interface, which gives a C^0-continuous solution, continuity of the displacement and normal stress across the random interface require

$$\begin{aligned}
[\![\boldsymbol{u}]\!] = \boldsymbol{u}_1 - \boldsymbol{u}_2 &= \boldsymbol{0} \quad \text{on } \Gamma(\boldsymbol{\xi}) \\
\boldsymbol{\sigma}_1 \cdot \boldsymbol{n}_1 + \boldsymbol{\sigma}_2 \cdot \boldsymbol{n}_2 &= 0 \quad \text{on } \Gamma(\boldsymbol{\xi}).
\end{aligned} \tag{12}$$

3 Heaviside Enriched X-FEM

The extended finite element [10, 19] uses an enrichment function to locally capture the non-smooth solution at the interface without requiring a mesh which conforms to Γ. Following the work by Hansbo and Hansbo [4] and Terada [21], a generalized Heaviside enrichment strategy is adopted which employs multiple enrichment levels [7–9]. The generalized Heaviside enrichment provides great flexibility in solving a broad range of partial differential equations with multiple phases for any choice of nodal basis functions. An advantage to using the Heaviside enrichment is that there are no issues with blending elements, which may exist for C^0-continuous enrichments. Also, neighboring intersected elements and elements intersected more than once can be modeled accurately using the generalized Heaviside enrichment strategy. This section defines the weak form of the governing equations (4)-(8) and the generalized Heaviside enrichment approach for solving the deterministic forms of the model problem.

3.1 Weak Form

The weak form of the governing equations for heat diffusion and linear elasticity are constructed by multiplying (4) and (8) by a set of admissible test functions and integrating over $\mathcal{D}$. The space $V = H^1(\mathcal{D})$ is the Hilbert space consisting of scalar functions with square integrable first derivatives and $V_0 = \{v \in V : v|_{\partial \mathcal{D}_D} = 0\}$.

Let $u \in V$ be the solution and $v \in V_0$ be an admissible test function. The weak form of the deterministic heat diffusion problem is stated as: Find $u \in V$ such that $u = u_t$ on $\partial \mathcal{D}_D$ and

$$\int_{\mathcal{D}} (\kappa \nabla u) \cdot \nabla v d\boldsymbol{x} - \int_{\mathcal{D}} f v d\boldsymbol{x} - \int_{\partial \mathcal{D}_N} q_t v ds + R_\Gamma = 0 \quad \forall v \in V_0, \qquad (13)$$

where s denotes the boundary of $\mathcal{D}$ and R_Γ includes the interface conditions in (6) for the discontinuous problem. For the continuous problem, $R_\Gamma = 0$. The space $W = H^1(\mathcal{D})$ is the Hilbert space consisting of vector functions with square integrable first derivatives and $W_0 = \{\boldsymbol{w} \in W : \boldsymbol{w}|_{\partial \mathcal{D}_D} = 0\}$. Let $\boldsymbol{u} \in W$ be the displacement and $\boldsymbol{w} \in W_0$ be an admissible test function. The weak form of the deterministic elasticity problem is stated as: Find $\boldsymbol{u} \in W$ such that $\boldsymbol{u} = \boldsymbol{u}_d$ on $\partial \mathcal{D}_D$ and

$$\int_{\mathcal{D}} \boldsymbol{\sigma} : \boldsymbol{\varepsilon}(\boldsymbol{w}) d\boldsymbol{x} - \int_{\mathcal{D}} \boldsymbol{b} \cdot \boldsymbol{w} d\boldsymbol{x} - \int_{\partial \mathcal{D}_N} \boldsymbol{t}_d \cdot \boldsymbol{w} ds + R_\Gamma = 0 \quad \forall \boldsymbol{w} \in W_0, \qquad (14)$$

where R^Γ is the enforcement of the interface conditions in (11) for the discontinuous problem.

The continuity equations in (7) and (12) were used to derive the weak form for both model problems. The interface conditions are included in R_Γ for the discontinuous problem. For discontinuous problems, the flux or normal stress at the interface are applied by multiplying (6) or (11) by the test functions and integrating along the interface.

3.2 Approximation

Consider a finite element mesh, $\mathcal{T}_h$, for $\mathcal{D}$ consisting of elements with edges that do not necessarily coincide with Γ. For a two phase problem with one level set function, an intersected element has a region corresponding to each of the two phases. The support of a nodal basis function includes multiple elements. If the support of a nodal basis function is intersected by the interface, there may be regions of the same phase which are not connected. A Heaviside enrichment function is implemented in the XFEM formulation, such that each disconnected region of the same phase is approximated by an independent set of nodal basis functions. The space V and W are comprised of the spaces for all disconnected regions and written as $V = \{v : v_i \in H^1(\mathcal{D})\}$ and $W = \{\boldsymbol{w} : \boldsymbol{w}_i \in H^1(\mathcal{D})\}$. Here, the subscript i represents the set of disconnected regions for each phase. The approximation of $u(\boldsymbol{x})$, denoted by $u^h(\boldsymbol{x})$, for two phases is defined as

$$u^h(\boldsymbol{x}) = \sum_{m=1}^{M} \left(H(-\phi(\boldsymbol{x})) \sum_{i \in I} N_i(\boldsymbol{x}) u_{i,m}^{(1)} + H(\phi(\boldsymbol{x})) \sum_{i \in I} N_i(\boldsymbol{x}) u_{i,m}^{(2)} \right), \qquad (15)$$

where I is the set of all nodes in $\mathcal{T}_h$, $N_i(\boldsymbol{x})$ is the nodal basis function, M is the maximum number of enrichment levels, and $u_{i,m}^{(q)}$ is the degree of freedom at node i for phase $q \in \{1, 2\}$. The Heaviside function is given by

$$H(z) = \begin{cases} 1 & z > 0 \\ 0 & z \leq 0 \end{cases}. \tag{16}$$

In this formulation, a single basis function, $N_i(\boldsymbol{x})$, is used at each node. Additional nodal degrees of freedom are added for each phase and enrichment level. Although (15) is written using the maximum possible number of enrichment levels, the specific number of enrichment levels at each node is determined by the spatial mesh and *a priori* knowledge of the interface location. The number of enrichment levels required depends on the number of disconnected regions of the same phase included in the support of $N_i(\boldsymbol{x})$. The approximation of $u(\boldsymbol{x})$ in (15) satisfies the partition of unity. Further details of this enrichment strategy are provided in [7, 9]. A key advantage of employing multiple enrichment levels using the Heaviside enrichment is that accurate solutions can be determined for neighboring intersected elements and elements intersected more than once using a single level set function, adding robustness for problems involving moving or changing interface geometry. For C^0-continuous problems, an interface constraint method is required for the Heaviside enrichment [1, 5, 18] to enforce the solution continuity across the interface in (7) and (12). Two common interface constraint formulations for enforcing continuity across material interfaces in the XFEM are the stabilized Lagrange and Nitsche methods, which are defined in [7, 9] for application to heat diffusion and linear elasticity.

4 Extended Stochastic FEM

The extended stochastic FEM (X-SFEM) [13] extends the XFEM to the stochastic framework using a PCE to model problems defined on random domains. The X-SFEM for C^0-continuous problems with random inclusions was introduced in [11] with a proposed enrichment function. The X-SFEM was studied for heat diffusion with a single random inclusion [6], specifically the accuracy and the smoothness of the degrees of freedom as a function of the random variables using various C^0-continuous enrichment functions. Requirements for a successful enrichment function were presented as well as a partitioning strategy for accurate integration in the probability domain. Here, the X-SFEM is studied for discontinuous problems with random inclusions by extending the Heaviside enriched formulation described in Section 3 to the stochastic domain using a PCE. The PCE approximates the variation of the spatial degrees of freedom with respect to the random parameters $\boldsymbol{\xi}$. In this work, a degree of freedom refers to the unknowns in the XFEM system of equations, and stochastic or expansion coefficients refer to the unknowns in the X-SFEM system of equations as described in Section 4.3. A PCE with global basis is well suited for a C^0-continuous enrichment function when the variation of the degrees of freedom is smooth and defined over the entire stochastic domain. However, a PCE with global basis is not well suited when using the Heaviside enrichment function in the X-SFEM. For the Heaviside enrichment, each degree of freedom is discontinuous as it is defined only on a subdomain of Ω. This subdomain is referred to as the active stochastic subdomain. Instead of a PCE with global support in the stochastic domain, adjusting the support of the PCE basis functions to account for the variation in the active stochastic subdomains is proposed. This

section defines the active stochastic subdomains, adjustment of the PCE basis functions, and construction of the system of equations.

4.1 Active Stochastic Subdomains

The active stochastic subdomain for each degree of freedom, denoted as $\Omega_{i,m}^{(q)} \subseteq \Omega$, defines the stochastic subdomain where the degree of freedom $u_{i,m}^{(q)}$ is nonzero. The active stochastic subdomain for each degree of freedom is determined by the intersection of $\phi(\boldsymbol{\xi}) = 0$ and the support of the nodal basis function in the XFEM approximation. For the linear basis functions used in this work, $\phi_j(\boldsymbol{\xi}) = 0$ is computed for the nodes of the elements sharing node i to determine the active stochastic subdomains. Each degree of freedom at node i is active for one or more of the regions created by $\phi_j(\boldsymbol{\xi}) = 0$. In general, each degree of freedom is active over a single connected subdomain. However, a degree of freedom may be active over disconnected regions depending on the discretization. In this case, additional enrichment levels are added such that each degree of freedom is active over a single connected subdomain.

The variation of the degrees of freedom is smooth over the active stochastic subdomain for which a polynomial approximation is well suited. As will be described, a PCE is constructed on the active stochastic subdomain using polynomial functions. For $d = 1$ and when $\xi : \Omega \to [-1, 1]$, $\Omega_{i,m}^{(q)}$ is defined by the interval $[a, b] \subseteq [-1, 1]$. For $d > 1$, the active stochastic subdomain is approximated by a hyperrectangle, $\hat{\Omega}_{i,m}^{(q)}$, and the product of one-dimensional polynomials are used to construct the PCE on $\hat{\Omega}_{i,m}^{(q)}$. A minimum bounding rectangle approximates the active stochastic subdomain, such that $\hat{\Omega}_{i,m}^{(q)} = [a_j, b_j] \subseteq [-1, 1]^d$ where $j = 1, \ldots, d$. For $d = 1$, $\hat{\Omega}_{i,m}^{(q)} = \Omega_{i,m}^{(q)}$. An example illustration of an approximate active stochastic subdomain for $d = 1$ and $d = 2$ is depicted in Figure 3(a)-(b). As discussed in the next section, a rotated $\hat{\Omega}_{i,m}^{(q)}$ may be required to closely approximate the area of the active stochastic subdomain, which is depicted in Figure 3(c).

The simple bar example is used to illustrate the active stochastic subdomains for $d = 1$. The bar depicted in Figure 1(a) has length $L = 1$ and is modeled using 5 elements. Let the interface position depend on one random parameter $r = 0.2\xi + 0.5$, where ξ is distributed uniformly over $[-1, 1]$, i.e., $\xi \sim U[-1, 1]$. The random level set function is given as $\phi(\xi) = x - r(\xi)$. The active stochastic subdomain for the degree of freedom interpolating the phase 2 solution at node 3, denoted $\Omega_{3,1}^{(2)}$, is defined by the interval $[-1, 0.5]$, and $\Omega_{4,1}^{(1)}$ is defined by the interval $[-0.5, 1]$. The intersection points $\xi = 0.5$ and $\xi = -0.5$ are computed from $\phi_4(\xi) = 0$ and $\phi_3(\xi) = 0$, respectively. Note that the other two active stochastic subdomains for nodes 3 and 4, $\Omega_{3,1}^{(1)}$ and $\Omega_{4,1}^{(2)}$ are defined by the interval $[-1, 1]$. The example in Section 5.1 further illustrates the active subdomains for $d = 1$ and depicts the variation of the degrees of freedom.
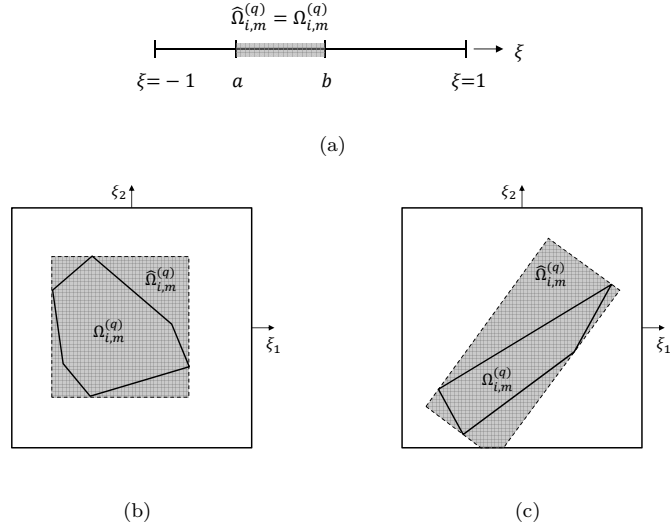
Fig. 3 Active stochastic subdomain for (a) $d = 1$, (b) $d = 2$, and (c) rotated in $d = 2$.

4.2 Approximation

In the X-SFEM, the Heaviside enrichment function and the degrees of freedom in (15) are functions of the random variables $\boldsymbol{\xi}$. For the Heaviside enriched formulation, the X-SFEM approximation of $u(\boldsymbol{x}, \boldsymbol{\xi})$ is defined as

$$
u^h(\boldsymbol{x}, \boldsymbol{\xi}) = \sum_{m=1}^{M} \left(H(-\phi(\boldsymbol{x}, \boldsymbol{\xi})) \sum_{i \in I} N_i(\boldsymbol{x}) u_{i,m}^{(1)}(\boldsymbol{\xi}) I_{i,m}^{(1)}(\boldsymbol{\xi}) \right.
$$

$$
\left. + H(\phi(\boldsymbol{x}, \boldsymbol{\xi})) \sum_{i \in I} N_i(\boldsymbol{x}) u_{i,m}^{(2)}(\boldsymbol{\xi}) I_{i,m}^{(2)}(\boldsymbol{\xi}) \right), \tag{17}
$$

where the indicator function I restricts the approximation of each degree of freedom $u_{i,m}^{(q)}(\boldsymbol{\xi})$ to the active stochastic subdomain $\hat{\Omega}_{i,m}^{(q)}$. The indicator function is defined as

$$
I_{i,m}^{(q)}(\boldsymbol{\xi}) = \begin{cases} 1 & \text{if } \boldsymbol{\xi} \in \hat{\Omega}_{i,m}^{(q)} \\ 0 & \text{otherwise} \end{cases}. \tag{18}
$$

Each degree of freedom, $u_{i,m}^{(q)}(\boldsymbol{\xi})$, is approximated in the stochastic space using a PCE of order p. A compact notation is introduced to define the set of degrees of freedom as $u_n(\boldsymbol{\xi})$, where n is an index to the set $\{i, m, q\}$ which consists of all nodes, enrichment levels, and phases. The stochastic approximation for a degree of freedom is defined by

$$
u_n(\boldsymbol{\xi}) = \sum_{j=1}^{M_{PC}} L_j^n(\boldsymbol{\xi}) a_j^n, \tag{19}
$$

where a_j^n are the stochastic coefficients to be determined and L_j^n are polynomials defined on $\hat{\Omega}^n$. For random variables with the independent uniform distributions considered in this work, multi-dimensional Legendre polynomials form an orthogonal basis with respect to the uniform measure, such that

$$\langle L_i, L_j \rangle = \int_{[-1,1]^d} L_i(\boldsymbol{\xi}) L_j(\boldsymbol{\xi}) P(\boldsymbol{\xi}) d\boldsymbol{\xi} = \langle L_i^2 \rangle \delta_{ij}, \tag{20}$$

where δ_{ij} denotes the Kronecker delta and $\langle \cdot \rangle$ denotes the mathematical expectation operator. The uniform measure is given as $P(\boldsymbol{\xi}) = (\frac{1}{2})^d I_{[-1,1]^d}$, where $I_{[-1,1]^d}$ is the indicator set of the hypercube $[-1,1]^d$ with d random variables. The Legendre polynomials in (20) are the standard basis defined on Ω. The polynomials L_j^n in the PCE (19) are defined on $\hat{\Omega}^n$, and are constructed by transforming the standard Legendre polynomials. While random variables with uniform distributions are considered in this work, local orthogonal polynomial bases for other distributions may be constructed numerically [22].

The proposed approach to construct L_j^n follows the multi-element generalized PCE [22], in which a single element in Ω is defined by $\hat{\Omega}^n$. The stochastic approximation is restricted to a single element to minimize the number of expansion coefficients to be determined by the system of equations. The L_j are scaled by a linear transformation from Ω to $\hat{\Omega}^n$ and normalized to construct L_j^n. The uniform random parameter ξ is defined on $[-1,1]$, and $\tilde{\xi}$ is a uniform random parameter defined on $[a,b]$. For $d=1$, constructing the L_j^n on the active stochastic subdomain uses the linear transformation

$$\tilde{\xi}_i = \frac{b_i - a_i}{2} \xi_i + \frac{b_i + a_i}{2} \quad \text{for } i = 1, \ldots, d. \tag{21}$$

Since $\langle L_i, L_j \rangle = \frac{1}{2i+1} \delta_{ij}$, the normalization constant is given as $\sqrt{2i+1}$. The transformed and normalized polynomials are defined on $\hat{\Omega}^n$ by

$$L_j^n(\tilde{\xi}) = \sqrt{2j+1} L_j(\xi(\tilde{\xi})), \tag{22}$$

and the L_j^n are zero outside of $\hat{\Omega}^n$. For $d > 1$, the multi-dimensional set of polynomials is constructed by the tensor product of one-dimensional polynomials with total order up to p [24]. The number of stochastic coefficients required in (19) is defined as

$$M_{PC} = \frac{(p+d)!}{p!d!}. \tag{23}$$

A comparison of the one-dimensional Legendre polynomials on $[-1,1]$ and the transformed and normalized Legendre polynomials on $[a,b] = [-0.75, 0]$ is shown in Figure 4 for $p = 3$. The transformed basis, L_j^n, is computed for each degree of freedom and avoids poorly conditioned systems resulting from small active stochastic subdomains.

Additionally for $d > 1$, the minimum bounding hyperrectangle and the active stochastic subdomain should have similar volumes. Otherwise an ill-conditioned system may result. Here, the focus is on $d = 2$, in which a minimum bounding rectangle is defined for the active stochastic subdomain. If the active stochastic
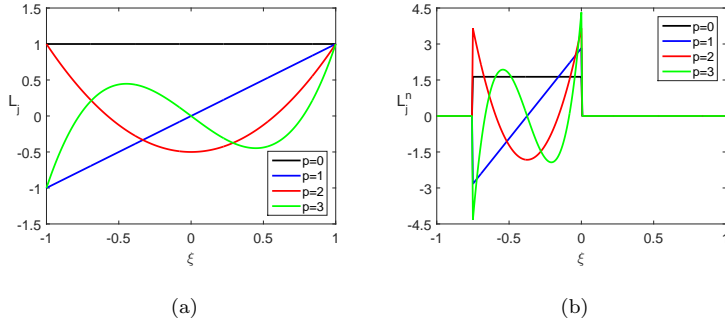
Fig. 4 (a) Legendre polynomials on $[-1, 1]$, and (b) transformed and normalized Legendre polynomials on $[-0.75, 0]$.

subdomain for $d = 2$ is a sliver, as depicted in Figure 5(a), the area of the minimum bounding rectangle does not closely match the area of the active stochastic subdomain. A rotated coordinate system is required in order for the bounding rectangle to closely approximate the active stochastic subdomain. The rotation for $d = 2$ is defined by the angle α, and the rotated coordinate system is $\boldsymbol{\xi}' = \boldsymbol{T}\boldsymbol{\xi}$. With α specified as the angle from the positive ξ_1 axis to the longest bounding box edge, the rotation to the reference coordinate system is defined as

$$\boldsymbol{T} = \begin{bmatrix} \cos(-\alpha) & -\sin(-\alpha) \\ \sin(-\alpha) & \cos(-\alpha) \end{bmatrix}. \tag{24}$$
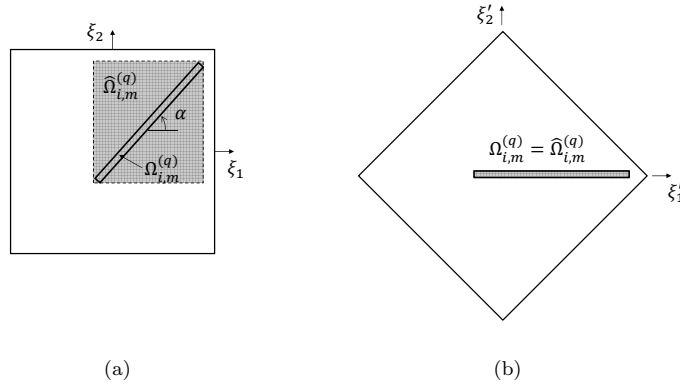
Fig. 5 (a) Example sliver configuration of an active stochastic subdomain for $d = 2$, and (b) the rotated coordinate system for defining the minimum bounding rectangle.

The rotated coordinate system for the example sliver configuration is shown in Figure 5(b). In this case, the minimum bounding rectangle matches the active stochastic subdomain using the rotated coordinate system. The transformed basis,

L_j^n, is computed using the rotated coordinate system. While the rotation is needed for defining the active stochastic subdomain for some degrees of freedom, $\boldsymbol{\xi}$ is used throughout the rest of the paper without reference to $\boldsymbol{\xi}'$. The rotated coordinate system is applied for the numerical examples in this work when the ratio of the minimum bounding rectangle area to the active area is greater than 2 for $d = 2$.

The uniform distribution of $\boldsymbol{\xi}$ is not preserved under a rotation, therefore the Legendre basis in $\boldsymbol{\xi}'$ is not orthogonal with respect to the measure of $\boldsymbol{\xi}'$ on $\hat{\Omega}^n$ when the rotation is utilized. However, it is straightforward to see that this basis is orthogonal with respect to the uniform density over $\hat{\Omega}^n$. In the subsequent formulations, the expectations are therefore taken with respect to the uniform density $\hat{\Omega}^n$ when a coordinate rotation is performed. Additionally, the rotation may lead to an active stochastic subdomain which extends beyond Ω, as illustrated in Figure 3(c). Since $\hat{\Omega}^n \subseteq \Omega$, the L_j^n are computed only within Ω.

Finally, active stochastic subdomains with small areas may lead to an ill-conditioned system. In order to avoid the ill-conditioning, the area of the active stochastic subdomain (A_Ω) is required to be greater than a minimum value. A tolerance is implemented such that the coefficients of the PCE for degrees of freedom with $A_\Omega < A_{tol}$ are constrained to zero. By doing so, the variation of the degree of freedom in Ω is neglected. A tolerance value of $A_{tol} = 10^{-6}$ was implemented for the numerical examples in this work, for which degrees of freedom were constrained only in Example 3.

4.3 System of Equations

In this section, the system of equations that results from the spatial and stochastic discretizations is described. The semi-discretized system of equations defined in (13) and (14) can be written in matrix form as

$$\boldsymbol{K}(\boldsymbol{\xi})\boldsymbol{u}(\boldsymbol{\xi}) - \boldsymbol{f}(\boldsymbol{\xi}) = \boldsymbol{0}, \tag{25}$$

where $\boldsymbol{K}$ is the conduction or stiffness matrix, $\boldsymbol{f}$ is the load vector, and $\boldsymbol{u}$ represents the vector of nodal degrees of freedom. The number of degrees of freedom is denoted by N_{FE}, and the dependency on the random inclusion geometry is included by the random vector $\boldsymbol{\xi}$. Following the approach outlined in [6], the system of equations is constructed to solve for the expansion coefficients in (19). However, the transformed polynomial basis L_j^n is specific to each spatial degree of freedom in this work. The polynomial expansion of each degree of freedom (19) is introduced into (25), and the Galerkin projection of the residual leads to a coupled system of equations for the vector of coefficients, $\boldsymbol{a}_j$, i.e.,

$$\sum_{k=1}^{M_{PC}} \langle \boldsymbol{K}_{ij}(\cdot)L_k^i(\cdot)L_l^j(\cdot)\rangle \boldsymbol{a}_k - \langle \boldsymbol{f}_i(\cdot)L_l^i(\cdot)\rangle = \boldsymbol{0}, l = 1, \ldots, M_{PC}. \tag{26}$$

The $(M_{PC} \cdot N_{FE}) \times (M_{PC} \cdot N_{FE})$ system of equations is written in compact form as

$$\boldsymbol{K}_s \hat{\boldsymbol{a}} - \boldsymbol{f}_s = \boldsymbol{0}, \tag{27}$$

where $\boldsymbol{K}_s$ and $\boldsymbol{f}_s$ are assembled from each spatial element integrated over Ω. The vector $\hat{\boldsymbol{a}}$ collects all of the expansion coefficients for the vector $\boldsymbol{u}(\boldsymbol{\xi})$. Each lth sub-vector component of the element vector $\boldsymbol{f}_s^e$ is defined as

$$(\boldsymbol{f}_s^e)_l = \langle \boldsymbol{f}_i^e(\cdot) L_l^i(\cdot) \rangle \quad \text{for } l = 1, \ldots, M_{PC}, \tag{28}$$

and each (k, l) block of the element matrix $\boldsymbol{K}_s^e$ is defined as

$$(\boldsymbol{K}_s^e)_{kl} = \langle \boldsymbol{K}_{ij}^e(\cdot) L_k^i(\cdot) L_l^j(\cdot) \rangle \quad \text{for } k, l = 1, \ldots, M_{PC}. \tag{29}$$

Here, (i, j) are indices for the degrees of freedom belonging to the nodes of element e in the finite element mesh, and (i, j) are not summed. The polynomial basis L^i is defined on $\hat{\Omega}^i$.

The element quantities $\boldsymbol{K}_s^e$ and $\boldsymbol{f}_s^e$ are computed by integrating over the spatial and stochastic domains. The spatial domain is partitioned for an intersected element for accurate integration over $\mathcal{D}$, which is standard practice in the XFEM. The partition is constructed to align with the interface, as described in [2, 7]. The integration over Ω also requires a partition for accuracy, since $\boldsymbol{K}^e(\boldsymbol{\xi})$ and $\boldsymbol{f}^e(\boldsymbol{\xi})$ vary piecewise smoothly with $\boldsymbol{\xi}$. Partitioning of Ω is also standard practice for the X-SFEM. However, the proposed approach for using the Heaviside enrichment requires a specific partitioning technique, which is described as follows. The domain in which the response varies smoothly is bounded by the intersection of $\phi_i(\boldsymbol{\xi}) = 0$ with the support of the basis functions. Therefore, $\phi_i(\boldsymbol{\xi}) = 0$ for the degrees of freedom at the nodes of the element and its neighbors are used to define the stochastic partition. Additionally, $\hat{\Omega}_i$ is considered in the construction of the stochastic partition, as it defines the nonzero subdomain for the PCE. The element stochastic partition is constructed using the union of $\phi_i(\boldsymbol{\xi}) = 0$ for the nodes of the element and its neighbors, as well as $\hat{\Omega}_i$ for the nodes of the element. Each element stochastic partition is potentially different, as well as each $\hat{\Omega}_i$, which leads to increased computational costs. However, constructing the element stochastic partition and performing the element integration are well suited for efficient parallel processing.

In this work, a triangulation is used for the partition of the $2D$ spatial domain. A linear interpolation of the level set field is used in this work. For integration in the spatial domain, the triangular partition of an intersected element aligns with the interface. Therefore the numerical integration in the spatial domain is exact for a properly chosen integration rule determined by the weak form of the governing equation. For $d = 1$, the partition of the stochastic domain is constructed using points according to $\phi_i(\xi) = 0$ where i is the set of nodes of the element and its neighbors. For $d = 2$, the stochastic partition is constructed using a triangulation of the bounding rectangle edges of the active stochastic subdomains for the element nodes as well as $\phi_i(\boldsymbol{\xi}) = 0$, where i is again the set of nodes of the element and its neighbors. An example partition of the stochastic domain is illustrated in Figure 6(a) for $d = 1$ with 4 points for $\phi_i(\xi) = 0$. Figure 6(b) depicts a triangulated stochastic partition for $d = 2$ with 4 edges for $\phi_i(\boldsymbol{\xi}) = 0$ and 2 minimum bounding rectangles for $\hat{\Omega}^n$. For integration in the stochastic domain, a local error is introduced from solving $\phi_i(\boldsymbol{\xi}) = 0$ for $d = 1$ and $d = 2$. Additionally, the zero level set curves are assumed to be linear for $d = 2$. Note that the integration rule for the stochastic domain depends on the chosen order of the PCE.
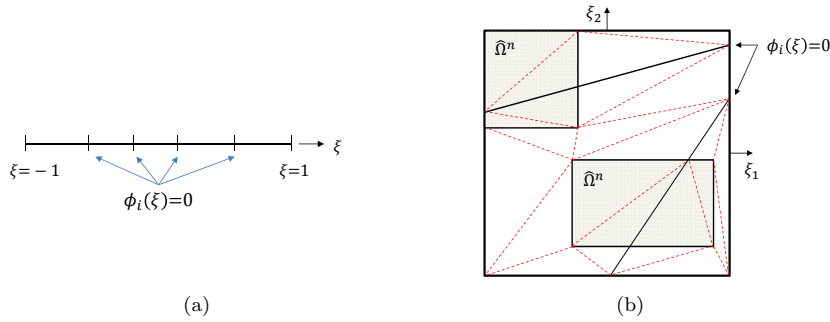
Fig. 6 Example stochastic partition for (a) $d = 1$ and (b) $d = 2$. The triangulation for $d = 2$ is denoted by the dashed red lines.

5 Numerical Examples

Four numerical examples are presented to study the convergence and accuracy of the proposed Heaviside enriched X-SFEM. The first two numerical examples have one random parameter and an analytical solution for investigating convergence of the method. The inclusion geometry in the third and fourth numerical examples is characterized by two random parameters in order to demonstrate the proposed method for problems with a two-dimensional stochastic domain. Example problems with continuous and discontinuous solutions are studied in this section. Solving problems with continuous solutions using the Heaviside enriched X-SFEM allows a comparison with the X-SFEM using a C^0-continuous enrichment [11]. The first three examples have C^0-continuous solutions while the solution is discontinuous in the fourth numerical example. The C^0-continuous enrichment used in the following examples was proposed in [11].

5.1 Example 1: Diffusion in a Two-Material Bar

The first numerical example solves the heat diffusion problem (4) for the two-material bar shown in Figure 7. The bar has length $L = 20$ with a centered inclusion of length $2r(\xi)$. The material interface is described by one random parameter, such that $r(\xi) = 5 + 2.5\xi$ and ξ has a uniform distribution $U(-1, 1)$. The inclusion geometry for $r = 5$ is shaded in Figure 7, and the dashed lines represent the variation of the inclusion geometry. The material conductivity in $\mathcal{D}_1$ and $\mathcal{D}_2$ is $k_1 = 2$ and $k_2 = 20$, respectively. The temperature at the left boundary is specified as $u_1 = 0$, and the temperature at the right boundary is specified as $u_2 = 100$. While the problem is one-dimensional in the physical domain, this example is modeled using 20 quadrilateral elements. The solution in the spatial domain for a specific value of ξ is piecewise constant over three subdomains. The chosen spatial discretization reproduces the exact solution and contributes zero error to the approximation.

Two studies are performed for this example. First, the degree of freedom approximation as a function of ξ is examined and compared to solving multiple

XFEM solutions for different interface positions. Second, the convergence of the solution error with respect to the stochastic approximation order p is determined. The stabilized Lagrange and Nitsche methods with a constraint factor of $k_1 + k_2$ are used to enforce solution continuity at Γ. The solutions using these methods were almost identical for the example problem, and the solution using the stabilized Lagrange method is shown. This example problem was studied in [6] using the X-SFEM with the C^0-continuous enrichment.
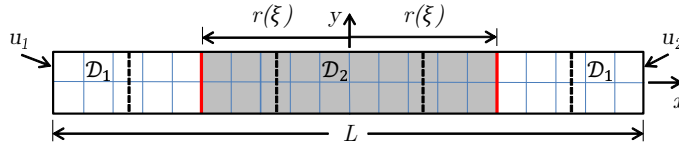
Fig. 7 Problem description for Example 1, shown with mesh size $h = 1$.

In order to show the variation of the degrees of freedom as a function of ξ, the deterministic solution is solved for $\xi = -1$ to $\xi = 1$ in steps of $\Delta\xi = 0.01$. The deterministic solution is computed using the XFEM by solving multiple problems for various interface positions defined by $r(\xi)$. It is noted that a preconditioner is required in the XFEM for varying interface positions in order to avoid an ill-conditioned system of equations due to possible element intersections with a small ratio of volumes on either side of the interface [7]. A preconditioner was not used in the X-SFEM. The variation of the degrees of freedom for the node located at $\boldsymbol{x} = (5, 0)$ are shown in Figure 8. The X-SFEM approximation for $p = 1$ is shown for comparison. The support of the PCE basis for the stochastic approximation is defined by the active subdomain. Note that the interface constraint formulation couples the phase 1 and 2 degrees of freedom. Increasing the order of the PCE reduces the error in the X-SFEM solution, as shown in the second part of this numerical example.

The accuracy of the X-SFEM solution is measured by the relative error defined by

$$e = \frac{\|u - \hat{u}\|_{L^2(\Omega;L^2(\mathcal{D}))}}{\|u\|_{L^2(\Omega;L^2(\mathcal{D}))}}, \tag{30}$$

where u denotes the analytical solution and $\hat{u}$ denotes the X-SFEM solution. The relative error is computed for each stochastic approximation order, p, and the convergence of the error is shown in Figure 9. The error convergence for the proposed Heaviside enriched X-SFEM is compared with the X-SFEM using the C^0-continuous enrichment. While the error for the Heaviside enriched X-SFEM is higher, the convergence rate for both approaches is the same. The difference in the magnitude of the error occurs because the C^0-continuous enrichment function is piecewise linear in ξ while the Heaviside enrichment is piecewise constant.
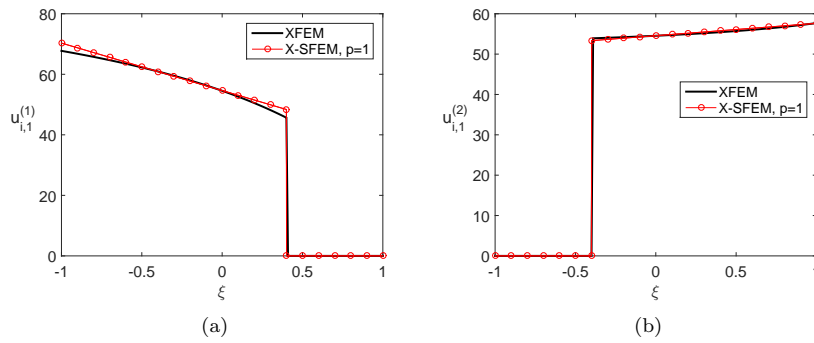
Fig. 8 The (a) phase 1 and (b) phase 2 degree of freedom values as a function of ξ for the node located at $\boldsymbol{x} = (5,0)$ using the XFEM and X-SFEM.
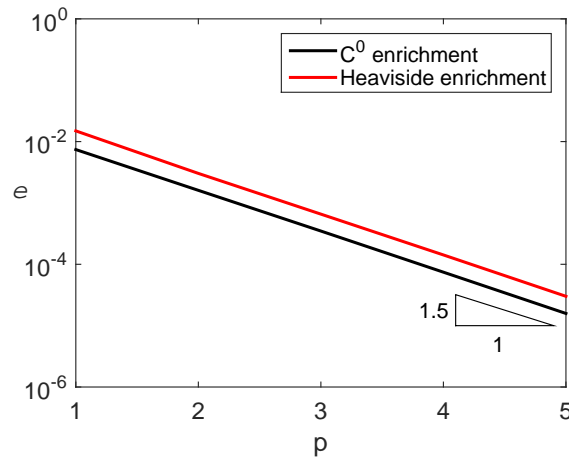

Fig. 9 Convergence of the relative error for the X-SFEM with the C^0 and Heaviside enrichment.

5.2 Example 2: Linear Elastic Bimaterial Plate

The second numerical example solves the linear elasticity problem (8) for the circular inclusion shown in Figure 10. A circular plate of radius $b = 2$ has a centered circular inclusion of radius r. The radius of the inclusion is determined by a single random parameter with a uniform distribution $U(-1,1)$. The inclusion radius is given by $r = 1.26 + 0.54\xi$. The elastic modulus and Poisson's ratio of the plate are $E_1 = 10$ and $\nu_1 = 0.3$. The elastic modulus and Poisson's ratio of the inclusion are given by $E_2 = 1$, $\nu_2 = 0.25$. A radial displacement is prescribed at the boundary of the plate, such that $\boldsymbol{u}_d = \boldsymbol{x}$. The stabilized Lagrange method [9] is used to

enforce continuity at the interface with a constraint factor $\gamma = 100(E_1 + E_2)$. This problem is studied using the proposed Heaviside enrichment in X-SFEM as well as the C^0-continuous enrichment proposed in [11].
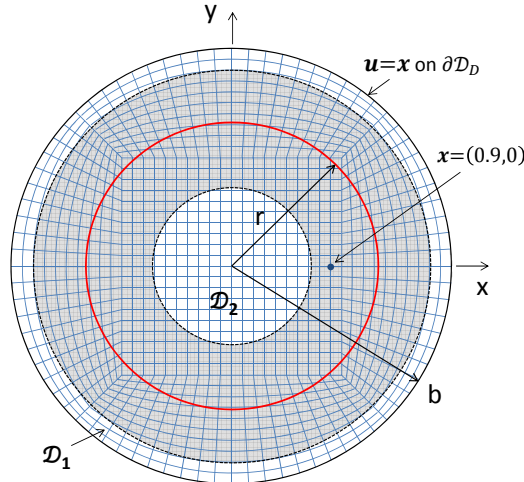

Fig. 10 Problem description for Example 2, shown with mesh size $h = 0.1$.

Two studies are performed for this example. First, the behavior of the degrees of freedom in the stochastic domain is compared using the C^0-continuous and Heaviside enrichment function for a deterministic sweep. The second study examines the accuracy of the X-SFEM solution and compares the convergence for the Heaviside and C^0-continuous enrichment functions.

As in the first example, the XFEM solution is determined for numerous values of ξ in order to examine the behavior of the degrees of freedom in the stochastic domain. The deterministic problem is solved for $\xi = -1$ to $\xi = 1$ with steps of $\Delta\xi = 0.01$. The degrees of freedom for the x-displacement at $\boldsymbol{x} = (0.9, 0)$ is shown in Figures 11 and 12 using the C^0-continuous and Heaviside enrichment functions, respectively. As discussed in [6] and shown here, the variation of the degrees of freedom using the C^0-continuous enrichment is not smooth with respect to ξ. The peaks correspond to the intersection of the interface with a node, therefore more peaks occur as the spatial mesh is refined. While some improvement in smoothness occurs with spatial mesh refinement, a smooth behavior of the degrees of freedom depends on a converged spatial mesh for the C^0-continuous enrichment. Using the Heaviside enrichment, the behavior of the degrees of freedom is piecewise smooth in the stochastic domain for any spatial mesh size, as depicted in Figure 12 for three spatial mesh sizes. The value of ξ at which the degree of freedom becomes active changes with mesh size. A second level degree of freedom exists at this node for phase 2 using the Heaviside enrichment, which is due to disconnected regions of phase 2 occurring for $-0.667 \leq \xi \leq -0.656$). The additional degree of freedom varies smoothly over this small active stochastic subdomain and is zero elsewhere.

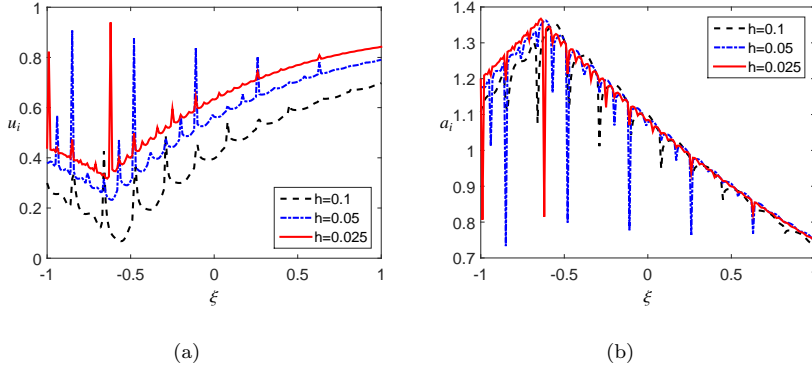A description of why additional enrichment levels may be required for the same phase is included in [7].

(a)   (b)

Fig. 11 (a) The regular and (b) enriched degree of freedom using the C^0 enrichment function for the x-displacement at $\boldsymbol{x} = (0.9, 0)$ as a function of ξ with spatial mesh refinement.
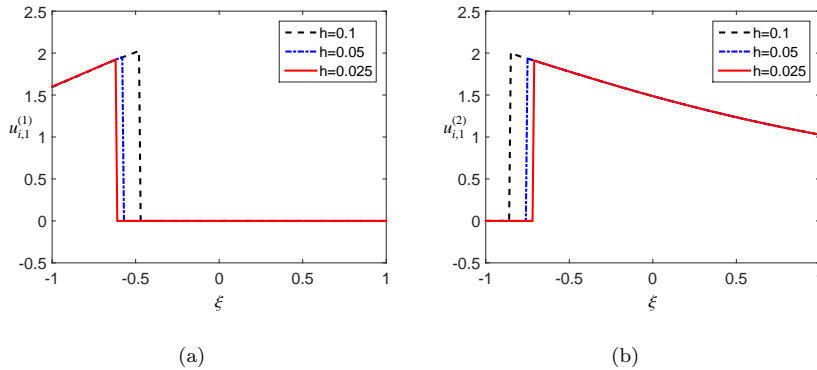

(a)   (b)

Fig. 12 The level 1 degrees of freedom for (a) phase 1 and (b) phase 2 using the Heaviside enrichment function for the x-displacement at $\boldsymbol{x} = (0.9, 0)$ as a function of ξ with spatial mesh refinement.

The analytical solution [19] is used to compute the relative error (30) in the X-SFEM solution. A comparison of the solution error using the C^0-continuous and Heaviside enrichment functions is shown in Figure 13 for three spatial mesh sizes. A higher convergence rate is achieved using the Heaviside enrichment. The spatial error dominates as each curve flattens as p is increased using the Heaviside enrichment.
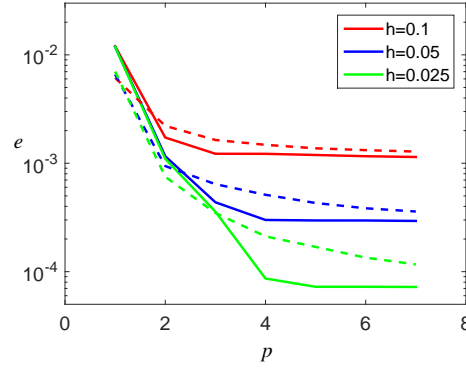
Fig. 13 Error convergence using the X-SFEM with respect to p for Example 2. Solid and dashed lines represent the Heaviside and C^0-continuous enrichment functions, respectively.

5.3 Example 3: Two Parameter Material Inclusion

The third numerical example studies the proposed Heaviside enriched X-SFEM for an inclusion geometry defined by two random parameters, resulting in a two-dimensional stochastic domain. The example problem solves the heat diffusion problem (4) for the random material inclusion with $d = 2$ depicted in Figure 14. This problem was presented in [6] using a C^0 enrichment function. A square domain with $L = 20$ has a random inclusion with radius $r(\theta, \boldsymbol{\xi})$ defined by two random parameters with independent uniform distributions $U(-1, 1)$. The thermal conductivity of $\mathcal{D}_1$ and $\mathcal{D}_2$ are $k_1 = 2$ and $k_2 = 20$, respectively. The stabilized Lagrange method is used for enforcing continuity at the interface with a constraint factor of $\gamma_S = k_1 + k_2$. The temperature on the left and right side is specified as $u_T = 0$ and $u_T = 100$. A tolerance of $A_{tol} = 10^{-6}$ is used for constraining to zero the coefficients of the PCE for degrees of freedom with small active stochastic subdomains. The radius of the inclusion is given by

$$r(\theta, \boldsymbol{\xi}) = \bar{r} + \sigma \sum_{k=1}^{2} \frac{1}{k} \xi_k \left[\cos(k^2\theta) + \sin(k^2\theta) \right], \tag{31}$$

where $\bar{r} = 4$ and $\sigma = 1$. The angle θ is measured counterclockwise from the positive x-axis.

The convergence of the X-SFEM solution with spatial and stochastic refinement is studied. Since an analytical solution does not exist for this problem, the expectation of the solution is computed and compared with a reference solution. The expectation of the X-SFEM solution is defined by

$$\|u\|_E^2 = \left\langle \int_{\mathcal{D}} (k\nabla u)^T \nabla u d\boldsymbol{x} \right\rangle. \tag{32}$$

The Monte Carlo (MC) reference solution is computed from numerous XFEM solutions using a random sampling of $\boldsymbol{\xi}$. A least-squares polynomial chaos regression
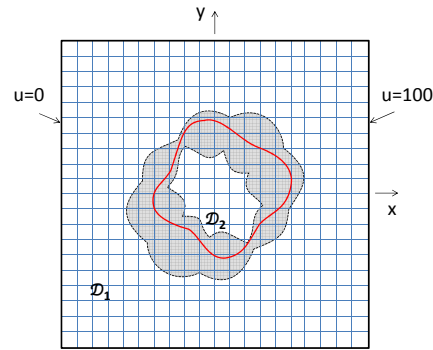
Fig. 14 Problem description for Example 3, shown with mesh size $h = 1$.

[3] was used to determine the reference energy norm using the XFEM for the interface geometry generated by $50,000$ random samples of $\boldsymbol{\xi}$ with 4 mesh sizes ($h = \{1, 0.5, 0.25, 0.125\}$). For $h = 0.125$, which was the smallest mesh size used for a MC reference solution, the mean energy norm of the reference solution is 157.523 with a 95% confidence interval of ± 0.00402. The comparison of the X-SFEM energy norm and the reference solution is shown in Figure 15 for 3 spatial mesh sizes ($h = \{1, 0.5, 0.25\}$). For each spatial mesh size, the Heaviside enriched X-SFEM solution converges quickly to the reference solution as the order of the PCE is increased. A higher convergence rate for each spatial mesh size is achieved when compared to the C^0-continuous enrichment functions explored in [6]. The stochastic approximation converges for order $p = 2$. Additionally, convergence to the reference solution is seen with spatial mesh refinement.
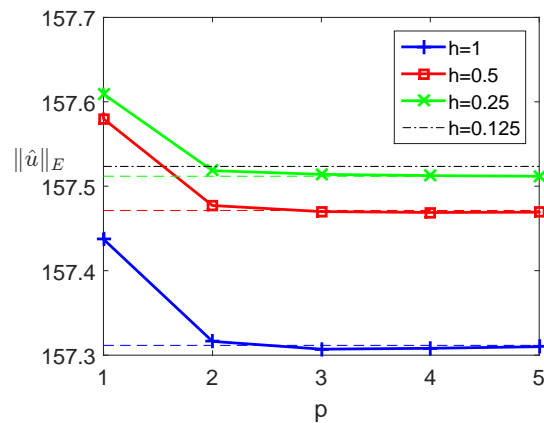

Fig. 15 Energy norm of the approximate solution for Example 3. The X-SFEM approximation and reference solution are represented by solid and dashed lines, respectively, for $h = \{1, 0.5, 0.25\}$.

5.4 Example 4: Ellipse

The Heaviside enriched X-SFEM for a problem with a discontinuous solution across the random material interface with a two-dimensional stochastic domain is studied. The fourth numerical example solves the heat diffusion problem (4) for a material with an ellipsoidal inclusion shown in Figure 16. The inclusion geometry is characterized by two random parameters, and the solution at the interface is discontinuous due to a thin interface layer with a thermal conductance of $\alpha = 10$. The flux at the interface is defined according to (6). The thermal conductivity of $\mathcal{D}_1$ and $\mathcal{D}_2$ are $k_1 = 2$ and $k_2 = 20$, respectively. The temperature on the left and right side of the domain is specified as $u_T = 0$ and $u_T = 100$. The random inclusion geometry is defined by the implicit representation of an ellipse and two random parameters with independent uniform distributions $U(-1, 1)$. Using the equation of an ellipse, the level set function is defined as

$$\phi(\boldsymbol{x}, \boldsymbol{\xi}) = r^2 - a(\xi_1)x_1^2 - b(\xi_2)x_2^2. \tag{33}$$

where $r = 5$ and $a(\xi_1) = 1 + 0.5\xi_1$ and $b(\xi_2) = 1 + 0.5\xi_2$. Using this definition instead of the signed distance function, the level set function is linear with respect to $\boldsymbol{\xi}$. As a consequence, the partition for stochastic integration exactly aligns with $\phi_i(\boldsymbol{\xi})$.
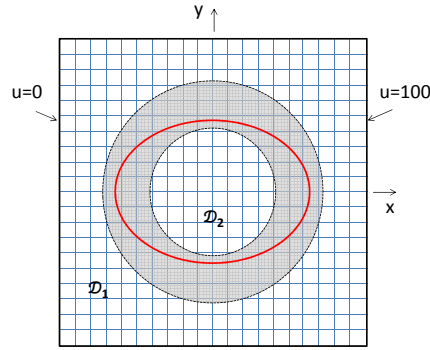

Fig. 16 Problem description for Example 4, shown with mesh size $h = 1$.

The convergence of the Heaviside enriched X-SFEM solution with increasing p is studied using a reference solution. The reference solution was computed with a least-squares polynomial chaos regression using the XFEM solutions for $50,000$ samples of $\boldsymbol{\xi}$ with 4 spatial mesh sizes ($h = \{1, 0.5, 0.25, 0.125\}$). The mean energy norm for the XFEM reference for $h = 0.125$ is 164.355 with a 95% confidence interval of ± 0.0606. The mean energy norm of the X-SFEM solution (32) is compared with the reference solution in Figure 17 for the three spatial mesh sizes of ($h = \{1, 0.5, 0.25\}$. The additional mesh size of $h = 0.125$ was included for the XFEM reference solution to show convergence. The X-SFEM energy norm converges quickly. Similar to Example 3, the stochastic approximation converges at

approximately $p = 2$. However, the X-SFEM solution does not converge to the corresponding reference solution for each spatial mesh size. When compared with Example 3, the reference energy norm has a larger variability as indicated by the confidence interval. The spatial error is dominating for the coarser mesh sizes of $h = 1$ and $h = 0.5$ with $p > 2$. A certain spatial resolution is required for convergence with a low order of the stochastic approximation. A similar requirement was identified in [6] using the C^0-continuous enrichment function for continuous problems.
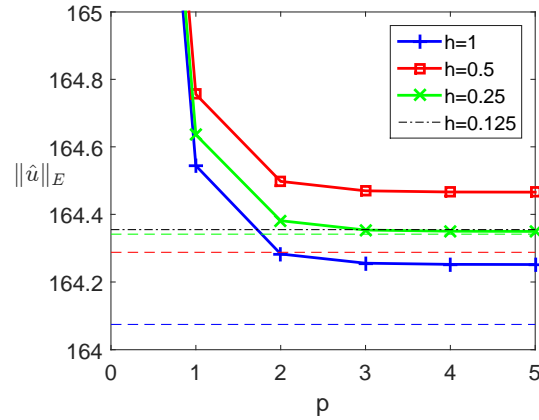

Fig. 17 Energy norm of the approximate solution for Example 4. The X-SFEM approximation and reference solution are represented by solid and dashed lines, respectively, for $h = \{1, 0.5, 0.25\}$.

6 Conclusions

A Heaviside enriched extended stochastic FEM has been developed for solving problems with uncertain inclusion geometry which have a discontinuous solution across the material interface. The Heaviside enrichment leads to a discontinuous solution in the stochastic domain, such that the degrees of freedom are nonzero (or active) on a subdomain of the stochastic domain. The active stochastic subdomain for each degree of freedom is determined by the spatial mesh and the random level set function. The stochastic approximation is constructed on the active stochastic subdomain for each degree of freedom, which leads to an accurate solution and well-conditioned system of equations. A minimum bounding hyperrectangle approximates the active stochastic subdomain, and the basis polynomials in the stochastic approximation are transformed and normalized onto the hyperrectangle. The proposed X-SFEM is best suited for a low number of random parameters due to the computational cost associated with construction of the numerous polynomial bases. Approximations of high dimensional stochastic functions with discontinuities is a challenging and active area of research.

The convergence and accuracy of the proposed method was demonstrated for example problems with continuous and discontinuous solutions at the interface. Studying problems with continuous solutions allowed a comparison to an existing approach. The proposed Heaviside enriched X-SFEM leads to a higher convergence rate for problems with continuous solutions when compared to using a C^0-continuous enrichment function. The degrees of freedom are smooth with respect to the random parameters regardless of the spatial mesh size. Due to the smoothness of the degrees of freedom, convergence in the stochastic space occurs with low orders of the polynomial approximation. Additional advantages of using the proposed Heaviside enrichment approach for problems with an uncertain interface configuration are that neighboring intersected elements and elements intersected more than once can be modeled accurately, and there are no issues with blending elements.

Acknowledgments

References

1. Fernández-Méndez S, Huerta A (2004) Imposing essential boundary conditions in mesh-free methods. Comput Methods Appl Mech Eng 193:1257–1275
2. Fries TP, Belytschko T (2010) The extended/generalized finite element method: an overview of the method and its applications. Int J Numer Methods Eng 84:253–304
3. Hampton J, Doostan A (2015) Coherence motivated sampling and convergence analysis of least-squares polynomial chaos regression. Comput Methods Appl Mech Eng 290:73–97
4. Hansbo A, Hansbo P (2004) A finite element method for the simulation of strong and weak discontinuities in solid mechanics. Comput Methods Appl Mech Eng 193:3523–3540
5. Juntunen M, Stenberg R (2009) Nitsche's method for general boundary conditions. Math Comput 78:1353–1374
6. Lang C, Doostan A, Maute K (2013) Extended stochastic FEM for diffusion problems with uncertain material interfaces. Comput Mech 51:1031–1049
7. Lang C, Makhija D, Doostan A, Maute K (2014) A simple and efficient preconditioning scheme for heaviside enriched XFEM. Comput Mech 54:1357–1374
8. Makhija D, Maute K (2014) Level set topology optimization of scalar transport problems. Struct Multidiscip Optim DOI 10.1007/s00158-014-1142-7

9. Makhija D, Maute K (2014) Numerical instabilities in level set topology optimization with the extended finite element method. Struct Multidiscip Optim 49:185–197

10. Moës N, Dolbow J, Belytschko T (1999) A finite element method for crack growth without remeshing. Int J Numer Methods Eng 46:131–150

11. Nouy A, Clément A (2010) Extended stochastic finite element method for the numerical simulation of heterogeneous materials with random material interfaces. Int J Numer Meth Engng 83:1312–1344

12. Nouy A, Schoefs F, Moës N (2007) X-SFEM, a computational technique based on X-FEM to deal with random shapes. Eur J Comput Mech 16:277–293

13. Nouy A, Clément A, Schoefs F, Moës N (2008) An extended stochastic finite element method for solving stochastic partial differential equations on random domains. Comput Methods Appl Mech Engrg 197:4663–4682

14. Savvas D, Stefanou G, Papadrakakis M, Deodatis G (2014) Homogenization of random heterogeneous media with inclusions of arbitrary shape modeled by xfem. Comput Mech 54:1221–1235

15. Sethian J (1999) Level Set Methods and Fast Marching Methods: Evolving Interfaces in Computational Geometry, Fluid Mechanics, Computer Vision, and Materials Science. Cambridge University Press

16. Stefanou G (2009) The stochastic finite element method: Past, present, and future. Comput Methods Appl Mech Engrg 198:1031–1051

17. Stefanou G, Nouy A, Clément A (2009) Identification of random shapes from images through polynomial chaos expansion of random level set functions. Int J Numer Meth Engng 79:127–155

18. Stenberg R (1995) On some techniques for approximating boundary conditions in the finite element method. J Comput Appl Math 63:139–148

19. Sukumar N, Chopp D, Moës N, Belytschko T (2001) Modeling holes and inclusions by level sets in the extended finite element method. Comput Methods Appl Mech Eng 190:6183–6200

20. Tan L, Zabaras N (2006) A level set simulation of dendritic solidification with combined features of front-tracking and fixed-domain methods. J Comput Phys 211:36–63

21. Terada K, Asai M, Yamagishi M (2003) Finite cover method for linear and nonlinear analyses of heterogeneous solids. Int J Numer Methods Eng 58:1321–1346

22. Wan X, Karniadakis G (2006) Multi-element generalized polynomial chaos for arbitrary probability measures. SIAM J Sci Comput 28:901–928

23. Wang M, Wang X, Guo D (2003) A level set method for structural topology optimization. Comput Methods Appl Mech Engrg 192:227–246

24. Xiu D (2010) Numerical Methods for Stochastic Computations: A Spectral Method Approach. Princeton University Press

25. Xiu D, Karniadakis G (2002) The Wiener-Askey polynomial chaos for stochastic differential equations. SIAM J Sci Comput 24:619–644